PoliTO Springer Series

Kristen M. Meiburger

Quantitative Ultrasound and Photoacoustic Imaging for the Assessment of Vascular Parameters

POLITECNICO
DI TORINO

Springer

PoliTO Springer Series

Springer, in cooperation with Politecnico di Torino, publishes the PoliTO Springer Series. This co-branded series of publications includes works by authors and volume editors mainly affiliated with Politecnico di Torino and covers academic and professional topics in the following areas: Mathematics and Statistics, Chemistry and Physical Sciences, Computer Science, All fields of Engineering. Interdisciplinary contributions combining the above areas are also welcome. The series will consist of lecture notes, research monographs, and briefs. Lectures notes are meant to provide quick information on research advances and may be based e.g. on summer schools or intensive courses on topics of current research, while SpringerBriefs are intended as concise summaries of cutting-edge research and its practical applications. The PoliTO Springer Series will promote international authorship, and addresses a global readership of scholars, students, researchers, professionals and policymakers.

More information about this series at http://www.springer.com/series/13890

Kristen M. Meiburger

Quantitative Ultrasound and Photoacoustic Imaging for the Assessment of Vascular Parameters

POLITECNICO
DI TORINO

Springer

Kristen M. Meiburger
Dipartimento di Elettronica e
Telecomunicazioni (DET)
Politecnico di Torino
Turin
Italy

ISSN 2509-6796 ISSN 2509-7024 (electronic)
PoliTO Springer Series
ISBN 978-3-319-48997-1 ISBN 978-3-319-48998-8 (eBook)
DOI 10.1007/978-3-319-48998-8

Library of Congress Control Number: 2016956175

Printed on acid-free paper

This Springer imprint is published by Springer Nature
The registered company is Springer International Publishing AG
The registered company address is: Gewerbestrasse 11, 6330 Cham, Switzerland

Preface

The aim of the work presented here is to develop quantitative techniques for ultrasound and photoacoustic imaging for the assessment of architectural and vascular parameters.

The works in this book can be divided into two macro areas: (1) morphological vascular studies based on the development of quantitative imaging techniques for the use with clinical B-mode ultrasound images, and (2) preclinical architectural vascular studies based on quantitative imaging techniques for ultrasound and photoacoustics.

The first section, which makes up the second and third chapters, focuses on the development and validation of quantitative techniques for the assessment of vascular morphological parameters that can be extracted from B-mode ultrasound longitudinal images of the common carotid artery. In Chap. 2, results from numerous past studies are presented, including the validation of techniques for correctly locating the CCA in B-mode ultrasound images, the development and implementation of novel completely automated techniques for the IMT measurement and plaque segmentation, and the validation and association of the automatically measured IMT value with clinical parameters. Chapter 3 focuses instead on the validation of the intima-media thickness variability parameter. Recent studies have shown that the IMT variation along the carotid artery wall has a stronger correlation with atherosclerosis than the nominal intima-media thickness value itself; hence this chapter presents an in-depth study and validation of the IMT variability (IMTV) parameter, confronting the question if manual segmentations of the lumen–intima and media–adventitia borders can be trusted as ground truth in the calculation of this parameter.

The second section, the fourth and fifth chapters, instead emphasizes quantitative imaging techniques for the assessment of architectural parameters of vasculature that can be extracted from 3D volumes, first using contrast-enhanced ultrasound (CEUS) imaging and, second, photoacoustic imaging without the administration of any contrast agent. More specifically, Chap. 4 demonstrates how the characterization and description of the vascular network of a cancer lesion in mouse models can be effectively determined using both traditional microbubbles and liposomes. Eight mice were administered both microbubbles and liposomes and 3D CEUS volumes were acquired. Vascular architectural descriptors were calculated after a skeletonization technique was applied. Chapter 5 focuses on the development and validation of a skeletonization technique for the quantitative assessment of vascular architecture in burn wounds using completely non-invasive photoacoustic imaging, thus not requiring any contrast agent administration. It was shown how this technique could provide quantitative information about the vascular network from photoacoustic images that can distinguish healthy from diseased tissue.

A summarizing discussion (Conclusions and Final Remarks) concludes this work.

Turin, Italy Kristen M. Meiburger

Contents

Chapter 1
Introduction

Abstract Medical imaging has been forever revolutionized by the technological and digital boom that has occurred over the last few decades. The idea of quantitative analysis of medical images by a computer was first reported in the 1960s (Lodwick et al, Radiology, 80(2):273–275, 1963, [1], Meyers et al, Radiology 83(6):1029–1034, 1964, [2], Winsberg et al, Radiology 89(2):211–215, 1967, [3], Kruger et al, IEEE Trans Biomed Eng, 3:174–186, 1972, [4], Kruger et al, IEEE Trans Syst Man Cybern, 1:40–49, 1974, [5], Toriwaki et al, Comput Graph Image Process, 2(3):252–271, 1973, [6]), and at that time it was generally assumed that computers could replace medical practitioners in detecting abnormalities, because computers and machines are better at performing certain tasks than human beings are. However, growth of this sector remained initially quite limited due to the fact that computers were not sufficiently powerful, advanced image-processing techniques were not available, and digital images were not easily accessible (Doi, Comput Med Imaging Graph, 31(4–5):198–211, 2007, [7]). Since those days, along with the evolution of technology and digital imaging in general, the idea of actually *replacing* medical practitioners has also evolved, bringing forth the idea of Computer Aided Diagnosis (CAD), in which the computer output can by utilized by medical practitioners, but not replace them. This field, which is based on the idea that digital medical images are analyzed quantitatively by computers, has spread widely and quickly, becoming one of the major research subjects in medical imaging. Therefore, the development of advanced image processing techniques is required in order to obtain quantitative information (Doi, Comput Med Imaging Graph, 31(4–5):198–211, 2007, [7]).

1.1 Quantitative Imaging

Healthcare continues to seek improved quantitative medical imaging biomarkers with which to better diagnose, treat, and monitor the health of patients. In fact, quantitative imaging (QI) is becoming an increasingly common tool in modern medicine, advancing from research trials to clinical reading rooms [8].

K.M. Meiburger, *Quantitative Ultrasound and Photoacoustic Imaging for the Assessment of Vascular Parameters*, PoliTO Springer Series,
DOI 10.1007/978-3-319-48998-8_1

But what is quantitative imaging? According to the Quantitative Imaging Biomarkers Alliance (QIBA) [9]:

> Quantitative imaging is the extraction of quantifiable features from medical images for the assessment of normal conditions or the severity, degree of change, or status of a disease, injury, or chronic condition relative to normal. Quantitative imaging includes the development, standardization, and optimization of anatomical, functional, and molecular imaging acquisition protocols, data analyzes, display methods, and reporting structures. These features permit the validation of accurately and precisely obtained image-derived metrics with anatomically and physiologically relevant parameters, including treatment response and outcome, and the use of such metrics in research and patient care.

Quantitative imaging can theoretically be applied to any digital imaging modality, and currently has important clinical applications in ultrasound, computed tomography (CT), magnetic resonance imaging (MRI), nuclear medicine, including positron emission tomography (PET), and more recently, photoacoustic (PA) imaging. Quantitative imaging is obviously enhanced by volumetric data sets, which facilitate assessments of morphological, functional, parametric, and other quantitative features [8]. The use of contrast agents and imaging over a period of time also enhances quantitative imaging possibilities, providing the enhancement of structures that normally produce low image contrast, and also allowing a comparison between pre- and post-contrast images and the assessment of the rate and pattern of enhancement or washout over time [8].

1.1.1 Ultrasound

Ultrasound imaging is a non-invasive imaging methodology which provides real-time information about tissue anatomy and function. It is based on the emission of ultrasound waves that interact with tissue and are reflected back to the probe and therefore detected. Image contrast in ultrasound imaging is based on the difference of adjacent tissue impedances, with a large difference of impedance producing a higher amplitude ultrasound wave that is reflected and therefore detected. This methodology is portable, real-time, inexpensive, and does not use ionizing radiation; however it suffers from being operator-dependent, it has a small field of view and is limited by the large impedance difference of bone and air compared to other soft tissues. There are various ultrasound imaging modes, but the prevalent ones are B-mode ultrasound imaging, Doppler imaging, and contrast-enhanced ultrasound imaging.

Gray-scale B-mode ultrasound images are commonly used to obtain size and distance measures, providing the basis for diagnosis in much of obstetric and cardiac imaging [8]. This modality is commonly used for the screening and evaluation of atherosclerosis, as the carotid artery wall is easily imaged with ultrasounds and permits the assessment of the artery wall thickness and/or plaque stenosis [10–15]. It is also often used for fast-look follow-up examinations. Doppler ultrasound has been used for quantitative characterization of vascular disease as well [16]. Contrast-enhanced ultrasound imaging is also widely used, mainly to enhance the vasculature of structures. Studies have shown how this technique can distinguish malignant from benign tumors [17–19] and it has been used for perfusion studies of organs after transplantation [20].

1.1.2 CT

Computed tomography, which is used to refer to X-ray computed tomography, is a non-invasive imaging technique that provides information about internal organs, bones, soft tissue, and blood vessels. It combines a series of X-ray views taken from many different angles and computer processing to create cross-sectional images. It is a modality based on ionizing radiation (i.e., x-rays) that can produce adverse effects, but the modality has many benefits that can outweigh potential risks. CT images are formed by emitting x-ray photons from an x-ray tube which interact with the imaged area of the body, and then exit the patient and are detected. Contrast in CT depends mainly on tissue attenuation properties.

The standardization of the CT pixel value with the Hounsfield unit (HU) scale allows the characterization of tissue density [21]. HU measures allow lesion characterization using a region of interest (ROI)-based measurement of average density or voxel-counting based on a threshold value [22]. Dual-energy CT scanners have recently emerged, bolstering the clinical role of QI. Using this modality, improved characterization of tissue has been made possible thanks to the differential absorption of x-rays by tissues of differing chemical composition at various energies [23], and it has been used to determine the composition of renal calculi [24].

1.1.3 MRI

Magnetic resonance imaging (MRI) is a non-invasive imaging technique, which provides information about in-vivo tissue anatomy, function and metabolism. This modality does not rely on ionizing radiation, but it is quite expensive. MRI makes use of hydrogen atoms predominantly originating from tissue water to generate images. By manipulating the magnetic moments of the hydrogren nuclei with radio frequency (RF) fields, images can be produced [8]. Contrast in MRI depends mainly on three parameters: proton spin density (PD), the longitudinal relaxation time (T_1), and the transverse relaxation times (T_2 and T_2*).

MR signal intensity units lack inherent meaning, being influenced by sequence parameters as well as hardware and software selection. However, some advanced MRI sequences and postprocessing techniques allow for the computation of parametric maps in which the pixel values are used for diagnosis. Some examples are: calculation of the T_2* relaxation time which is used in liver imaging as a marker of the presence and severity of hepatic iron deposition [25]; Diffusion weighted (DW) MRI for the apparent diffusion coefficient (ADC) of tissue [26]; MRI spectroscopy for the extraction of information regarding the presence and concentration of chemicals in a Region-Of-Interest (ROI) [27].

1.1.4 Nuclear Medicine

Nuclear medicine, and Positron emission tomography (PET) [28] in particular, is a functional imaging technique that produces a three-dimensional image of functional processes in the body. The system detects pairs of gamma rays emitted indirectly by a positron-emitting radionuclide (tracer), which is introduced into the body on a biologically active molecule. Three-dimensional images of tracer concentration within the body are then constructed by computer analysis. This modality requires the administration of an ionizing contrast agent, yet it still remains a powerful tool for evaluating tissue metabolism.

PET imaging allows the calculation of the standardized uptake value (SUV) which represents the concentration of radioactivity within a tissue, normalized by dividing it by the ratio between the decay-corrected injected radioactivity and that patient's body weight, lean body mass, or surface area [8, 29, 30]. This parameter is used to determine the likelihood of malignancy of a lesion and to predict tumor aggressiveness and treatment response. Other PET-based parameters that are being applied in clinical decision-making include the metabolic tumor volume, total lesion glycolosis, and heterogeneity index [8].

1.1.5 Photoacoustics

Photoacoustic imaging is a relatively new imaging modality that can provide information about in-vivo tissue composition, function and metabolism. It is based on the illumination of tissue with a pulsed laser light, usually in the near infrared (NIR) spectrum, that is absorbed by the tissue which undergoes a rapid conversion to heat which produces a small temperature rise. This effect results in the emission of broadband low-amplitude acoustic waves which can be detected by an ultrasound receiver and processed to form an image. Contrast is based on tissue absorption properties at different wavelengths. It is often coupled with ultrasounds to provide the anatomical structure image.

The spectroscopic properties of oxygenated haemoglobin and deoxygenated haemoglobin provide a natural endogenous contrast agent for this technique, but still many exogeneous contrast agents exist and are undergoing constant evolution. Some photoacoustic contrast agents that are used are methylene blue, ICG, and gold nanoparticles, to mention a few [31–35]. This imaging modality, especially with the application of contrast agents, has a strong presence in preclinical imaging [34–37], but it is quickly making its way to clinical studies, as various research groups have recently used this modality for the evaluation of breast cancer [38–40].

As can be noted from the previous paragraphs, there are many different modalities that can be taken advantage of for quantitative imaging. However, both nuclear medicine and CT imaging modalities require the use of ionizing radiation, which should, if possible, be avoided. MRI does not require ionizing radiation, but the exam is far from being portable and is expensive. Ultrasound imaging, on the other hand, thanks to its non-invasive nature, low cost, broad diagnostic applicability and easy handling, is the second-most used imaging modality in clinical practice after conventional x-ray radiography [41, 42]. Photoacoustic imaging, which is undergoing an exponential growth in research, also does not use ionizing radiation and can provide important functional information, thanks to the spectroscopic properties of this imaging modality. For these reasons, the work in this final work focused on the development of quantitative imaging techniques for ultrasound and photoacoustic imaging, two fundamental biomedical imaging modalities that are explained in more detail in Sects. 1.2 and 1.3.

1.2 Ultrasounds

Ultrasounds, as the name itself already implies, are sound waves that oscillate at a frequency which is greater than the upper limit of human hearing ($f > 20\,\text{kHz}$). Since ultrasounds are mechanical waves of compression and rarefaction, the only type of energy that they transfer to biological tissues is mechanical, which stimulates the tissue molecules. The propagation speed of ultrasounds varies depending on the elasticity of the material and has the following relation with the sound cycle frequency:

$$v = \lambda f \tag{1.1}$$

where v is the propagation speed, f is the frequency, and λ is the wavelength.

Another important parameter that can be calculated for various materials is the acoustic impedance (Z) by the following equation:

$$Z = \rho v \tag{1.2}$$

where v is the propagation speed and ρ is the medium density.

As Table 1.1 shows, many tissues and organs that are quite different from one another can still show similar density and acoustic impedance values. It can also be observed that most biological tissues have propagation speeds that are close in value, so generally a typical value of 1540 m/s is assumed.

Ultrasounds are generated due to the piezoelectric effect. When an electrical impulse is applied to a piezoelectric element, it vibrates and produces the ultrasound. Vice versa, when a piezoelectric element is vibrated, it produces a pulse of electricity. An ultrasound transducer contains on its surface an array of piezoelectric crystals, which each produce an ultrasound wave. The summation of all of the generated waves forms the ultrasound beam. Ultrasound waves are generated in pulses and each pulse

Table 1.1 Tissue and organ characteristics

Material	Density [kg/m^3]	Propagation speed [m/s]	Acoustic impedance [kg/m^2/s $\cdot 10^{-6}$]
Air	1.2	330	0.0004
Water	1000	1480	1.48
Soft tissue (mean)	1060	1540	1.63
Liver	1060	1550	1.64
Muscle	1080	1580	1.70
Fat	952	1459	1.38
Brain	994	1560	1.55
Kidney	1038	1560	1.62
Lung	400	650	0.26
Bone	1912	4080	7.80

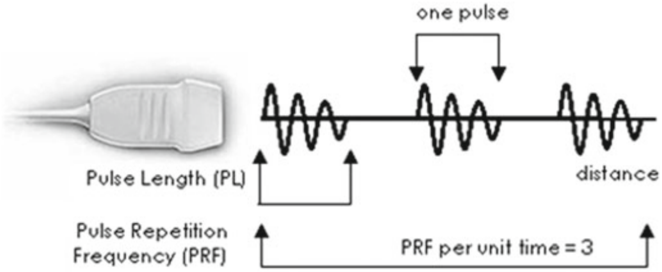

Fig. 1.1 Ultrasound pulse parameters. Image available from: http://www.usra.ca/

generally consists of 2 or 3 sound cycles of the same frequency. The pulse length (PL) is the distance travelled per pulse, while the pulse repetition frequency (PRF) is the rate of pulses emitted by the transducer (number of pulses per unit time). These parameters can be seen in Fig. 1.1.

As an ultrasound wave propagates through matter, it interacts in various ways. First of all, the ultrasound pulse continuously loses energy. The *attenuation* that it undergoes is defined by the following equation:

$$A(z) = A_0 e^{-\alpha z} \tag{1.3}$$

where $A(z)$ is the amplitude of the pulse at the depth z, A_0 is the initial amplitude of the pulse, and α is the absorption coefficient of the matter which increases the higher the frequency is. Furthermore, the attenuation (I) of the ultrasound wave (in dB) as it passes from one medium to another can be defined as follows:

$$I = 20 \cdot \log_{10} \frac{A_2}{A_1} \tag{1.4}$$

When an ultrasound pulse meets an interface between two different materials, the pulse is not only attenuated as described above, but it also undergoes two interactions of fundamental importance for ultrasound imaging: *reflection* and *transmission*. These two phenomena are generally expressed through the reflection coefficient R, and the penetration coefficient T:

$$R = \left(\frac{Z_1 - Z_2}{Z_1 + Z_2} \right)^2 \tag{1.5}$$

$$T = 1 - R \tag{1.6}$$

So, if the two materials present similar values of acoustic impedance, very little of the pulse is reflected. On the other hand, if the two materials have very dissimilar values of acoustic impedance (as what happens if one of the materials is air), almost all of the pulse energy is reflected and, therefore, does not penetrate into the tissue which is found below.

1.2.1 Ultrasound Imaging

Ultrasound imaging is based on the fact that the ultrasound pulse is partly reflected when it meets an interface between two materials with different acoustic impedance. The same transducer that emits the ultrasound pulse also receives the reflected echoes of the pulse, and the depth at which the echo is produced (d) can be found by measuring the time required for the pulse to travel to the reflecting site and for the echo pulse to return (Δt):

$$d = \frac{1}{2} c \Delta t \tag{1.7}$$

where c is equal to the average propagation speed in biological tissues (1540 m/s).

So, by emitting a sequence of ultrasound pulses along different scansion lines and by listening to the return echoes produced (Fig. 1.2), an image that shows the spatial distribution of the discontinuities of the irradiated tissues can be generated.

The most common visualization strategy that is used is B-mode, which is based on brightness. In B-mode ultrasound images, a certain pixel of the image is brighter if the amplitude of the return echo in that point is greater. So, strong specular reflections give rise to bright pixels (*hyperechoic*), weaker diffuse reflections produce gray pixels (*hypoechoic*), and no reflection produces dark pixels (*anechoic*).

The bi-dimensional image exhibits along the horizontal axis the width extension of the tissue that is irradiated, while the vertical axis reveals the depth of the pulse that generated the return echo.

A fundamental parameter in all imaging techniques is *spatial resolution*. Axial spatial resolution depends on the wavelength of the sound cycle that is emitted. In ultrasound imaging, however, the emission of an ultrasound pulse consisting of only one sound cycle is hardly ever used, as discussed previously. In order to have a

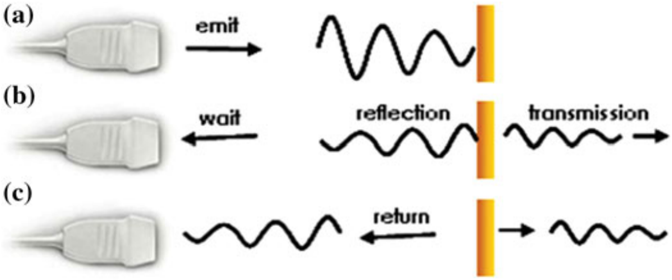

Fig. 1.2 Example of emission of ultrasound pulses and waiting for return echoes. Image available from: http://www.usra.ca/

narrow bandwidth of frequencies with a minimum power loss, an ultrasound pulse consisting of two or three sound cycles is emitted. In this way, the axial spatial resolution depends not on the wavelength of the sound cycle but on the pulse length. If the distance between two points is greater than the pulse length, then the points will be seen as two distinct objects.

With these considerations, it can be observed that the higher the frequency is (therefore, the shorter the wavelength is, considering the same propagation speed), the better the axial spatial resolution. High frequencies are, therefore, optimal for a clearer image, but there is the disadvantage that tissues absorb more energy at higher frequencies, putting a limit on the possible scansion depth [43].

1.2.2 Contrast Enhanced Ultrasound Imaging (CEUS)

CEUS is an enhanced form of ultrasound scan that uses intravenous administration of a contrast agent, typically microbubbles. This contrast agent is an intraluminal tracer and can be used to obtain angiography-like images of vasculature. Ultrasound scan contrast agents were introduced in clinical practice in the early 1990s. The currently approved and used agents include SonoVue (Bracco SpA, Milan, Italy), Optison (GE Healthcare, Princeton, NJ), Definity (Lantheus Medical Imaging, N. Billerica, Mass), and Levovist (Schering AG, Berlin, Germany). The contrast agents consist of microbubbles (approximately 1–8 μm), generally filled with a perfluorinated gas that has a low solubility, and stabilized with a phospholipid or protein shell to improve circulation time [44]. Because of the size of microbubbles, they cannot leave the intravascular compartment, or in other words, they cannot extravasate. The microbubble shell is eliminated from the body through the reticuloendothelial system when the gas is exhaled. Contraindications for microbubble contrast agents are unstable angina, acute cardiac failure, acute endocarditis, known right-to-left shunts, and known allergy for microbubble contrast agents. Microbubble contrast agents have been administered in millions of patients and are safe; side effects are extremely rare [45].

For clinical applications, microbubble contrast agents have been registered for tissue perfusion imaging and cardiac chamber border enhancement [44]. Most commercially available ultrasound systems provide specific pulse sequences, such as amplitude modulation or pulse inversion, that retrieve nonlinearities at low acoustic power, which are only exhibited by microbubbles [46]. These techniques enable the suppression of tissue in the image and allow the specific identification of the microbubbles signal.

1.3 Photoacoustics

Photoacoustic (PA) imaging, also known as optoacoustic imaging, is a biomedical imaging modality that has seen exponential growth in the last couple of decades [47]. This hybrid modality, which is based on the use of laser-generated ultrasound, combines spectroscopic-based specificity of optical imaging with the high spatial resolution of ultrasound imaging.

The discovery of the photoacoustic effect dates back to 1880 when Alexander Graham Bell first observed the generation of sound owing to the absorption of modulated sunlight [48]. Despite the early discovery of this physical phenomenon, very little active scientific research or technological development took place, mainly due to the lack of an adequate light source. In fact, it was only with the development of the laser in the 1960s that sensing applications began to be investigated, since the laser source finally provided the necessary high peak power, spectral purity and directionality that PA sensing applications require [47].

Still, even after the development of the laser, applications were first more geared towards the exploitation of the indirect gas-phase cell type of PA detection, and the first uses of the direct detection of laser-induced ultrasound waves were focused on characterizing solids as a potential non-destructive testing tool. The first investigations of using the photoacoustic effect for biomedical imaging were only in the mid 1990s and the first biomedical images appeared soon thereafter [36, 49–51]. With these first images, the field of photoacoustic imaging continued to progress steadily but really only began to see its exponential growth once the first truly compelling *in-vivo* images began to be obtained in the early to mid 2000s [47].

1.3.1 The Photoacoustic Effect

As already mentioned, the photoacoustic effect is based on laser-generated ultrasound. As can be seen in Fig. 1.3, there is first an optical path, in which a pulsed light source irradiates the tissue which absorbs the light. The absorption by tissue chromophores is then followed by a rapid conversion to heat which produces a small temperature rise. This effect leads to the acoustic path, since there is an initial pressure increase which then relaxes, resulting in the emission of broadband low-amplitude

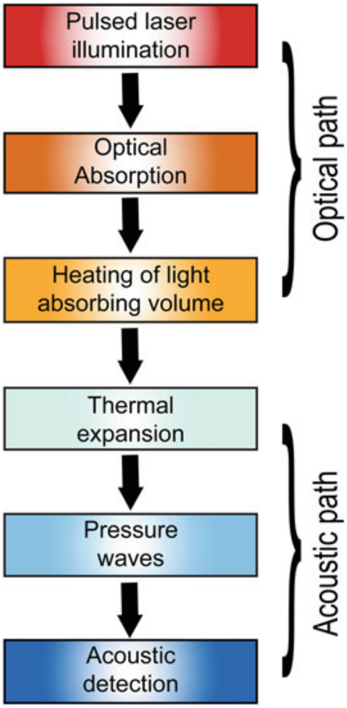

Fig. 1.3 The photoacoustic effect

acoustic waves which can be detected by an ultrasound receiver and processed to form an image [52–54].

So, the mechanism of signal generation can be described as one in which the optically induced initial pressure distribution, called p_0, is encoded onto a propagating acoustic wave which is then converted to a time-resolved electrical signal upon detection by the ultrasound receiver. From this explanation, it is clear that the resulting photoacoustic image is therefore a representation of p_0. In order to generate acoustic waves, the thermal expansion needs to be time-variant [55], which therefore requires that the acoustic propagation time is small compared with the length scale of the heated volume [47]. A typical laser pulse duration in photoacoustic imaging is less than $10ns$, which respects both the thermal and stress confinement times, which are explained in more detail in [55]. In this case, with simple thermodynamic considerations and assuming 1D plane wave propagation in a homogeneous medium, it can be shown that p_0 at a certain point z is proportional to the absorbed optical energy $H(z)$, as shown in Eq. 1.8.

$$p_0(z) = \frac{\beta {v_s}^2}{C_p} H(z) \tag{1.8}$$

where β is the thermal coefficient of volume expansion, v_s is the speed of sound in tissue and C_p is the specific heat capacity of the tissue at constant pressure. The absorbed optical energy $H(z)$ is given by the product of the local absorption coefficient $\mu_a(z)$ and the optical fluence ϕ_0 at depth $z = 0$ multiplied by $\mathrm{e}^{-\mu_{eff}(z)}$, where $\mu_{eff}(z)$ is the effective extinction coefficient of the tissue, defined as $\mu_{eff}(z) = \sqrt{3\mu_a(\mu_a + \mu_s')}$ and μ_s' is the scattering coefficient of tissue [52–54, 56]. The ratio $\frac{\beta {v_s}^2}{C_p}$ is also known as the Grüneisen coefficient, Γ, a dimensionless thermodynamic constant that provides a measure of the conversion efficiency of heat energy into pressure. So, we can rewrite Eq. 1.8 as:

$$p_0(z) = \Gamma \mu_a \phi_0 \mathrm{e}^{-\mu_{eff}(z)} \tag{1.9}$$

As can be noted in (1.8) and (1.9), p_0 depends on various mechanical, thermodynamic and optical parameters. Making the assumption that the mechanical and thermodynamic properties are spatially invariant, which is generally considered in PA imaging since they do not significantly vary between different tissue types, it is clear how photoacoustic image contrast is largely determined by the wavelength-dependent μ_a. This assumption inevitably has some limitations, and recently it has become more widely recognized that in certain tissues image contrast may partially originate from heterogeneities in the Grüneisen coefficient [57]. Nonetheless, optical absorption and scattering properties of the tissue still remain the dominating factor in photoacoustic image contrast [34]. It is important to note, however, that this does not imply a direct proportion between image contrast and μ_a; in fact, p_0 is proportional to the product between μ_a and the laser fluence ϕ which is itself dependent on μ_a, so p_0 can therefore be considered a non-linear function of μ_a.

Since optical absorption, which changes with the light source wavelength, is still the primary source of photoacoustic image contrast, this imaging modality is very promising for the visualisation of anatomical features that contain an abundance of endogenous chromophores, such as haemoglobin, lipids and water. The variation of the absorption coefficient μ_a of some important endogenous chromophores as function of wavelength is shown in Fig. 1.4. The PA signal intensity at different optical wavelengths can therefore be used to characterize optical properties of tissue.

1.3.2 Penetration Depth and Spatial Resolution

In photoacoustic imaging, the penetration depth is limited by optical and acoustic attenuations. Acoustic attenuation is significant in most soft tissues, but optical attenuation typically dominates. Optical attenuation depends on the absorption and scattering coefficients (which give forth the effective attenuation coefficient derived from diffusion theory [47]) and is most of all limited by the wavelength of laser illumination [34, 47].

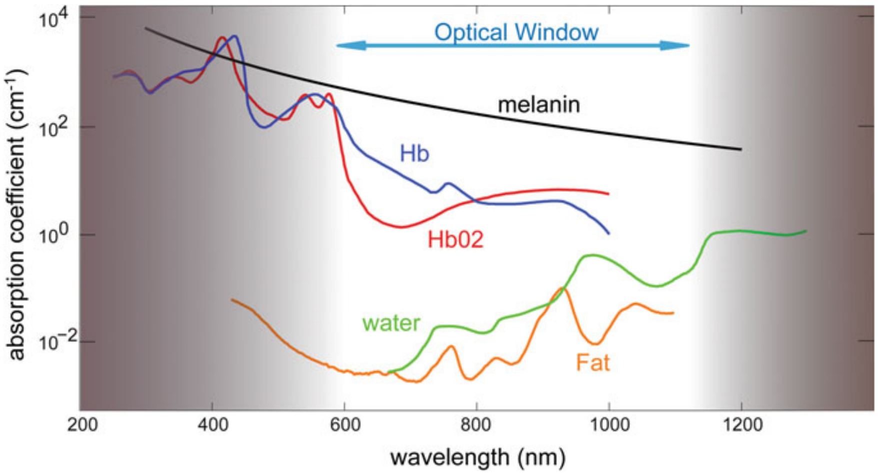

Fig. 1.4 Absorption spectra of endogenous chromophores in the body. Data for the absorption coefficient were obtained from http://omlc.ogi.edu/spectra/

Table 1.2 Maximum permissible exposure (MPE) values at different wavelengths

MPE $[\frac{\mathrm{mJ}}{\mathrm{cm}^2}]$	Wavelength λ [nm]
20	$400 < \lambda < 700$
$20 \times 10^{0.002(\lambda-700)}$	$700 < \lambda < 1050$
100	$1050 < \lambda < 1500$

Since endogenous tissue chromophores have less optical absorption in the optical window (600–1100 nm), greater penetration depth can be achieved using these wavelengths to illuminate the tissue. Nevertheless, considering an excitation wavelength of 700 nm and assuming physiologically realistic values of endogenous chromophores and scattering coefficients, it can be found that once beyond the first millimeter in tissue, light is attenuated by approximately a factor of 4 for each additional centimeter of penetration depth [47]. So considering a value of 0.75 dB $\mathrm{cm}^{-1}\,\mathrm{MHz}^{-1}$ for plane wave acoustic attenuation and a center frequency of 10 MHz, we can find that the total attenuation is therefore at least one order of magnitude per centimeter [47].

Penetration depth thus represents one of the major challenges in photoacoustic imaging since to penetrate several centimeters in tissue, a signal attenuation of several orders of magnitude incurs therefore requiring the detection of extremely weak return ultrasound signals. An initial high energy pulse can in part mitigate this challenge, but for obvious safety reasons the American National Standards Institute for human skin imposed maximum permissible exposure (MPE) values which limits the amount of energy possible in each pulse. The MPE limit at different wavelengths can be found in Table 1.2 [58].

Similarly to traditional ultrasound imaging, the spatial resolution in photoacoustic images ultimately depends on the frequency content of the acoustic wave arriving at the detector. Nanosecond excitation laser pulses, which are most commonly used, can result in very broadband acoustic waves with a frequency content ranging up to several tens or even hundreds of megahertz, depending on the length scale of the optical absorbers [47]. So, there is a trade-off between imaging depth and spatial resolution limit: increasing the imaging depth, frequency-dependent attenuation decreases the BW and center frequency of the ultrasound wave, resulting in poorer spatial resolution [59]. An approximate rule of thumb is that for centimeter penetration depths, sub-millimeter spatial resolution is possible, decreasing to sub-100 µm for millimeter penetration depths and sub-10 µm for depths of a few hundred microns.

1.3.3 Photoacoustic Imaging Modalities

Considering this trade-off between penetration depth and resolution, various photoacoustic systems have been developed to image microscopic and macroscopic features. More specifically, there are three main photoacoustic imaging modalities:

1. **Photoacoustic tomography**. Photoacoustic tomography is usually considered the traditional mode of PA imaging as envisaged by early practitioners, and it is the modality that was used for the study in this work. It is also the most general and least restrictive PA imaging approach with the fewest limitations on imaging performance imposed by its practical implementation. With photoacoustic tomography (PAT), full field illumination, in which a large diameter pulsed laser beam irradiates the tissue surface, is employed. At NIR wavelengths where tissue is relatively transparent, light is able to penetrate deeply and is also strongly scattered, resulting in a relatively large tissue volume that gets ‘bathed’ in diffuse light. The broadband ultrasonic waves that are produced by the tissue propagate to the tissue surface where they are detected by a mechanically scanned ultrasound receiver or array of receivers. The time-varying detected ultrasound signals can then, with knowledge of the speed of sound, be spatially resolved and back-projected to reconstruct a three-dimensional image. There are three commonly used detection geometries: spherical, cylindrical and planar. Clearly, the cylindrical or spherical detection geometries require access to all points around the target and are therefore limited to applications such as imaging the breast or small animals, such as mice. Planar detection geometries are more versatile providing access to a greater range of anatomical targets, especially those superficially located [47, 60].
2. **Photoacoustic microscopy**. PA microscopy refers to techniques in which a PA image is obtained by mechanically scanning either a focused ultrasound detector or a focused laser beam. The image is then formed directly from the set of acquired A-lines, without the aid of a reconstruction algorithm as in PAT. The term acoustic resolution PA microscopy (AR-PAM) refers to when a focused ultrasound detector is used, since axial and lateral spatial resolution is defined by the physics of ultrasound propagation and detection. On the other hand, if a focused laser beam is used, it is termed OR-PAM since the spatial resolution in at least one plane

(usually, the lateral) is defined by the spatial characteristics of a focused laser beam propagating in tissue [61]. Even though it is called PA microscopy, this technique does not necessarily imply the observation of anatomy on a small length scale—AR-PAM, for example, can be used to image to depths of several centimetres [47, 62].

3. **Endoscopic devices**. There are several potential clinical applications in which the target tissue can only be accessed by introducing a miniature endoscopic probe percutaneously or through a natural orifice. Among these are the clinical assessment of coronary artery disease, prostate cancer and gastrointestinal pathologies. A number of prototype PA endoscopic or intravascular devices, conceptually similar to conventional US probes, have been developed [63–71] for these applications. Intravascular PA imaging employs a sideways looking rotating probe in a manner analogous to IVUS. A variety of other PA intravascular probe designs based on different light delivery and ultrasound detection mechanisms have also been demonstrated [64–69].

1.4 Disease Models and Their Architectural and Vascular Parameters

1.4.1 Atherosclerosis and the Common Carotid Artery (CCA)

Atherosclerosis is the earliest manifestation of the possible onset of a cardiovascular disease (CVD), and it is a process which refers to the degeneration of the arterial wall and the deposition of lipids and other blood-borne material within the arterial wall of almost all vascular territories [72–74]. It has been shown that the lipid deposit might be the consequence of an inflammatory process that takes place in the artery wall, and numerous studies that link atherosclerosis and inflammation have been published. Particular interest has been shown in the atherosclerotic process that takes place in the common carotid artery (CCA), since carotid wall lesions have been correlated to a various number of pathologies [75].

The common carotid artery is an artery of paramount importance, since it is responsible for supplying the neck and head (and, therefore, also the brain) with oxygenated blood. It is a paired structure, meaning that there are two in the body: the left and right carotid arteries.

Once born from the aortic arc, the carotid arteries follow the neck axis, at a depth of about 2–4 cm. Figure 1.5 shows on the left panel the anatomy of the carotid artery and its course along the neck. On the right panel, we can see the supra-aortic arterial circulation. The course of the common carotid artery is shown, as well as its bifurcation that originates the internal and external carotid arteries.

The CCA wall is composed of endothelial cells, smooth muscle cells and extracellular matrix, including collagen and elastin. These are arranged into three concentric layers: intima, media and adventitia.

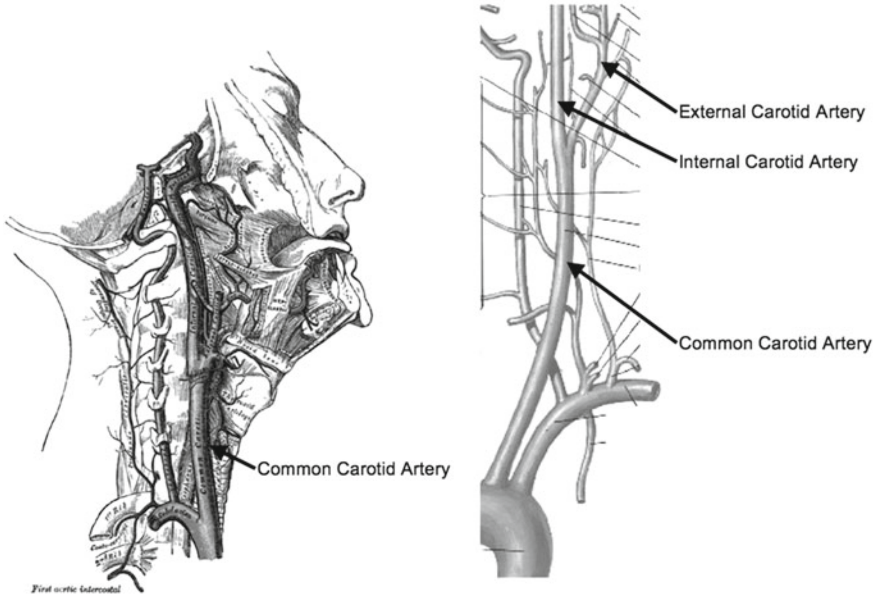

Fig. 1.5 Anatomy of the CCA and the supra-aortic arterial circulation. Image taken with permission from: [75]

Ultrasound Imaging of the CCA

The B-mode ultrasound scan of the carotid artery in its common tract is nowadays a widely adopted clinical exam for the assessment of the artery status. During this exam, the patient is generally asked to lay in a supine position with their head slightly tilted back (Fig. 1.6). The ultrasound probe can be applied in a way to acquire either a longitudinal or transverse image of the CCA, but the longitudinal image is generally preferred. The transducer that is used is generally a high frequency (7–12 MHz) linear

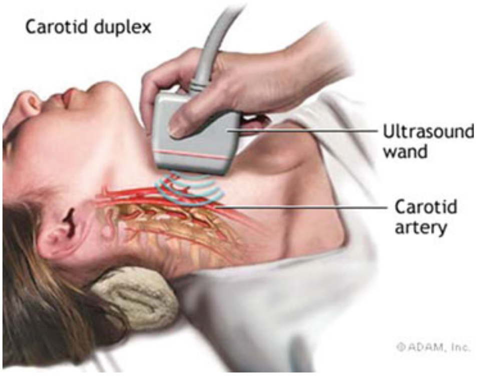

Fig. 1.6 Example of a clinical exam for carotid artery assessment. Image available from: http://health.nytimes.com/

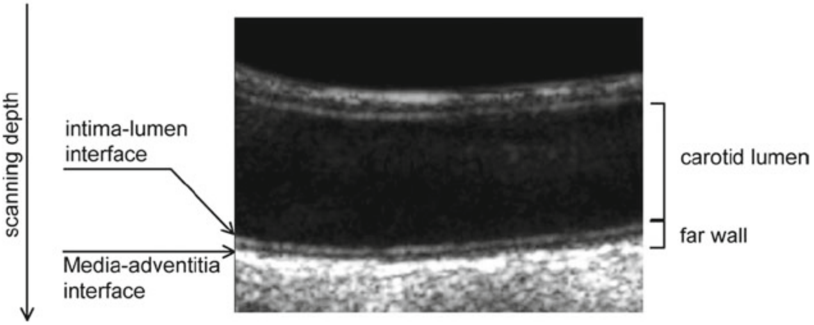

Fig. 1.7 B-mode ultrasound image of the CCA. Image taken with permission from: [76]

probe. Since the carotid artery is anatomically positioned in a place that is close to the surface, the limitation of scansion depth that higher frequencies present is not a problem. The use of higher frequencies also permits a better spatial resolution which is an especially important feature when measurements must be made on the image.

Figure 1.7 shows an exemplary B-mode image that is obtained during this clinical exam. As can be clearly seen, the artery appears as a tube which runs along the entire width of the image. The lumen of the artery appears anechoic, since red blood cells present dimensions which are too small to produce an echo. The near wall (close to the top of the image) and far wall (close to the bottom of the image) are, on the other hand, clearly visible in the image.

The interfaces of the artery wall that can be distinguished in the image, however, do not account for all of the layers that are actually present. The lumen-intima interface produces a visible echo in the image, transitioning from quite low-intensity pixels (lumen) to relatively low gray tones produced by the intimal and medial layers. The intima-media interface does not produce a visible echo and, therefore, the intimal layer cannot be distinguished from the medial one. The adventitia layer is the most hyperechoic tissue, and, therefore, the media-adventita interface is visible as the transition from the relatively low gray tones to the high-intensity pixels produced by this outermost layer.

Artery Wall Measurements - IMT and IMTV

The parameter that is most commonly used to assess the progression of atherosclerosis which can be easily obtained from a B-mode ultrasound image is the **intima-media thickness** (**IMT**) [77, 78]. This parameter has been widely validated and several studies have proven the relationship between the IMT and CVDs [79, 80].

Usually, a trained operator directly calculates the IMT from the B-mode image acquired during the exam by fixing markers on the screen of the ultrasound device. This methodology, however, is highly user-dependent and is impractical in large image databases. For this reason, many recent studies have been focused on the development and implementation of semi-automated or completely automated and user-independent algorithms [10–15]. Figure 1.8 shows the manual placement of

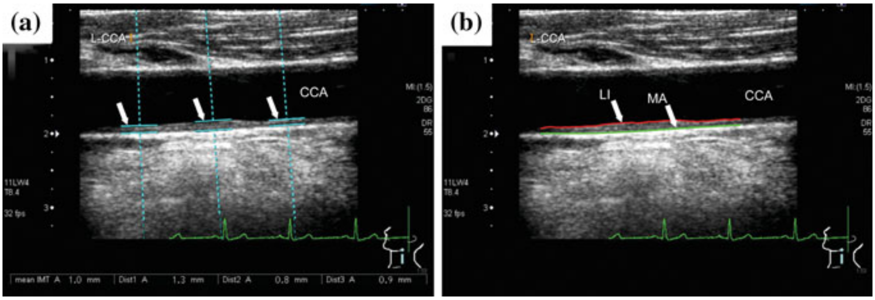

Fig. 1.8 Manual and automatic IMT segmentations. **a** Manual placement of markers along the carotid artery wall. **b** Automatic segmentation of the same image, lumen-intima profile in *red*, media-adventita in *green*

markers on a B-mode ultrasound image of the CCA and the corresponding image with the segmentation results of an automatic algorithm.

In recent studies, it has been shown that the IMT variation (IMTV) along the carotid artery wall has a stronger correlation with atherosclerosis than the value of the intima-media thickness itself [81]. In fact, the IMT variation is an estimation of the wall irregularity [81], which is a risk condition for plaque buildup. Therefore, the quantification of IMT variations along the vessel could also be an important diagnostic tool, adding more information compared to solely the IMT value by itself.

1.4.2 Cancer and Angiogenesis

Cancer results from the outgrowth of a clonal population of cells from tissue [82]. Cancer development requires the acquisition of six fundamental properties: self-sufficient proliferation, insensitivity to anti-proliferative signals, evasion of apoptosis, unlimited replicative potential, the maintenance of vascularization, and, for malignancy, tissue invasion and metastasis [83]. Cancer can also be considered with regard to a step-wise development functionally grouped into three phases: initiation, promotion, and progression [84]. Research over the last few decades has solidified the concept that tumor development and malignancy is the result of processes involving both the cancer cells themselves and non-cancer cells, and a clear example of this is illustrated by the requirement of neo-angiogenesis for tumor growth and thus the contribution of the vascular endothelial cells [82, 85].

Angiogenesis can be defined as the growth of nascent blood vessels from preexisting vessels, and it is a critically important process for both physiological (such as wound healing, reproduction and embryonic development) and pathophysiological conditions (such as solid tumor growth, psoriasis and diabetic retinopathy) [86]. Angiogenesis is a dynamic and complicated multi-step process involving the activation, migration and invasion, proliferation, sprout formation, tube formation,

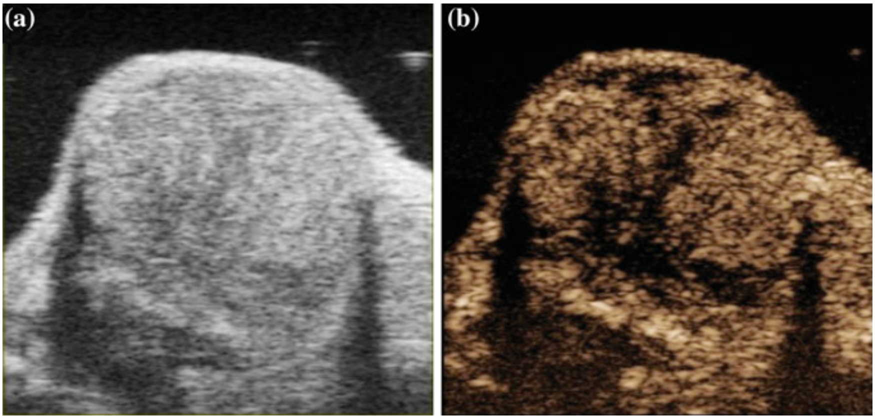

Fig. 1.9 **a** Example B-mode ultrasound image of a mouse tumor. **b** Example contrast-enhanced ultrasound image obtained after injection of micro bubble contrast agent

and finally capillary network formation of vascular endothelial cells. All of these steps are essential for the success of angiogenesis and is therefore tightly controlled directly or indirectly by the dynamic balance between angiogenic stimulators and inhibitors [86].

The vascular network can therefore be a cue to assess malicious tumor and ischemic tissues, and the accurate characterization and description of the vascular network of a cancer lesion are of paramount importance in clinical practice and cancer research in order to improve diagnostic accuracy or to assess the effectiveness of a treatment.

Ultrasound and Photoacoustic Imaging of Vascular Architecture

The use of microbubble contrast agents and contrast enhanced ultrasound (CEUS) imaging have been registered for tissue perfusion imaging and cardiac chamber border enhancement, as mentioned already in Sect. 1.2.2. Microbubble contrast agents enhance the arterial lumen, improving the delineation of the lumen. The capability of ultrasound scans to detect individual microbubbles passing though the capillary system allows direct visualization of neovascularization. Because the microbubbles are strict intravascular tracers, their presence therefore represents the presence of a neovessel [44]. Figure 1.9 displays an example of a B-mode ultrasound image and the corresponding image obtained thanks to the enhancement of microbubble contrast agents.

Photoacoustic imaging is a technique that has seen rapid growth in the last decade and it has emerged as an alternative imaging technique to noninvasively visualize microvasculature [87]. The photoacoustic wave can be generated by thermoelastic expansion subsequent to absorption of a short laser pulse. Because the contrast mechanism of photoacoustic imaging is based on optical absorption, blood vessels can be photoacoustically imaged using strong photon-absorbing chromophore

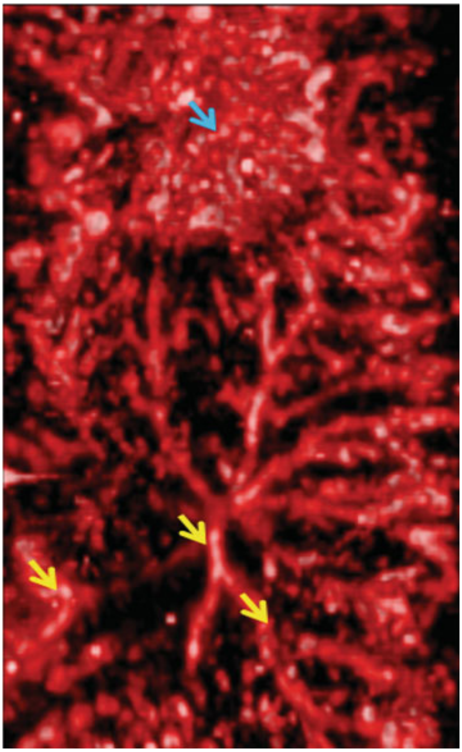

Fig. 1.10 Example of obtainable photoacoustic image of vasculature. Top view image of a photoacoustic volume, obtained at 800 nm

in the body, in particular haemoglobin, without additional support from exogenous contrast agents [88]. Also, physiological parameters such as oxygen saturation and haemoglobin concentration can be quantitatively assessed using photoacoustic imaging [89]. Figure 1.10 displays an example of a photoacoustic image of vasculature, where the blood vessels can be clearly seen.

Vascular Architecture Measurements - Tortuosity

The clinical recognition of abnormal vascular tortuosity, or excessive bending, twisting, and winding, is important to the diagnosis of many diseases [90]. In the studies that are reported in this work, three main tortuosity parameters for 3D volumes were considered:

Distance Metric (DM) This metric has been widely used in 2D, and it provides a ratio between the actual path length of a meandering curve and the linear distance between endpoints (Fig. 1.11a). The distance metric produces a dimensionless number [90].

Inflection Count Metric (ICM) The DM calculates how far a path deviates from that of a straight line; however, its usefulness is limited as it may assign the same tortuosity value to a large, gentle "C" curve as to a much more tortuous vessel that makes abrupt changes in direction. The Inflection Count Metric is defined therefore as the number

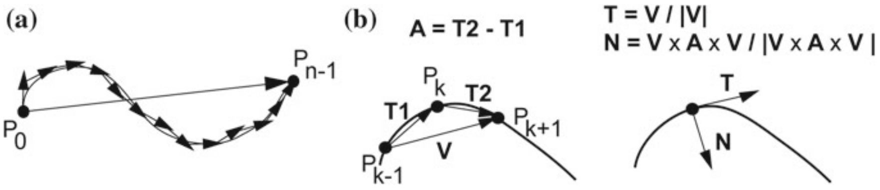

Fig. 1.11 **a** Distance Metric; The sum of distances between adjacent 3D points along the actual vessel path (*short arrows*) is divided by the length of the straight path between the first and last 3D points (*long line*). **b** Frenet frame. *Left* determination of velocity (**V**) and acceleration (**A**) vectors. *Right* derivation of the Frenet frame given the **V** and **A** vectors

of inflection points calculated along the path multiplied by the DM. An inflection point is defined as a locus that exhibits a minimum of total curvature. Considering the Frenet frame, [91], the Normal and Binormal axes change orientation by close to 180 as the frame passes through an inflection point. So, the 3D inflection points can be found by identifying large local maxima of the dot product $\Delta N \cdot \Delta N$, where N is the unit vector representing the Frenet normal axis, and ΔN is the difference of the normal axes associated with points P_k and P_{k-1}. An example of the Frenet frame and the calculation of N, which is derived by crossing the velocity and acceleration vectors, and then crossing that vector with the velocity vector and normalizing, is shown in Fig. 1.11b [90].

Sum of Angles Metric (SOAM) Neither the DM nor the ICM handles the situation of tight coils very well, which is the reason why the sum of angles metric was developed, which consists of integrating the total curvature along a curve and normalizing by path length. This approach provides a 3D, geometrically based variant of the curvature integration method described by Hart [92]. The in-plane curvature at point P_k is estimated by calculating the vector **T1** between the points P_{k-1} and P_k, and the vector **T2** between points P_k and P_{k+1}. The vectors are then normalized, the dot product is obtained, and the arccosine is calculated to provide an angle between the two vectors. If the three points are collinear, the in-plane angle will thus be reported as 0. If the three points are close to collinear, the in-plane angle is small. If the three points define a sharp peak, the in-plane angle is large [90]. A positive total angle of "curvature" at point P_k is calculated by taking the square root of the sum of the squares of the in-plane angle and of the torsional angle. The total angles are summed for each valid point in the curve, and the result is normalized by dividing by the total curve length.

Considering that $\mathbf{T1} = P_k - P_{k-1}$, $\mathbf{T2} = P_{k+1} - P_k$, and $\mathbf{T3} = P_{k+2} - P_{k+1}$, the in-plane angle at point P_k, IP_k, and the torsional angle, TP_k can be defined as:

$$IP_k = cos^{-1}((\mathbf{T1}/|\mathbf{T1}|) \cdot (\mathbf{T2}/|\mathbf{T2}|)) \tag{1.10}$$

$$TP_k = cos^{-1}((\mathbf{T1} \times \mathbf{T2}/|\mathbf{T1} \times \mathbf{T2}|) \cdot (\mathbf{T2} \times \mathbf{T3}/|\mathbf{T2} \times \mathbf{T3}|)) \tag{1.11}$$

The total angle CP_k at point P_k is then:

$$CP_k = sqrt(IP_k \times IP_k) + (TP_k \times TP_k) \tag{1.12}$$

The sum of angles metric calculates the total tortousity of the curve as [90]:

$$SOAM = \frac{\left(\sum_{k=1}^{n-3} CP_k\right)}{\left(\sum_{k=1}^{n-1} |P_k - P_{k-1}|\right)} \tag{1.13}$$

References

1. G.S. Lodwick, C.L. Haun, W.E. Smith, R.F. Keller, E.D. Robertson, Computer diagnosis of primary bone tumors: a preliminary report 1. Radiology **80**(2), 273–275 (1963)
2. P.H. Meyers, C.M. Nice Jr., H.C. Becker, W.J. Nettleton Jr., J.W. Sweeney, G.R. Meckstroth, Automated computer analysis of radiographic images 1. Radiology **83**(6), 1029–1034 (1964)
3. F. Winsberg, M. Elkin, J. Macy Jr., V. Bordaz, W. Weymouth, Detection of radiographic abnormalities in mammograms by means of optical scanning and computer analysis 1. Radiology **89**(2), 211–215 (1967)
4. R.P. Kruger, J.R. Townes, D.L. Hall, S.J. Dwyer, G.S. Lodwick, Automated radiographic diagnosis via feature extraction and classification of cardiac size and shape descriptors. IEEE Trans. Biomed. Eng. **3**, 174–186 (1972)
5. R.P. Kruger, W.B. Thompson, A.F. Turner, Computer diagnosis of pneumoconiosis. IEEE Trans. Syst. Man Cybern. **1**, 40–49 (1974)
6. J.-I. Toriwaki, Y. Suenaga, T. Negoro, T. Fukumura, Pattern recognition of chest X-ray images. Comput. Graph. Image Process. **2**(3), 252–271 (1973)
7. K. Doi, Computer-aided diagnosis in medical imaging: historical review, current status and future potential. Comput. Med. Imaging Graph. **31**(4–5), 198–211 (2007)
8. A.B. Rosenkrantz, M. Mendiratta-Lala, B.J. Bartholmai, D. Ganeshan, R.G. Abramson, K.R. Burton, J.Y. John-Paul, E.M. Scalzetti, T.E. Yankeelov, R.M. Subramaniam, et al., Clinical utility of quantitative imaging, in *Academic Radiology* (2014)
9. R. S. of North America. Quantitative Imaging Biomarkers Alliance (2014), http://www.rsna.org/QIBA.aspx. Accessed 22 Dec 2014
10. R. Rocha, A. Campilho, J. Silva, E. Azevedo, R. Santos, Segmentation of the carotid intima-media region in B-Mode ultrasound images. Image Vis. Comput. **28**(4), 614–625 (2010)
11. R. Rocha, A. Campilho, J. Silva, E. Azevedo, R. Santos, Segmentation of ultrasound images of the carotid using RANSAC and cubic splines. Comput. Methods Programs Biomed. **101**(1), 94–106 (2011)
12. C.P. Loizou, C.S. Pattichis, A.N. Nicolaides, M. Pantziaris, Manual and automated media and intima thickness measurements of the common carotid artery. IEEE Trans. Ultrason. Ferroelectr. Freq. Control **56**(5), 983–994 (2009)
13. F. Molinari, C. Pattichis, G. Zeng, L. Saba, U. Acharya, R. Sanfilippo, A. Nicolaides, J. Suri, Completely automated multi-resolution edge snapper (CAMES) : a new technique for an accurate carotid ultrasound imt measurement: clinical validation and benchmarking on a multi-institutional database, in *IEEE Transactions on Image Processing* (2011). (23 Sep 2011). [Epub ahead of print]
14. F. Molinari, K.M. Meiburger, G. Zeng, A. Nicolaides, J.S. Suri, CAUDLES-EF: carotid automated ultrasound double line extraction system using edge flow. J. Digit. Imaging **24**(6), 1059–1077 (2011)

15. K.M. Meiburger, F. Molinari, U.R. Acharya, L. Saba, P.S. Rodrigues, W. Liboni, A. Nicolaides, J.S. Suri, Automated carotid artery intima layer regional segmentation. Phys. Med. Biol. **56**(13), 4073–4090 (2011)
16. K. Taylor, P. Burns, Duplex Doppler scanning in the pelvis and abdomen. Ultrasound Med. Biol. **11**(4), 643–658 (1985)
17. S.-F. Huang, R.-F. Chang, W. Moon, Y.-H. Lee, D.-R. Chen, J. Suri, Analysis of tumor vascularity using three-dimensional power Doppler ultrasound images. IEEE Trans. Med. Imaging **27**(3), 320–330 (2008)
18. Y.-H. Huang, J.-H. Chen, Y.-C. Chang, C.-S. Huang, W. Moon, W.-J. Kuo, K.-J. Lai, R.-F. Chang, Diagnosis of solid breast tumors using vessel analysis in three-dimensional power Doppler ultrasound images. J. Digit. Imaging **26**(4), 731–739 (2013)
19. F. Molinari, A. Mantovani, M. Deandrea, P. Limone, R. Garberoglio, J. Suri, Characterization of Single Thyroid Nodules by Contrast-Enhanced 3-D Ultrasound. Ultrasound Med. Biol. **36**(10), 1616–1625 (2010)
20. D.O. Cosgrove, K.E. Chan, Renal transplants: what ultrasound can and cannot do. Ultrasound Q. **24**(2), 77–87 (2008)
21. B.F. Kurland, E.R. Gerstner, J.M. Mountz, L.H. Schwartz, C.W. Ryan, M.M. Graham, J.M. Buatti, F.M. Fennessy, E.A. Eikman, V. Kumar et al., Promise and pitfalls of quantitative imaging in oncology clinical trials. Magn. Reson. Imaging **30**(9), 1301–1312 (2012)
22. M.S. Davenport, A.M. Neville, J.H. Ellis, R.H. Cohan, H.S. Chaudhry, R.A. Leder, Diagnosis of renal angiomyolipoma with hounsfield unit thresholds: effect of size of region of interest and nephrographic phase imaging. Radiology **260**(1), 158–165 (2011)
23. C.A. Coursey, R.C. Nelson, D.T. Boll, E.K. Paulson, L.M. Ho, A.M. Neville, D. Marin, R.T. Gupta, S.T. Schindera, Dual-energy multidetector CT: how does it work, what can it tell us, and when can we use it in abdominopelvic imaging? 1. Radiographics **30**(4), 1037–1055 (2010)
24. D.T. Boll, N.A. Patil, E.K. Paulson, E.M. Merkle, W.N. Simmons, S.A. Pierre, G.M. Preminger, Renal stone assessment with dual-energy multidetector CT and advanced postprocessing techniques: improved characterization of renal stone composition-pilot study 1. Radiology **250**(3), 813–820 (2009)
25. H. Chandarana, R.P. Lim, J.H. Jensen, C.H. Hajdu, M. Losada, J.S. Babb, S. Huffman, B. Taouli, Hepatic iron deposition in patients with liver disease: preliminary experience with breath-hold multiecho T2*-weighted sequence. Am. J. Roentgenol. **193**(5), 1261–1267 (2009)
26. D.-M. Koh, D.J. Collins, Diffusion-weighted MRI in the body: applications and challenges in oncology. Am. J. Roentgenol. **188**(6), 1622–1635 (2007)
27. S. Currie, M. Hadjivassiliou, I.J. Craven, I.D. Wilkinson, P.D. Griffiths, N. Hoggard, Magnetic resonance spectroscopy of the brain. Postgrad. Med. J. (2012). postgradmedj-2011
28. D.L. Bailey, D.W. Townsend, P.E. Valk, M.N. Maisey, *Positron Emission Tomography* (Springer, New York, 2005)
29. M. Graham, L. Peterson, R. Hayward, Comparison of simplified quantitative analyses of FDG uptake. Nucl. Med. Biol. **27**(7), 647–655 (2000)
30. D. Vriens, L.-F. de Geus-Oei, H.W. van Laarhoven, J.N. Timmer-Bonte, P.F. Krabbe, E.P. Visser, W.J. Oyen, Evaluation of different normalization procedures for the calculation of the standardized uptake value in therapy response monitoring studies. Nucl. Med. Commun. **30**(7), 550–557 (2009)
31. M. Jeon, W. Song, J. Kim, J. Kim, J. Oh, J. Lovell, C. Kim, Methylene blue microbubbles (MB2) as a dual modal contrast agent for photoacoustic and ultrasound imaging, in *SPIE BiOS. International Society for Optics and Photonics* (2014), pp. 894321–894321
32. G. Kim, S.-W. Huang, K. Day, M. O'Donnell, R. Agayan, M. Day, R. Kopelman, S. Ashkenazi, Indocyanine-green-embedded PEBBLEs as a contrast agent for photoacoustic imaging. J. Biomed. Opt. **12**(4) (2007)
33. C. Kim, E. Cho, J. Chen, K. Song, L. Au, C. Favazza, Q. Zhang, C. Cobley, F. Gao, Y. Xia, L. Wang, In vivo molecular photoacoustic tomography of melanomas targeted by bioconjugated gold nanocages. ACS Nano **4**(8), 4559–4564 (2010)

34. S. Mallidi, G. Luke, S. Emelianov, Photoacoustic imaging in cancer detection, diagnosis, and treatment guidance. Trends Biotechnol. **29**(5), 213–221 (2011)
35. R. Bouchard, O. Sahin, S. Emelianov, Ultrasound-guided photoacoustic imaging: current state and future development. IEEE Trans. Ultrason. Ferroelectr. Freq. Control **61**(3), 450–466 (2014)
36. C. Hoelen, F. De Mul, R. Pongers, A. Dekker, Three-dimensional photoacoustic imaging of blood vessels in tissue. Opt. Lett. **23**(8), 648–650 (1998)
37. Y. Lao, D. Xing, S. Yang, L. Xiang, Noninvasive photoacoustic imaging of the developing vasculature during early tumor growth. Phys. Med. Biol. **53**(15), 4203–4212 (2008)
38. T. Kitai, M. Torii, T. Sugie, S. Kanao, Y. Mikami, T. Shiina, M. Toi, Photoacoustic mammography: initial clinical results. Breast Cancer **21**(2), 146–153 (2014)
39. M. Heijblom, Clinical Experiences with Photoacoustic Breast Imaging: The Appearance of Suspicious Lesions (2014)
40. W. Xia, W. Steenbergen, S. Manohar, Photoacoustic mammography: prospects and promises. Breast Cancer Manag. **3**(5), 387–390 (2014)
41. K.K. Shung, Diagnostic ultrasound: past, present, and future. J. Med. Biol. Eng. **31**(6), 371–374 (2011)
42. F. Kiessling, S. Fokong, J. Bzyl, W. Lederle, M. Palmowski, T. Lammers, Recent advances in molecular, multimodal and theranostic ultrasound imaging. Adv. Drug Deliv. Rev. **72**, 15–27 (2014)
43. V. Chan, Ultrasound for Regional Anesthesia (2007), http://www.usra.ca/. Accessed 22 Dec 2014
44. G. Kate, Carotid Artery Contrast Enhanced Ultrasound. Ph.D. thesis (2014)
45. M.L. Main, A.C. Ryan, T.E. Davis, M.P. Albano, L.L. Kusnetzky, M. Hibberd, Acute mortality in hospitalized patients undergoing echocardiography with and without an ultrasound contrast agent (multicenter registry results in 4,300,966 consecutive patients). Am. J. Cardiol. **102**(12), 1742–1746 (2008)
46. J. Powers, M. Averkiou, M. Bruce, Principles of cerebral ultrasound contrast imaging. Cerebrovasc. Dis. **27**(Suppl. 2), 14–24 (2009)
47. P. Beard, Biomedical photoacoustic imaging. Interface Focus **1**(4), 602–631 (2011)
48. A. Bell, On the production and reproduction of sound by light. Am. J. Sci. **20**(118), 305–324 (1880)
49. R. Kruger, P. Liu, Y. Fang, C. Appledorn, Photoacoustic ultrasound (PAUS) - reconstruction tomography. Med. Phys. **22**(10), 1605–1609 (1995)
50. R. Esenaliev, A. Karabutov, F. Tittel, B. Fornage, S. Thomsen, C. Stelling, A. Oraevsky, Laser Optoacoustic Imaging for Breast Cancer Diagnostics: Limit of Detection and Comparison with x-ray and Ultrasound Imaging, vol. 2979 (1997) pp. 71–82
51. A.A. Oraevsky, V.A. Andreev, A.A. Karabutov, D.R. Fleming, Z. Gatalica, H. Singh, R.O. Esenaliev, Laser Opto-Acoustic Imaging of the Breast: Detection of Cancer Angiogenesis, vol. 3597 (1999), pp. 352–363
52. S. Emelianov, Synergy and Applications of Combined Ultrasound, Elasticity, and Photoacoustic Imaging, in *IEEE International Ultrasonics Symposium* (2006)
53. L. Wang, Multiscale photoacoustic microscopy and computed tomography. Nat. Photonics **3**(9), 503–509 (2009)
54. A. Oraevsky, A. Karabutov, Optoacoustic tomography, in *Biomedical Photonics Handbook*, PM125 (2003), pp. 34/1–34/34
55. J. Xia, J. Yao, L. Wang, Photoacoustic tomography: principles and advances. Prog. Electromagn. Res. **147**, 1–22 (2014)
56. A. Oraevsky, S. Jacques, F. Tittel, Measurement of tissue optical properties by timeresolved detection of laser-induced transient stress. Appl. Opt. **36**(1), 402–415 (1997)
57. B. Cox, J. Laufer, P. Beard, The Challenges for Quantitative Photoacoustic Imaging, vol. 7177 (2009)
58. American National Standards Institute, in *American National Standard for the Safe Use of Lasers: ANSI Z136. 1-2000* (2000)

59. S. Emelianov, S. Aglyamov, A. Karpiouk, S. Mallidi, S. Park, S. Sethuraman, J. Shah, R. Smalling, J. Rubin, W. Scott, 1E-5 synergy and applications of combined ultrasound, elasticity, and photoacoustic imaging, in *Ultrasonics Symposium, 2006. IEEE* (IEEE, 2006), pp. 405–415
60. J. Xia, J. Yao, L.H.V. Wang, Photoacoustic tomography: principles and advances. Prog. Electromagn. Res. **147**, 1–22 (2014)
61. S. Hu, K. Maslov, L.V. Wang, Second-generation optical-resolution photoacoustic microscopy with improved sensitivity and speed. Opt. Lett. **36**(7), 1134–1136 (2011)
62. S. Park, C. Lee, J. Kim, C. Kim, Acoustic resolution photoacoustic microscopy. Biomed. Eng. Lett. **4**(3), 213–222 (2014)
63. J.-M. Yang, K. Maslov, H.-C. Yang, Q. Zhou, K.K. Shung, L.V. Wang, Photoacoustic endoscopy. Opt. Lett. **34**(10), 1591–1593 (2009)
64. A.B. Karpiouk, B. Wang, S.Y. Emelianov, Development of a catheter for combined intravascular ultrasound and photoacoustic imaging. Rev. Sci. Instrum. **81**(1), 014901 (2010)
65. M.A. Yaseen, M. Fronheiser, B.A. Bell, A.A. Oraevsky, M. Motamedi, S.A. Ermilov, H.-P. Brecht, R. Su, A. Conjusteau, Optoacoustic imaging of the prostate: development toward image-guided biopsy. J. Biomed. Opt. **15**(2), 021310–021310 (2010)
66. B.-Y. Hsieh, S.-L. Chen, T. Ling, L.J. Guo, P.-C. Li, Integrated intravascular ultrasound and photoacoustic imaging scan head. Opt. Lett. **35**(17), 2892–2894 (2010)
67. Y. Yuan, S. Yang, D. Xing, Preclinical photoacoustic imaging endoscope based on acousto-optic coaxial system using ring transducer array. Opt. Lett. **35**(13), 2266–2268 (2010)
68. K. Jansen, A.F. Van Der Steen, G. Springeling, H.M. Van Beusekom, J.W. Oosterhuis, G. Van Soest, Intravascular photoacoustic imaging of human coronary atherosclerosis, in *SPIE BiOS. International Society for Optics and Photonics* (2011), pp. 789904–789904
69. E.Z. Zhang, P.C. Beard, A miniature all-optical photoacoustic imaging probe, in **SPIE BiOS. International Society for Optics and Photonics** (2011), pp. 78991F–78991F
70. L. Xi, J. Sun, Y. Zhu, L. Wu, H. Xie, H. Jiang, Photoacoustic imaging based on MEMS mirror scanning. Biomed. Opt. Express **1**(5), 1278–1283 (2010)
71. J.-M. Yang, C. Favazza, R. Chen, K. Maslov, X. Cai, Q. Zhou, K.K. Shung, L.V. Wang, Volumetric photoacoustic endoscopy of upper gastrointestinal tract: ultrasonic transducer technology development, in *SPIE BiOS. International Society for Optics and Photonics* (2011), pp. 78990D–78990D
72. J.J. Badimon, B. Ibanez, G. Cimmino, Genesis and dynamics of atherosclerotic lesions: implications for early detection. Cerebrovasc. Dis. **27**(Suppl. 1), 38–47 (2009)
73. A.-M. Kampoli, D. Tousoulis, C. Antoniades, G. Siasos, C. Stefanadis, Biomarkers of premature atherosclerosis. Trends Mol. Med. **15**(7), 323–332 (2009)
74. M. Walter, Interrelationships among HDL metabolism, aging, and atherosclerosis. Arterioscleгo. Thromb. Vasc. Biol. **29**(9), 1244–1250 (2009)
75. F. Molinari, G. Zeng, J.S. Suri, A state of the art review on intima-media thickness (IMT) measurement and wall segmentation techniques for carotid ultrasound. Comput. Methods Programs Biomed. **100**, 201–221 (2010)
76. S. Delsanto, F. Molinari, P. Giustetto, W. Liboni, S. Badalamenti, J.S. Suri, Characterization of a completely user-independent algorithm for carotid artery segmentation in 2-D ultrasound images. IEEE Trans. Instrum. Meas. **56**(4), 1265–1274 (2007)
77. P. Touboul, et al., Mannheim carotid intima-media thickness consensus (2004–2006), in **An update on behalf of the Advisory Board of the 3rd and 4th Watching the Risk Symposium, 13th and 15th European Stroke Conferences, Mannheim, Germany, 2004, and Brussels, Belgium, 2006. Cerebrovascular Diseases**, vol. 23 (2007), pp. 75–80
78. P.J. Touboul, M.G. Hennerici, S. Meairs, H. Adams, P. Amarenco, M. Desvarieux, S. Ebrahim, M. Fatar, R. Hernandez Hernandez, S. Kownator, P. Prati, T. Rundek, A. Taylor, N. Bornstein, L. Csiba, E. Vicaut, K.S. Woo, F. Zannad, Mannheim intima-media thickness consensus. Cerebrovasc. Dis. **18**(4), 346–349 (2004)
79. P.-J. Touboul, A. Elbaz, C. Koller, C. Lucas, V. Adraï, F. Chédru, P. Amarenco, G. Investigators et al., Common carotid artery intima-media thickness and brain infarction the étude du profil génétique de l'infarctus cérébral (génic) case-control study. Circulation **102**(3), 313–318 (2000)

80. G. de Simone, R. McClelland, J.S. Gottdiener, A. Celentano, R.A. Kronmal, J.M. Gardin, Relation of hemodynamics and risk factors to ventricular-vascular interactions in the elderly: the Cardiovascular Health Study. J. Hypertens. **19**(10), 1893–1903 (2001)
81. I.M. Graf, F.H. Schreuder, J.M. Hameleers, W.H. Mess, R.S. Reneman, A.P. Hoeks, Wall irregularity rather than intima-media thickness is associated with nearby atherosclerosis. Ultrasound Med. Biol. **35**(6), 955–961 (2009)
82. S. Rakoff-Nahoum, Cancer issue: why cancer and inflammation? Yale J. Biol. Med. **79**(3–4), 123 (2006)
83. D. Hanahan, R.A. Weinberg, The hallmarks of cancer. Cell **100**(1), 57–70 (2000)
84. K.W. Kinzler, B. Vogelstein, Lessons from hereditary colorectal cancer. Cell **87**(2), 159–170 (1996)
85. J. Folkman, Role of angiogenesis in tumor growth and metastasis, in *Seminars in Oncology*, vol. 29, no. 6 (Elsevier, 2002), pp. 15–18
86. X. Feng, Angiogenesis and antiangiogenesis therapies: spear and shield of pharmacotherapy. J. Pharma. Care Health SysT. **1**, e110 (2014)
87. S. Hu, L.V. Wang, Photoacoustic imaging and characterization of the microvasculature. J. Biomed. Opt. **15**(1) (2010)
88. G.P. Luke, D. Yeager, S.Y. Emelianov, Biomedical applications of photoacoustic imaging with exogenous contrast agents. Ann. Biomed. Eng. **40**(2), 422–437 (2012)
89. B. Cox, J.G. Laufer, S.R. Arridge, P.C. Beard, Quantitative spectroscopic photoacoustic imaging: a review. J. Biomed. Opt. **17**(6), 0612021–06120222 (2012)
90. E. Bullitt, G. Gerig, S.M. Pizer, W. Lin, S.R. Aylward, Measuring tortuosity of the intracerebral vasculature from MRA images. IEEE Trans. Med. Imag. **22**(9), 1163–1171 (2003)
91. J.J. Koenderink, *Solid Shape*, vol. 2 (Cambridge Univ Press, Cambridge, 1990)
92. W.E. Hart, M. Goldbaum, B. Côté, P. Kube, M.R. Nelson, Measurement and classification of retinal vascular tortuosity. Int. J. Med. Inf. **53**(2), 239–252 (1999)

Chapter 2
Automated IMT Carotid Artery Far Wall Segmentation Techniques

Abstract This Chapter focuses on the development and validation of quantitative techniques for the assessment of vascular morphological parameters that can be extracted from B-mode ultrasound longitudinal images of the common carotid artery. In particular, results from numerous past studies (Molinari et al., Comput. Methods Progr. Biomed. 108, 946–960, 2012, [1], Molinari et al., Software. Int. Angiol. 31(1), 42–53, 2012, [2], Ikeda et al., Int. Angiol. J. Int. Union Angiol. 32(3), 339–348, 2013, [3], Saba et al., Diabet. Res. Clin. Pract. 100(3), 348–353, 2013, [4], Molinari et al., Med. Phys. 39(1), 378–391, 2012, [5], Meiburger et al., GIMT: Generalized IMT measurement in carotid ultrasound images with plaque: an automated method, [6]) will be presented, ranging from the validation of techniques for correctly locating the CCA in B-mode ultrasound images, the development and implementation of novel completely automated techniques for the IMT measurement and plaque segmentation, and the validation and association of the automatically measured IMT value with clinical parameters.

2.1 Introduction

As briefly mentioned in Sect. 1.4.1, atherosclerosis is a cardiovascular disease (CVD), which causes a thickening of the arterial walls and stenosis, affecting healthy blood flow. Various studies have demonstrated how the risk of CVDs and the characteristics of the carotid artery wall are strongly correlated [7].

The intima-media thickness (IMT) is a widely used and reliable early indicator of this pathology, and is also used to mark the progression of carotid artery (CA) disease [8]. During the early stages of atherosclerosis, the intima-media complex is enclosed by the lumen and the adventitia, whose boundary is defined by two parallel interfaces, the lumen-intima (LI) interface and the media-adventitia (MA) boundary. Carotid plaques, on the other hand, are the growing regions located on the walls of the carotid artery. When plaque with significant local thickening exists, its shape can differ greatly from the traditional double-layered structure found along the artery wall.

K.M. Meiburger, *Quantitative Ultrasound and Photoacoustic Imaging for the Assessment of Vascular Parameters*, PoliTO Springer Series,
DOI 10.1007/978-3-319-48998-8_2

There have also been various large-scale and multi-center projects on the topic of artery wall thickness (Improve QLG1-CT-2002-00896; PROG-IMT project). In particular, The IMPROVE study, carried out from 2003 to 2007, was a prospective, multicenter, longitudinal, observational study designed to investigate whether cross-sectional carotid artery intima media thickness and overall IMT progression are predictors of future vascular events in European individuals at high risk of cardiovascular diseases [9–12]. The PROG-IMT project aimed to combine individual data from large IMT prospective studies to investigate whether individual IMT progression can be used as a surrogate for vascular risk [13]. Findings from these studies show how an important carotid ultrasonic variable that may have predictive capacity, alone or when integrated with conventional or non conventional risk factors, is the progression of carotid IMT. Accurate computer algorithms that can automatically measure the IMT in all images coming from these various centers can provide a huge benefit, removing the inter- and intra-operator variability that affects manual readings, and the tedious time-consuming manual measurement.

Since the work by Pignoli et al. [14], computer systems have been used to aid the clinician in IMT measurement. In a recent review, Molinari et al. [15] described all the most-used and performing techniques that have been developed for carotid IMT measurement. More than 40 different algorithms have been proposed for IMT measurement. This is because there are several challenges in IMT measurement in ultrasound images. Ultrasound images are always affected by speckle (caused by multiple ultrasound reflections) and often by artifacts (e.g., shadow cones caused by calcium). Then, the CA morphology is very variable and the artery can be represented as horizontal, inclined, or even curved. Also, ultrasound scanners have different resolutions and dynamic ranges, resulting in a very variable representation of the CA walls, in terms of size and brightness. Moreover, a standard acquisition protocol lacks, and this introduces further variability in images acquired by different Institutions. Finally, when atherosclerosis advances, the CA might show a plaque buildup.

The segmentation process of the intima-media complex can conceptually be thought of as two cascading stages:

- Stage I: recognition of the common carotid artery and delineation of the far adventitia layer (AD_F) in the two-dimensional B-mode ultrasound image;
- Stage II: tracing of the LI/MA wall boundaries in the region-of-interest (ROI) of the recognized CCA.

In Stage I, the carotid artery must be correctly located within the ultrasound image frame. This stage is generally better performed by human experts, who can mark the position of the CCA by either tracing rectangular regions-of-interest (ROI) or by placing markers. In Stage II, a guidance zone is created and, within this guidance zone, the LI and MA borders are estimated. The IMT can then be subsequently measured. These two stages cannot be independent of each other. In fact, in the case of completely automated algorithms, Stage I is of utmost importance since the found AD_F profile is used as a starting point for Stage II. The performance of Stage I directly affects the initialization of Stage II, and, therefore, also affects the final results. This fact emphasizes the importance of the need of an accurate yet versatile technique to perform Stage I.

In order to achieve complete automation, both of these stages must be designed to be independent of the user. To do so, first of all, appropriate detection strategies are required to automatically locate the carotid artery in the image. These strategies must be robust with respect to noise and must be able to process carotids with different geometrical appearances.

The majority of the algorithms proposed in literature for the automated segmentation of the CCA in ultrasound images requires a certain degree of user-interaction, which precludes complete automation. Any user-interaction also slows down the analysis process and introduces a dependence on the operator if gain settings are not optimal, bringing subjectivity into the process. As mentioned previously, complete automation can instead be an asset for multi-center large studies since it enables the processing of large image databases.

2.2 Materials and Methods

2.2.1 Performance Metric Evaluation for Carotid Artery Recognition Systems

This section is dedicated to the performance metric evaluation for ultrasound carotid wall segmentation, showing the comparative characterization of Stage I of three completely automated paradigms, CAMES, CALEX, and CULEX, and is based on the work done in [5].

CAMES (Completely Automated Multiresolution Edge Snapper) is based on multi-resolution analysis and scale-space analysis [16]. CALEX (Completely Automated Layered Extraction using an Integrated Approach) detects the carotid artery by relying on a combined approach of feature extraction, fitting, and classification [17]. CULEX (Computed User Layered EXtraction using a Signal Analysis approach) is based on local statistics and distribution of the pixels and its features [18, 19].

300 images coming from two different Institutions were used for this evaluation. Two hundred images were acquired using the same ultrasound scanner at the Neurology Department of Torino, Italy, from one hundred and fifty asymptomatic patients who were referred to the Neurology Division for carotid assessment (age: 69 ± 16 years old; range: 50–83 years old). The remaining one hundred images were acquired at the Cyprus Institute of Neurology (Nicosia, Cyprus) from symptomatic patients (age: 54 ± 24 years old; range: 25–95 years old) using a Philips ATL HDI 3000 ultrasound scanner equipped with a linear 7–10 MHz probe. Both of the Institutions made sure to obtain written informed consent from the patients prior to enrolling them in the study. Both the experimental protocol and the data acquisition procedure were approved by the respective local Ethical Committees. Three different expert sonographers (a cardiologist, a vascular surgeon, and a neurologist) independently manually segmented the images by tracing the boundaries of the lumen-intima (LI) and media-adventitia (MA) interfaces, and the average tracings were considered as ground truth (GT).

The performance of the far adventitial border automated tracing was assessed in two ways: by computing the Hausdorff distance (HD) between (a) the $\mathrm{AD_F}$ and the ground-truth average LI profile (GT-LI), and (b) the $\mathrm{AD_F}$ and the ground-truth average MA profile (GT-MA). The HD between $\mathrm{AD_F}$ and the GT-LI borders is symbolized as $H_{GT-LI}^{AD_{\mathrm{F}}}$, while the HD between $\mathrm{AD_F}$ and the GT-MA borders is symbolized as $H_{GT-MA}^{AD_{\mathrm{F}}}$.

To assess the quality of the carotid artery recognition, a threshold was fixed on the $H_{GT-LI}^{AD_{\mathrm{F}}}$ and $H_{GT-MA}^{AD_{\mathrm{F}}}$ values, in a way that the carotid artery can be considered as being correctly identified when $H_{GT-LI}^{AD_{\mathrm{F}}}$ is lower than 60 pixels ($\Delta_{lim_{pixels}}$).

The Hausdorff distance [20] is defined as the maximum distance of a boundary A to the nearest point in the Boundary B. If *a* represents a point on Boundary A and *b* represents a point on Boundary B, then for every point *a* on boundary A, the Euclidean Distance is calculated (indicated by d_{HD} in Fig. 3.1a) from *a* to Boundary B and choose the minimum distance for that point *a*. The process is repeated for all the points *a* on Boundary A and find the maximum distance for the Boundary A with respect to Boundary B, max_{AB}. The same process is repeated for all the points b on Boundary B, and the maximum distance for the Boundary B with respect to Boundary A, max_{BA}, is recorded. The greater value between max_{AB} and max_{BA} is taken as the HDM value. This distance metric was used in other studies by Destrempes et al. [21] and Loizou et al. [22].

CAMES

Stage I of the automated technique CAMES is based on multi-resolution analysis and Gaussian higher-order filtering, and it consists of a novel and low-complexity procedure.

Starting from the automatically cropped image (Fig. 2.1a), the automated Stage I is divided into different steps described in detail here:

- *Step 1: Fine to coarse down-sampling.* The image is first down-sampled by a factor of two (*i.e.*, the number of rows and columns of the image is halved) (Fig. 2.1b) implementing the down-sampling method discussed by Ye et al [20], adopting a bi-cubic interpolation. This method was tested on ultrasound images and showed a good accuracy and a low computational cost [20].
- *Step 2: Speckle reduction.* Speckle noise is attenuated using a first-order local statistics filter (called *lsmv* by the authors [23, 24], which has given the best performance in the specific case of carotid imaging. Figure 2.1c shows the despeckled image.
- *Step 3: Higher order Gaussian derivative filter.* The despeckled image is then filtered using a first-order derivative of a Gaussian kernel [16]. The white horizontal stripes in Fig. 2.1d show the proximal (near) and distal (far) adventitia layers.
- *Step 4: Automated far adventitia (AD_F) tracing.* Figure 2.1e shows the intensity profile of one column (from the upper edge of the image to the lower edge of the image) of the Gaussian filtered image. The proximal (near) and distal (far) walls are clearly identifiable as intensity maxima saturated to the maximum value of 255. A heuristic search is then applied to the intensity profile of each column

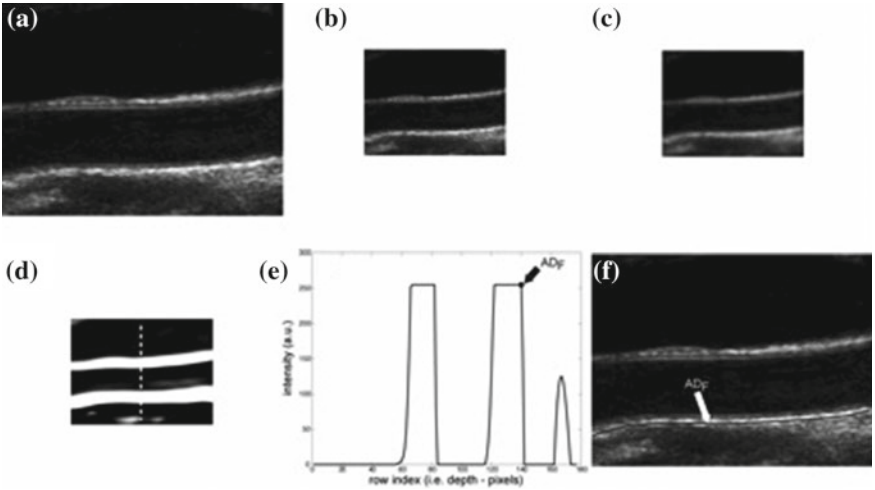

Fig. 2.1 CAMES procedure for AD_F tracing. **a** Original cropped image. **b** Down-sampled image. **c** Despeckled image. **d** Image after convolution with first-order Gaussian derivative. **e** Intensity profile of the column indicated by the vertical *dashed line* in panel **d**. (AD_F indicates the position of the far adventitia wall). **f** Cropped image with far adventitia profile overlaid

to automatically trace the profile of the distal wall. The overall automated AD_F tracing is found as the sequence of points resulting from the heuristic search for all of the image columns.

- *Step 5: Up-sampling of the far adventitia (AD_F) boundary locator.* The AD_F profile that is found is then subsequently up-sampled to the original fine scale and superimposed over the original cropped image (Fig. 2.1f) for both visualization and performance evaluation.

This multi-resolution method prepares the vessel wall's edge boundary so that the thickness of the vessel wall is roughly equivalent to the scale of the Gaussian kernel. This allows an optimal detection of the CCA walls since when the kernel is located close to a near gray level change, it enhances the transition. Consequently, the most echoic image interfaces are enhanced to white in the filtered image. This fact, as clearly shown in Fig. 2.1d, e, is what allows this procedure to detect the far adventitia layer.

CALEX

The Stage I algorithm of CALEX exploits the image information in order to automatically detect the near and far adventitia, presenting an approach that is based on feature extraction and fitting. The local intensity maxima of each column are processed by a linear discriminator to detect which are located on the CCA wall. These points are called "seed points". Seed points are then linked to form line segments. An intelligent procedure is applied to removes short or false line segments by computing the *validation* probability and joins close and aligned segments by computing the *connectability* probability. This procedure avoids over-segmentation

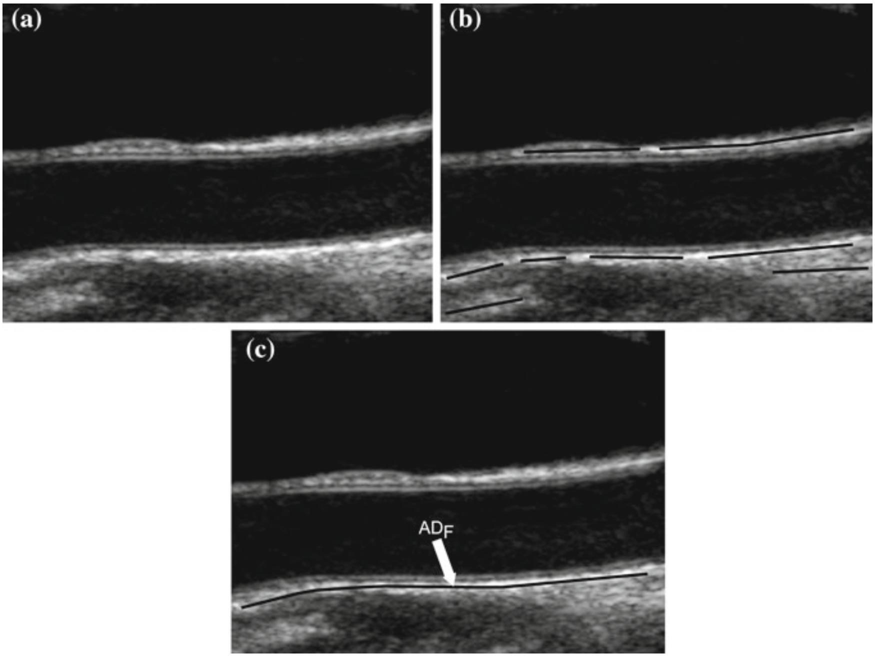

Fig. 2.2 CALEX (integrated approach) recognition strategy. **a** Original image. **b** Automatically identified *line* segments (*black lines*). **c** Final AD$_F$ tracing after line segments validation and combination

of the artery wall. Therefore, line segments classification extracts the line pair that contains the artery lumen in between (Fig. 2.2). The definitions of the *validation* and *connectability* probabilities can be found in [17].

CULEX

The Stage I algorithm of CULEX presents a local statistics approach and is based on the assumption that carotid representation can be thought of as a mixture model with varying intensity distributions. This is because (a) the pixels belonging to the vessel lumen are characterized by low mean intensity and low standard deviation; (b) pixels belonging to the adventitia layer of the carotid wall are characterized by high mean intensity and low standard deviation; and (c) all remaining pixels should have high mean intensity and high standard deviation. As a result, a bi-dimensional histogram (2DH) of the carotid image was derived. Previous studies have shown that pixels belonging to the lumen of the artery are usually classified into the first classes of this 2DH [19]. Figure 2.3 shows the lumen region selection process in four images: Fig. 2.3a depicts the original image after automatic cropping; Fig. 2.3b depicts the 2D histogram (2DH) showing the relationship between the normalized mean and normalized standard deviation. The gray region in the 2DH represents what is considered as the lumen region of the carotid artery. All the image pixels falling into this region have been depicted in gray in Fig. 2.3c. This example shows

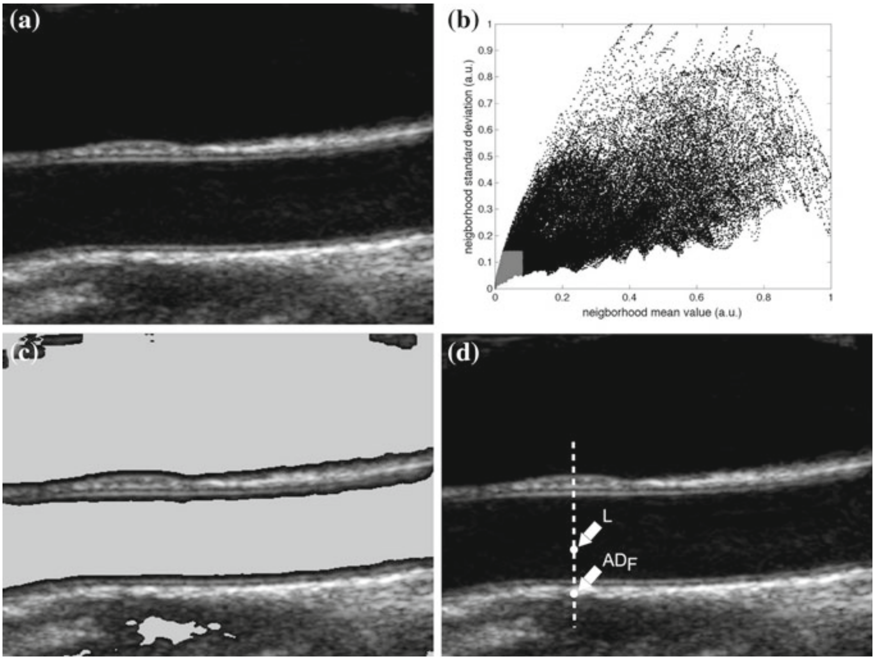

Fig. 2.3 CULEX strategy for far wall adventitial tracing. **a** Original image. **b** Bi-dimensional histogram (2DH). The *gray* portion of the 2DH denotes the region in which we suppose to find only lumen pixels. **c** Original image with lumen pixels overlaid in *gray*. **d** Sample processing of one column, with the marker points of the far (AD$_F$) adventitia layer and of the lumen (L)

how the local statistic is effective in detecting image pixels that can be considered as belonging to the CCA lumen.

Schematically, the following are the steps for processing the intensity profile:

- *Step 1: AD$_F$ tracing.* The procedure starts from the bottom most point and searches for the first maxima with an intensity value above the 90th percentile of the intensity distribution along that profile. This point is marked as a possible far adventitia (AD$_F$) candidate.
- *Step 2: Lumen tracing.* For a lumen estimation point, the algorithm moves upwards along the row (decreasing row value) and searches for a pixel (point) possibly belonging to the lumen. The lumen candidate is the first minima point whose neighborhood mean intensity and standard deviation values matched the criteria of the 2DH.

When the two candidate points along the column are found, they are plotted on the original image in correspondence with their row index (and the column index under analysis). Figure 2.3d shows the marked points on a sample image column.

2.2.2 GIMT: Generalized IMT Measurement in Carotid Ultrasound Images with Plaque: An Automated Method

Numerous automated techniques for the IMT measurement were previously developed and validated, with methods based on: (1) the mean shift classification applied to the far wall [25], (2) image feature extraction and line fitting and the first order absolute moment [26, 27], (3) an Edge Flow technique based on directional probability maps using the attributes of intensity and texture [28], and (4) a dual snake-based parametric model [29, 30]. These methods, however, were developed for the automated segmentation of the intima-media complex *without* the presence of plaque along the wall, which presents a challenge for automated segmentation techniques.

This section concentrates on the development of a completely automated algorithm for the segmentation of the common carotid artery far wall [6]. The technique was developed to function considering (1) the calculation of the intima-media thickness, for healthy carotids or the beginning stages of atherosclerosis which present a thickening of the intima-media layer, and (2) plaque segmentation, for atherosclerotic carotids which portray an obvious protrusion of the intima-media layer into the lumen area.

Two hundred and eighteen Japanese patients (163 males, 55 females, mean age 71 ± 11 years) admitted to Toho University Ohashi Medical Center from December 2008 to January 2011 who underwent carotid-US and first coronary angiography were analyzed. Coronary angiography was performed to evaluate ischemic heart disease or cardiomyopathy as the preoperative investigation for ischemic heart, aortic, or valvular disease. The study complied with the Declaration of Helsinki, and written informed consent was obtained from all patients. From the 218 patients, an image database containing 735 images was created. All patients presented a SYNTAX score higher than 0, with evidence of coronary artery disease.

Stage-I: Far Adventitia Estimation (CCA Recognition)

The first step of CA localization in the ultrasound image is done automatically thanks to a low-complexity procedure which detects the far adventitia border (AD_F) using a method based on scale-space multi-resolution analysis, as presented in Sect. 2.2.1. An example of AD_F segmentation can be seen in Fig. 2.4a.

Stage-II: Automatic Lumen-Intima and Media-Adventitia Border Segmentation

This second step is based on the technique as proposed by Rocha et al. [31, 32], a semi-automatic method in which the user was required to manually insert at least two points along the lumen medial axis of the image. These points were then used to define a region-of-interest (ROI) in the original image. Since the new GIMT algorithm is completely automated, this user-dependency was overcome by automatically defining the ROI without any interaction with the operator, thanks to the AD_F profile, which was automatically traced in Step-I. In fact, a preliminary position of the lumen axis was estimated by taking the AD_F profile and shifting it towards the lumen by a

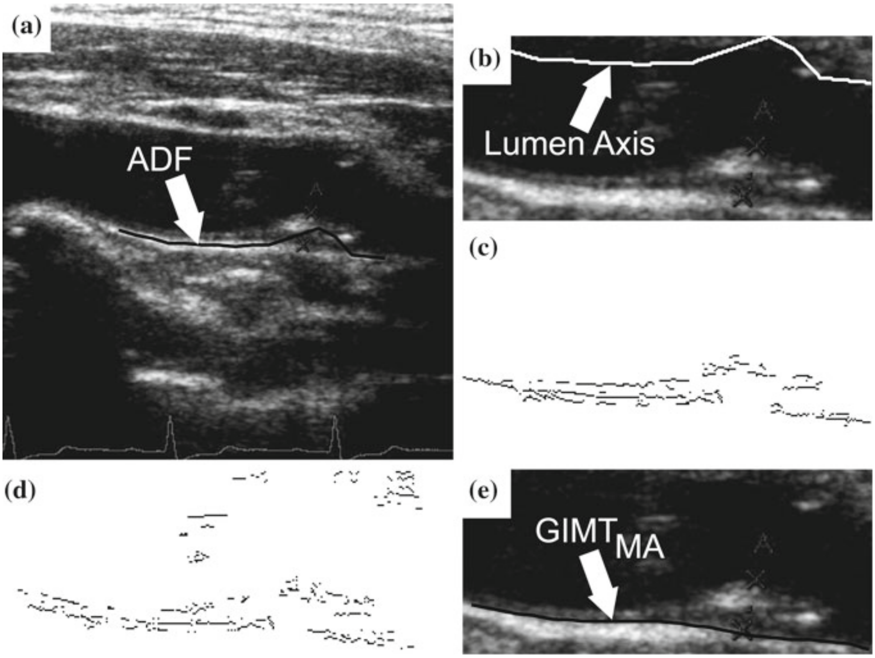

Fig. 2.4 MA estimation summary. **a** Original image with AD_F profile; **b** Region of Interest (ROI) with estimated lumen axis; **c** Final edge map; **d** Valley edge map; **e** ROI image with final estimated MA boundary

distance of Δ. An initial value of Δ was taken to be 6 mm. A check was then done to make sure that the determined lumen axis was not too high (i.e., along the proximal wall or in the jugular vein), or too close to the distal wall which could be problematic in the case of an echogenic plaques. The initial lumen axis was therefore shifted upwards or downwards accordingly, and Δ was also lowered or raised accordingly. The ROI was then defined as the smallest rectangle containing all pixels between the AD_F profile and the estimated lumen axis profile Fig. 2.4b. Finally, a lumen-check based on local statistics was performed to ensure that the ROI comprised all the wall and portion of the lumen pixels, and to get an approximation of the image noise level present in the lumen [19].

Media-adventitia border estimation using RANSAC Once the ROI has been automatically computed with the estimation of the lumen axis profile, a rough estimate of the lumen region can be estimated with the triangle thresholding algorithm [33]. A signed distance to the carotid lumen boundaries, SDL, having negative values inside the lumen region, can then be determined.

An initial low noise edge map is then computed using a new smoothing filter [34], non-maxima suppression and hysteresis thresholding. This map was obtained by borrowing concepts from robust statistics and the total variation theory [35, 36]. The instantaneous coefficient of variation ($ICOV$) [37, 38], an edge detector that is well adapted to ultrasound images, was integrated to measure the edge strength, and non-maxima suppression and hysteresis [39] was used to select the strongest edges. The $ICOV$ value at pixel (x, y) is given by:

$$ICOV(x, y) = \sqrt{\frac{\left|\frac{1}{2}\|\nabla I(x, y)\|^2 - \frac{1}{16}\Big(\nabla^2 I(x, y)\Big)^2\right|}{\Big(I(x, y) + \frac{1}{4}\nabla^2 I(x, y)^2\Big)^2}} \tag{2.1}$$

Where $I(x, y)$ represents the image intensity at (x, y), $\nabla I(x, y)$ is the intensity gradient at (x, y), $\|\nabla I(x, y)\|^2 = 0.5\Big[\|\nabla_{-} I(x, y)\| + \|\nabla_{+} I(x, y)\|^2\Big]$, $\nabla_{-} I(x, y) = \Big(I(x, y) - I(x-1, y), I(x, y) - I(x, y-1)\Big)$, $\nabla_{+} I(x, y) = \Big(I(x+1, y) - I(x, y), I(x, y+1) - I(x, y)\Big)$, $\nabla^2 I(x, y) = I(x+1, y) + I(x-1, y) + I(x, y+1) + I(x, y-1) - 4I(x, y)$, and $\|(u, v)\| = \sqrt{u^2 + v^2}$ is the norm of a vector (u, v). This new model inhibits diffusion not only where the ICOV is high, but also where the curvature is small, and also smooth outs the noise in the image since it generally has high curvature and low $ICOV$. Intensity gradient orientation errors can then be reduced by computing the local dominant gradient direction.

The final edge map (Fig. 2.4c) is then computed by only keeping the edges that are compatible with the MA boundary. In particular, only the edges that, at a given pixel, have an angle between the intensity gradient and the gradient of the distance map to the estimated medial axis below 30, are kept. Moreover, all edges in the ROI whose distance to the lumen axis is greater than d_{max} are also removed. A value of d_{max} equal to Δ was taken.

The geometry of the MA contour is modeled by a cubic spline with five control points. The search for the best fit of the cubic spline is implemented through a random sample consensus (RANSAC) algorithm. This search repeatedly extracts a random sample, with the least number of data points that are required to determine the model parameters. The consensus of the fitted spline is measured by a gain function:

$$G = \frac{1}{2m}\sum_{k=1}^{m}\Big[g_1(P_k) + g_2(P_k)\Big]g_3(P_k)g_4(P_k) \tag{2.2}$$

where P_k is a MA model point, m is the number of P_k points of the digital spline and $g_j(P_k) \leq j \leq 4$ is a fuzzy function representing the contribution of feature j at P_k. This function integrates four different discriminating features of the carotid boundaries: the proximity of the geometric model to any edge (g_1) (Fig. 2.4c) or to valley shaped edge pixels (g_2) (Fig. 2.4d); the consistency between the orientation of the normal to the geometric model and the intensity gradient (g_3); and the distance to a rough estimate of the lumen boundary (g_4). More detailed descriptions of each of these features can be found in [32]. The consensus of the model is then evaluated on the remaining population and the model with the best consensus is selected as the final cubic spline that best fits the MA border. To avoid accidentally segmenting the LI border in this step, the edges found in the estimated lumen and a little bit below it were removed from the final version of the edge map. A check was done on the distance between the found MA border and the detected $\mathrm{AD_F}$ border, so if the distance was found to be too large, indicating a likely erroneous LI tracing, edges found farther below the detected lumen were again removed. Figure 2.4e shows the ROI with the final estimated MA boundary.

Lumen-intima border estimation using dynamic programming Once the MA border has been properly segmented, the completely automated technique must then segment the LI boundary in order to correctly determine the IMT. Since many plaques are hypoechoic, presenting low contrast between the lumen and the plaque, the image is analyzed and a method based on the luminosity histogram and the estimated lumen region is used to determine whether or not the image could be hypoechoic. If the image is found to be hypoechoic, the image contrast is increased with a 0.35 gamma correction and then speckle noise is further removed, using the method proposed by [23, 24] with 3 iterations and a $7x7$ neighborhood. If the image is found instead to be hyperechoic, the image pixel intensity values are normalized (lumen to 0, adventitia layer to 190) [40] and speckle noise is removed with 2 iterations and a $3x3$ neighborhood. The $ICOV$ and edge images are recalculated using the newly processed image. Furthermore, edges found right above the MA profile and above the estimated lumen axis profile are removed. The method proposed for the detection of the lumen-intima boundary uses dynamic programming (DP) to search for the best lumen path [31]. It can be summarized as follows:

1. Set $E_{all}(x, y) = 1$ if (x, y) is a local maximum of the $ICOV$ in the direction of $\nabla I(x, y)$. Otherwise, $E_{all}(x, y) = 0$. E_{all} is the edge map with all of the edges but without any constraint on the edge strength, as measured by $ICOV$ (Fig. 2.5b).
2. Set $E_{strong}(x, y) = E_{all}(x, y)$ if $ICOV(x, y) > T$, where T is a threshold automatically estimated with robust statistics [34]. Otherwise, set $E_{strong}(x, y) = 0$.
3. Set $E(x, y) = E_{all}(x, y)$ if $(x, y) \in \Omega$, where Ω is the region delimited by the detected MA border and the estimated lumen medial axis. Otherwise, $E(x, y) = 0$.
4. Set $E(x, y) = 0$ and $E_{strong}(x, y) = 0$ if $\gamma(x, y) \geq 90$, where γ is the angle between $\nabla I(x, y)$ and $\nabla D(x, y)$, and D is the distance map to the lumen medial axis, SDL. This removes the edges that have a gradient pointing inwards toward the artery. Figure 2.5c shows the strong edges after removing these edges.
5. If $E(x, y) = 1$, compute $ICOV^{*}(x, y) = \frac{ICOV(x,y)}{\max\limits_{y}(ICOV(x,y))}$, the normalized $ICOV$ at (x, y) in the vertical direction. This procedure gives a chance to the usually weaker lumen boundary edges to compete with the stronger MA edges.
6. Set $E(x, y) = 1$ if $E_{strong}(x, y) = 1$ and there are no other edges in E_{strong} between (x, y) and the lumen axis, in the vertical direction. Set $ICOV^{*}(x, y) = 1$ for these edges.
7. Using dynamic programming, look for the path in the final edge map E (Fig. 2.5d), between the first and last columns of the ROI that minimizes the cost function:

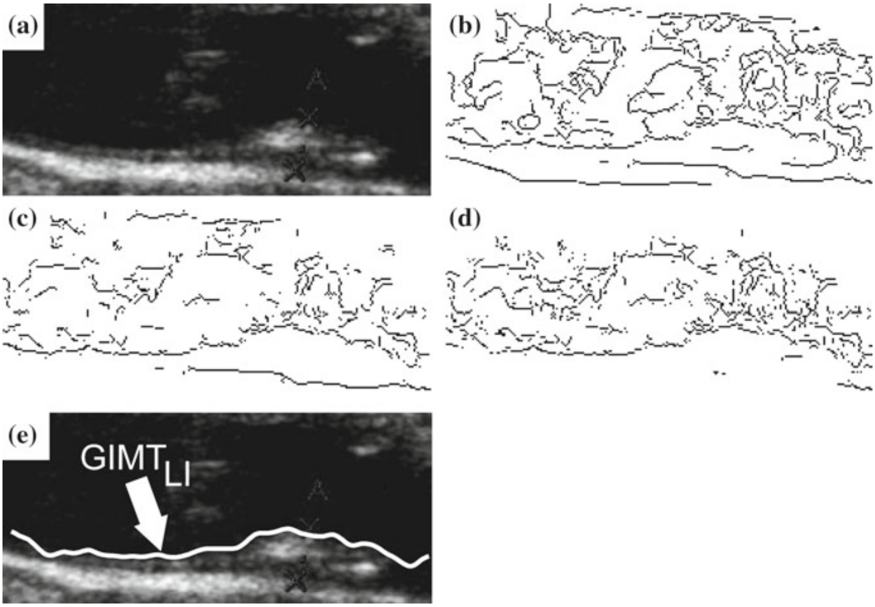

Fig. 2.5 LI estimation summary. **a** Original ROI image; **b** Edge map E_{all} with all edges, both strong and weak; **c** Edge map E_{strong} containing only strong edges after removing edges with a gradient direction incompatible with the intima layer; **d** Final version of edge map E; **e** ROI image with final estimated LI boundary

$$C_t = \sum_{j=1}^{N} \Psi(x_j, y_j) \tag{2.3}$$

where $\Psi(x_j, y_j) = 1 - ICOV^*(x_j, y_j)$ if $E(x_j, y_j) = 1$ and $\Psi(x_j, y_j) = 1$ if not; N is the number of columns in the ROI.

Performance Metric and Statistics

A medical expert (Reader) manually segmented all the images by tracing the lumen-intima (LI) and media-adventitia (MA) profiles using ImgTracer™(Global Biomedical Technologies, Inc., CA, USA) [41]. The manual segmentations were considered as ground truth (GT) for computing the system performance of the computer-generated LI/MA segmentations and IMT measurements. The performance of GIMT was benchmarked to that of the semi-automatic algorithm, RANSAC, which requires the user to manually select at least two points along the lumen medial axis.

All the IMT values obtained by GIMT and RANSAC were compared to the Reader's tracings (Ground Truth). For each image, the IMT bias was measured as the difference between the computer-based value and the value as measured by the reader. The Figure-of-Merit (FoM) [42] was also calculated to give an overall assessment of the algorithm performances. To estimate the carotid intima-media thickness variability, the IMTV values for each image was measured. To calculate both the IMT and IMTV values, the Polyline Distance Method was adopted [43]. The Polyline distance is briefly the average distance between the points on one boundary and the segments of the other boundary. It is described in much more detail in Chap. 3 and was extensively used by authors in [27, 44].

Moreover, since plaque segmentation is being considered, the area of the plaque was measured, along with the area percentage difference compared to Ground Truth, the Dice's coefficient, precision, recall and f-measure of the plaque area.

Finally, correlation plots were performed to assess the relationship between the max IMT/IMTV values for each patient versus the Plaque Score and the percent value of HbA1c. Correlation was numerically measured by using the Pearson ρ coefficient. The statistical existence of correlation between the variables was measured by the correlation level of significance (correlation was considered significant if the p value was lower than 0.05).

2.2.3 Validation of the Techniques and Association of the Automated IMT Measurement with Clinical Parameters

As already stated, automated and high performance carotid intima-media thickness (IMT) measurement is gaining increasing importance in clinical practice to assess the cardiovascular risk of patients. Numerous methods have also been developed because it has been observed that different techniques had different performances in presence of diverse noise sources. It is therefore important to understand the portability of the available techniques, and their possible downfalls. It is also of fundamental importance to understand if the automated IMT measurement obtained from these algorithms associates with clinical parameters or not.

To confront these issues, various studies were done:

1. Four fully automated IMT measurement techniques (CALEX, CAMES, CARES and CAUDLES) and one semi-automated technique (FOAM) were compared on a large multi-ethnic and multi-institutional database [1].
2. The automated IMT measurement obtained with CALEX was validated on a low contrast ultrasound database of 885 images acquired on Indian patients [2].
3. The automated carotid IMT measurement was studied for the prediction of the SYNTAX Score in Japanese coronary artery disease patients [3].
4. The association of automated carotid IMT measurement and HbA1c in Japanese patients with coronary artery disease was studied [4].

More details of these studies are found in Sect. 2.3.3.

2.3 Results

2.3.1 Carotid Artery Recognition Systems Results

The dataset that was tested incorporated normal and pathological carotids. Also, it contained arteries with different morphology: The first row of Fig. 2.6 is relative to a straight and horizontal artery, the second row to a curved artery, and the third row to a straight and inclined artery in the image frame. The white dashed lines correspond to the ground-truth LI while black corresponds to the ground-truth MA.

The first column reports CAMES tracings, the second column reports CALEX, and the third column CULEX. It is possible to observe how, despite the different carotid morphology, the three techniques show correct results and identify the far adventitial border. However, the variability in the carotid appearance increased the standard deviations of the HD values. This is because the AD_F tracings of straight arteries were closer to the GT-LI/MA profiles than those of curved arteries (see Fig. 2.6a compared to Fig. 2.6d).

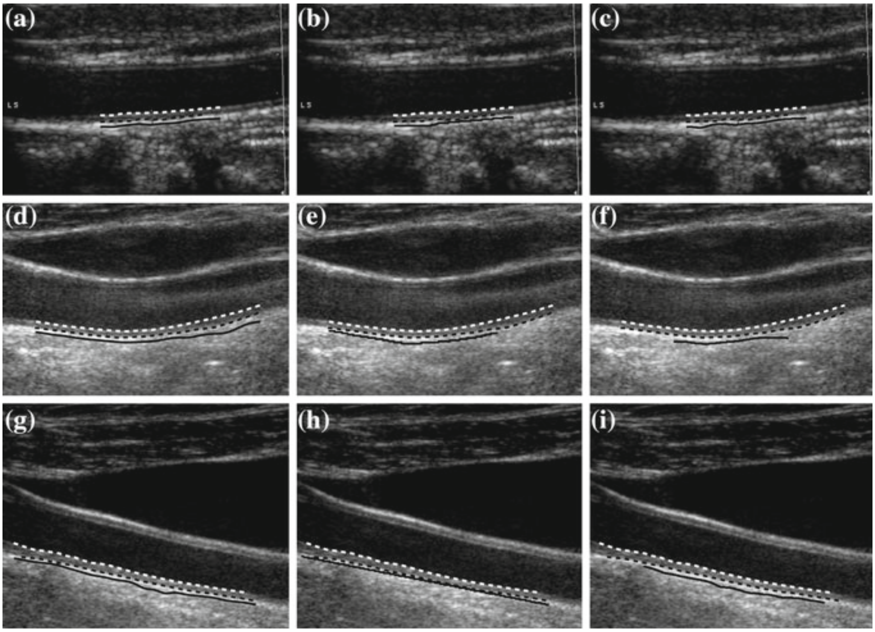

Fig. 2.6 Samples of automated far adventitia tracing by the three techniques. CAMES is represented by panels **a**, **d**, and **g**. CALEX is shown in panels **b**, **e**, and **h**. CULEX is represented in panels **c**, **f**, and **i**. The *white dashed line* represents the GTLI profile, the *black dashed line* the GTMA. The *continuous black line* represents the AD_F. The first row is relative to a straight and horizontal artery; the second row to a curved artery; the third row to a straight but inclined artery

Table 2.1 Hausdorff distance between the average ground-truth (GT-LI/MA) boundaries and the $\mathrm{AD_F}$ automated tracings by the three considered techniques

	$H^{AD_F}_{GT-LI}$ (mm)	$H^{AD_F}_{GT-MA}$ (mm)
CAMES	2.327 ± 1.394	1.632 ± 1.584
CALEX	2.733 ± 2.895	2.036 ± 3.024
CULEX	2.651 ± 1.436	1.965 ± 1.733

A $\Delta_{lim_{pixels}}$ value equal to 60 was considered, so the maximum height of a guidance zone that can be supported to efficiently compute accurate LI and MA borders was found to be equal to 3.6 mm ($\Delta_{lim_{mm}}$).

Overall, CAMES showed an identification accuracy equal to 95%, CALEX showed an identification accuracy equal to 87.3%, while the identification accuracy of CULEX was found to be equal to 90.9%.

Table 2.1 reports the average results (in mm) of the HD between $\mathrm{AD_F}$ and the GT-LI/MA profiles for the three considered techniques. CAMES (scale-space approach) showed $\mathrm{AD_F}$ tracings that were closer to the manually traced LI/MA profiles than those of CALEX (integrated approach) and CULEX (signal processing approach).

2.3.2 GIMT Results

Figure 2.7 portrays the performance of the new GIMT algorithm on three different images, along with RANSAC results. The first row represents the cropped B-mode images with the GIMT LI and GTLI borders in white, whereas the GIMT MA and GTMA borders are overlaid in black. The continuous solid white lines represent the computed tracings while the dotted white lines represent the ground truth tracings. The second row presents segmentation results of RANSAC on the same images. The first image (shown on the first column) portrays an inclined vessel where backscattering in the lumen is present; the second image (Fig. 2.7b, e) shows a large plaque present along a slightly inclined vessel; the last column (Fig. 2.7c, f) instead portrays a large calcified plaque that creates artifacts in the US image. As these results demonstrate, the GIMT algorithm was capable of automatically tracing the LI and MA borders in all of these potentially problematic cases.

GIMT correctly processed 726 out of 735 images (success rate 98.8 %), whereas RANSAC correctly processed 730 images (success rate 99.3 %). The average PDM between the LI and MA borders for all processed images was 0.999 ± 0.372 mm for Ground Truth (GT), 1.042 ± 0.593 mm for GIMT, and 0.914 ± 0.509 mm for RANSAC. The mean bias when compared to GT was −0.044 ± 0.595 mm and 0.087 ± 0.476 mm for GIMT and RANSAC, respectively, showing a Figure of Merit equal to 95.7 % for GIMT and 91.4 % for RANSAC. The average IMTV values were 0.251 ± 0.233 mm for GT, 0.330 ± 0.296 mm for GIMT, and 0.332 ± 0.578 mm for

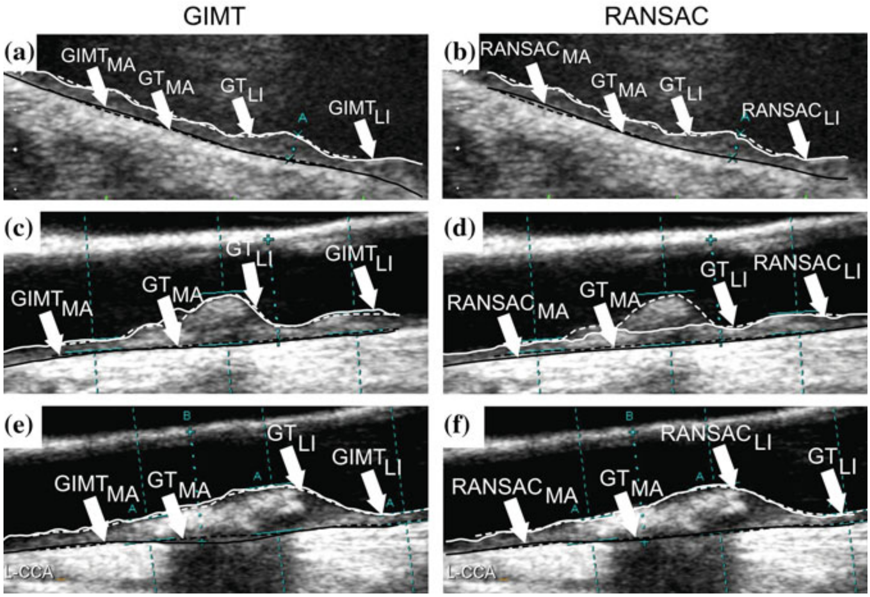

Fig. 2.7 Samples of GIMT (*left*) and RANSAC (*right*) segmentation. The computer traced LI profile is in *white*, the MA profile in *black*. The ground truth tracings are shown by *dashed lines*

Table 2.2 Comparative performance evaluation of fully-automated GIMT and semi-automated RANSAC

Method	Computer-based IMT (mm)	GT IMT (mm)	IMT bias (mm)	FoM (%)
GIMT	1.042 ± 0.593	0.999 ± 0.372	−0.044 ± 0.595	95.7
RANSAC	0.914 ± 0.509	0.999 ± 0.372	0.087 ± 0.476	91.4

RANSAC; the mean bias IMTV values were -0.080 ± 0.287 mm and -0.082 ± 0.566 mm for GIMT and RANSAC, respectively. Table 2.2 summarizes the IMT measurements, bias, and Figure of Merit.

Figure 2.8 represents along the first row the histogram of the IMT measurement bias for GIMT and RANSAC (first column and second column, respectively), and along the second row the Bland-Altman plots. The mean area of the plaque was calculated by cutting the ground truth and algorithm profiles to the same support so as to consider the same portion of the plaque. When considering GIMT, the mean area was 16.925 ± 13.011 mm^2 for GT and 17.205 ± 13.109 mm^2 for GIMT. For RANSAC, the mean area was 18.341 ± 13.358 mm^2 for GT and 16.486 ± 12.935 mm^2 for RANSAC. The GT mean area present different values because GIMT and RANSAC did not always compute the LI and MA profiles along the same portion of the image. Table 2.3 summarizes all of the plaque data obtained for GIMT and RANSAC.

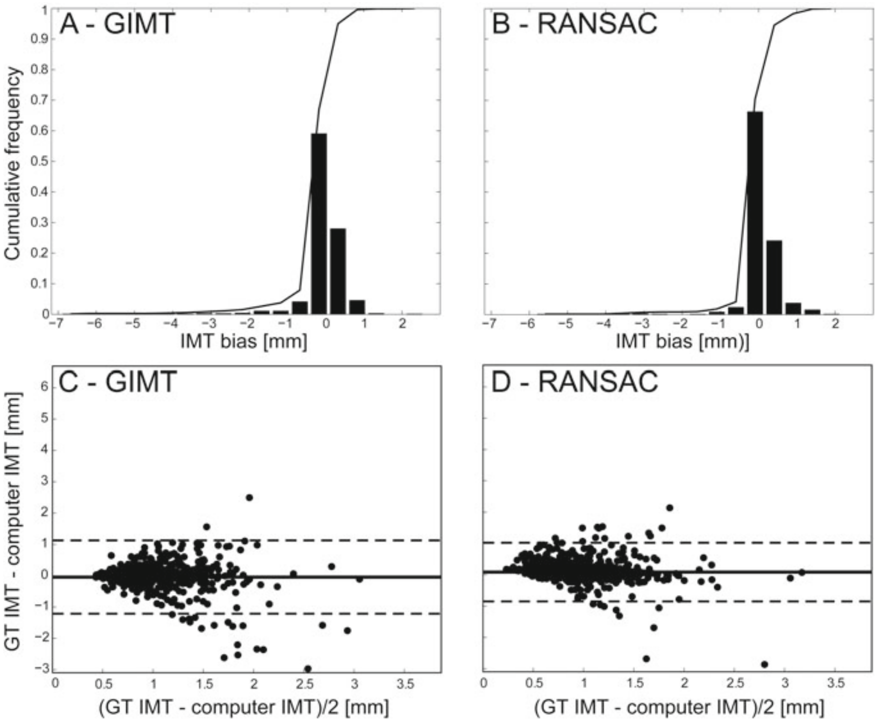

Fig. 2.8 Histogram of IMT measurement bias and Bland-Altman plots compared to the Reader for GIMT (**a** and **c**, respectively) and for RANSAC (**b** and **d**), respectively. In **a** and **b**, the horizontal axis represents the error classes in millimetres and the vertical axis represents the cumulative frequency. The *black lines* represent the cumulative functions of the error distributions

Table 2.3 Plaque data obtained for GIMT and RANSAC compared to ground truth

Method	Area percentage difference (%)	Dice coefficient	Precision	Recall	F-measure
GIMT	28.8 ± 93.8	0.764 ± 0.254	0.772 ± 0.262	0.778 ± 0.256	0.798 ± 0.201
RANSAC	21.8 ± 50.8	0.776 ± 0.226	0.751 ± 0.244	0.840 ± 0.190	0.780 ± 0.219

A total of 218 subjects were included, all with evidence of coronary artery disease and the SYNTAX score (SXscore) was 20.142 ± 16.903, whereas the Plaque Score (PS) was 9.583 ± 5.803. The mean maximum Ground Truth IMT and IMTV was 1.239 ± 0.439 mm and 0.417 ± 0.289 mm, respectively, and 1.417 ± 0.804 mm and 0.553 ± 0.398 mm respectively for GIMT and 1.245 ± 0.657 mm and 0.579 ± 0.988 mm for RANSAC. A direct correlation was found between the max GIMT IMT and IMTV values and the Plaque Score ($\rho = 0.2449$, $p = 0.0003$; $\rho = 0.1987$, $p = 0.0034$, respectively; a direct correlation was also found between the max

Table 2.4 Classification performance for the 5 techniques. N indicates the number of images correctly processed, PPV indicates the positive predictive value, NPV the negative predictive value, and DA the diagnostic accuracy

Technique	N	IMT error (mm)	Sensitivity	Specificity	PPV	NPV	DA
CALEX (auto)	665	−0.050 ± 0.285	0.387	0.850	0.341	0.874	0.773
CARES (auto)	647	−0.032 ± 0.279	0.298	0.895	0.352	0.869	0.799
CAMES (auto)	657	−0.045 ± 0.270	0.475	0.916	0.505	0.906	0.849
CAUDLES (auto)	630	−0.111 ± 0.318	0.462	0.832	0.358	0.884	0.770
FOAM (semi)	665	−0.025 ± 0.225	0.423	0.917	0.505	0.888	0.835

RANSAC IMT and IMTV values and the Plaque Score, although less when compared to GIMT ($\rho = 0.2206$, $p = 0.0011$; $\rho = 0.1802$, $p = 0.0079$, respectively. There was no significant correlation found between the max IMT or IMTV values and HbA1c levels either for GIMT or RANSAC (GIMT IMT and IMTV, respectively: $\rho = -0.0114$, $p = 0.8695$; $\rho = -0.0379$, $p = 0.5849$; RANSAC IMT and IMTV, respectively: $\rho = 0.0168, p = 0.8087$; $\rho = 0.0669, p = 0.3348$).

2.3.3 Validation and Association Results

Comparison Between Four Fully Automated and One Semi-automated IMT Measurement Techniques

The four fully automated lumen-intima and media-adventitia border estimation techniques use different methods that are: (a) edge-based; (b) training-based; (c) feature-based; or (d) directional Edge-Flow based. The database (DB) consisted of 665 images that represented a multi-ethnic group and was acquired using four OEM scanners. Table 2.4 shows the overall results obtained.

Between all of the automatic methods, CARES showed the best performance with the highest accuracy and close to the highest repeatability, as can be seen by the IMT error value in Table 2.4. CAMES was the automatic technique that showed the highest repeatability with a standard deviation equal to 0.270 mm, but presented a lower accuracy, showing a mean IMT bias value equal to 0.045 mm. The user-driven method, FOAM, was the technique that showed the overall best performance both in terms of accuracy and repeatability. In fact, the IMT bias was equal to 0.025 ± 0.225 mm. The reason for this result, which is not surprising, was that the user exploited their expertise and chose the optimal ROI for IMT measurement, by avoiding image regions with high local noise or artifacts. CAUDLES showed a rather low accuracy, with an IMT bias at least twice as large as the other techniques. On this dataset, CAUDLES performance decreased due to the high level of noise affecting many images.

A more in-depth description of the comparison and results obtained with these five algorithms can be found in [1].

Validation on a Low Contrast Ultrasound Database of 885 Images Acquired on Indian Patients

The aim of this study was to demonstrate the usage of automated computer-based IMT measurement system called CALEX on a low contrast and low resolution image database acquired during an epidemiological study from India. Further, to demonstrate the accuracy and reproducibility of the system, the results were compared with the manual tracings of a vascular surgeon – considered as a gold standard.

The IMT value of 885 common carotid arteries in longitudinal B-Mode images was automatically measured. CALEX consisted of a stage for the automatic recognition of the carotid artery (see Sect. 2.2.1) and an IMT measurement modulus made of a fuzzy K-means classifier. Performance was assessed by measuring the system accuracy and reproducibility against manual tracings by experts.

CALEX processed all the 885 images of the dataset (100 % success). The average automated obtained IMT measurement by CALEX was 0.407 ± 0.083 mm compared with 0.429 ± 0.052 mm for the manual tracings, which led to an IMT bias of 0.022 ± 0.081mm. The IMT measurement accuracy (0.022 mm) was comparable to that obtained on high-resolution images and the reproducibility (0.081 mm) is suitable to clinical application. The Figure-of-Merit defined as the percent agreement between the computer-estimated IMT and manually measured IMT for CALEX was 94.7 %.

CALEX had a 100 % success in processing low contrast/low-resolution images. It is the first technique which has led to high accuracy and reproducibility on low-resolution images acquired during an epidemiological study. This algorithm can be proposed as a generalized framework for IMT measurement on large datasets.

The in-depth study can be found in [2].

Prediction of the SYNTAX Score in Coronary Artery Disease Patients

The SYNTAX score (SXscore) is an angiographic score that reflects coronary lesion complexity and it is used to predict clinical outcomes in patients with single or multivessel disease. The purpose of this study was to evaluate whether the carotid intima media thickness (IMT) measured by using an automated software, called could predict the SYNTAX score for coronary artery disease patients.

370 consecutive patients were tested (males 218, females 152; median age 69 ± 11 years) who underwent carotid ultrasound and coronary angiography. The SXscore of the 370 patients was independently assessed by two experienced cardiologists, who calculated the SXscore by considering each coronary lesion producing $\geq$50 % diameter stenosis in vessels $\geq$1.5 mm according to the algorithm available on the SYNTAX website. The IMT values were measured by the automated system, which is based on a multi-resolution approach.

There were 150 subjects (prevalence of 40.5 %) with evidence of coronary artery disease and the SXscore was 8.1 ± 14.4, whereas the mean IMT (obtained by averaging the left and right side) was 0.86 ± 0.23 mm. The Pearson correlation analysis showed a statistically significant correlation between the IMT and SXscore (r value = 0.323; p value = 0.0001). Using the ROC analysis for presence/absence of coronary artery diseases versus IMT, it was observed that the presence of IMT of 1 mm is associated with the presence Coronary Artery Disease with a specificity of 90.52 %.

The results of this study using the fully automated algorithm showed a statistical significant association between IMT and SXscore. This association was demonstrated by applying an automated strategy to an image database of patients with different risk factors. From a clinical point of view, results indicate that automatically measured IMT may be considered a reliable parameter to predict the SXscore.

The in-depth study can be found in [3].

Association of Automated Carotid IMT Measurement and HbA1c

The purpose of this study was to evaluate whether carotid IMT (IMT) identified using automated software is associated with HbA1c in Japanese patients with coronary artery disease.

370 consecutive patients (males 218, females 152; median age 69 ± 11 years) who underwent carotid-US and first coronary angiography were prospectively analyzed. After ultrasonographic examinations were performed, the plaque score (PS) was calculated and automated IMT analysis was obtained with a dedicated algorithm. Pearson correlation analysis was performed to calculate the association between automated IMT, PS and HbA1c.

The mean value of the IMT was 1.00 ± 0.47 mm for the right carotid and 1.04 ± 0.49 mm for the left carotid; the average bilateral value was 1.02 ± 0.43 mm. No significant difference of IMT was detected between men and women. A direct correlation between IMT values and HbA1c ($p = 0.0007$) was found, whereas the plaque score did not correlate with the HbA1c values ($p > 0.05$).

The results of this study confirm that automated IMT values and levels of HbA1c in Japanese patients with coronary artery disease are correlated whereas the plaque score does not show a statistically significant correlation.

The in-depth study can be found in [4].

2.4 Discussion

There are numerous segmentation algorithms present in literature for the segmentation of the intima-media complex for healthy carotids [15, 45–49]. Some of these algorithms are fully automated, while others still require the use of a human operator to locate the carotid artery in the image [21, 31, 32, 46, 50] or the computer generated borders are manually corrected [47–49].

As discussed in Sect. 2.1, the correct localization of the common carotid artery in the B-mode ultrasound image is of utmost importance since it defines the ROI within which the intima-media complex is then segmented. The results portrayed in Sect. 2.3.1 show how CAMES in particular showed very accurate AD_F profiles coupled with a low computational burden and without the need for specific tuning. It can therefore be thought of as a reference technique for carotid localization, to be used in automated intima-media thickness measurement strategies.

Furthermore, there are very few fully automated algorithms present in literature that are capable of segmenting plaques in 2D longitudinal B-Mode ultrasound images. Rocha et. al presented the benchmark technique, RANSAC [31, 32], that is able to segment plaques, but still requires human interaction to complete segmentation. Rocha et. al later in 2012 presented a fully automated technique for plaque segmentation [51], but their technique requires parameter tuning and therefore would present problems when working with multi-institutional and multi-scanner image databases.

The novel technique presented in Sect. 2.2.2 (GIMT) is a novel completely automatic computer-based plaque segmentation technique in longitudinal B-mode ultrasound images. GIMT presented very promising results on a large database containing images coming from patients with evidence of coronary artery disease. It showed good results even when considering possible error sources, such as inclined or curved vessels, lumen backscattering, or large calcified plaques causing acoustic shadowing in the US image. These results can be seen in Fig. 2.7. GIMT showed comparable IMT bias measurements with RANSAC when compared to the Ground Truth measurements and only a slightly larger area percentage difference. RANSAC shows a slightly higher Dice coefficient and Recall, while GIMT shows a higher Precision and F-measure. In fact, as demonstrated also by the IMT bias measurements, GIMT tends to slightly overestimate the measurements, raising therefore the number of false negatives and lowering the Recall value. These differences can be explained by the fact that in RANSAC, the user is required to manually locate the carotid artery in the image by tracing the lumen axis. The user therefore can easily trace the axis, avoiding the near wall and the protrusion of plaque in the lumen. GIMT, however, automatically traces the far adventitia layer and initially approximates the lumen axis and then carries out various checks to try to guarantee a lumen axis that does not protrude into the near wall but that is also found above any possible plaque in the image [6].

The maximum GIMT and RANSAC IMT and IMTV values were also correlated with the Plaque Score and HbA1c levels of the patients. A direct correlation with the Plaque Score was found, whereas the HbA1c levels did not show any correlation either with GIMT or RANSAC. It was found that GIMT correlated slightly better with the Plaque Score compared to RANSAC both when considering the IMT and IMTV values.

Three main contributions of GIMT are that (1) it is completely automated, (2) it is suitable for plaque segmentation, and (3) it can be considered near real time. In fact, GIMT was developed using C++ and processed approximately 14.4 images per minute, showing a mean computation time of 4.16 s. The computer was equipped with an Intel Core i7 processor at 2.66 GHz. RANSAC, on the other hand, was developed in MATLAB and showed a mean computation time of 20.1 s.

Finally, the extent to which the automated IMT measurement can be used was analyzed in numerous studies, (1) through an in-depth comparison between various automated methods and one semi-automated method [1], (2) showing how automated techniques can be used for epidemiological studies even with low contrast and low resolution images [2], (3) confirming that the automated IMT measurement can be considered a reliable parameter to predict the SYNTAX score [3], and finally (4) revealing that automated IMT values and levels of HbA1c in patients with coronary artery disease are correlated [4].

2.5 Conclusions

In conclusion, it is evident how vascular morphological parameters can be automatically extracted from B-mode ultrasound longitudinal images of the common carotid artery thanks to the various techniques that were developed and presented in this chapter.

In particular, Stage I of the automated algorithm CAMES is suitable for carotid localization, and can be used for the assessment of vascular morphological parameters that can be extracted from B-mode ultrasound longitudinal images of the common carotid artery, specifically in automated intima-media thickness measurement strategies.

Moreover, the new GIMT algorithm is suitable for the segmentation of plaques in B-mode longitudinal ultrasound images of the common carotid artery. It boasts the fact of being completely user-independent and does not require any parameter tuning. The performances of the new technique were validated against expert human tracings and benchmarked the results with a semi-automatic algorithm (RANSAC). Clinically speaking, the algorithm automatically traces the boundaries of both the intima and media layers, providing boundaries that can be used further for plaque classification and characterization.

Finally, the automated IMT measurement was validated in numerous situations and was found to be a useful parameter for the prediction and association of clinical parameters of patients with coronary artery disease.

References

1. F. Molinari, K.M. Meiburger, L. Saba, U.R. Acharya, G. Ledda, G. Zeng, S.Y.S. Ho, A.T. Ahuja, S.C. Ho, A. Nicolaides, J.S. Suri, Ultrasound IMT measurement on a multiethnic and multi-institutional database: our review and experience using four fully automated and one semi-automated methods. Comput. Methods Progr. Biomed. **108**, 946–960 (2012)
2. F. Molinari, K.M. Meiburger, G. Zeng, L. Saba, U.R. Acharya, L. Famiglietti, N. Georgiou, A. Nicolaides, R.S. Mamidi, H. Kuper, J.S. Suri, Automated carotid IMT measurement and its validation in low contrast ultrasound database of 885 patient Indian population epidemiological study: results of AtheroEdge™Software. Int. Angiol. **31**(1), 42–53 (2012)

3. N. Ikeda, L. Saba, F. Molinari, M. Piga, K.M. Meiburger, K. Sugi, M. Porcu, L. Bocchiddi, U.R. Acharya, M. Nakamura, M. Nakano, A. Nicolaides, J.S. Suri, Automated carotid intima-media thickness and its link for prediction of SYNTAX score in Japanese coronary artery disease patients. Int. Angiol. J. Int. Union Angiol. **32**(3), 339–348 (2013)
4. L. Saba, N. Ikeda, M. Deidda, T. Araki, F. Molinari, K.M. Meiburger, U.R. Acharya, Y. Nagashima, G. Mercuro, M. Nakano, A. Nicolaides, J.S. Suri, Association of automated carotid IMT measurement and HbA1c in Japanese patients with coronary artery disease. Diabet. Res. Clin. Pract. **100**(3), 348–353 (2013)
5. F. Molinari, K.M. Meiburger, G. Zeng, U.R. Acharya, W. Liboni, A. Nicolaides, J.S. Suri, Carotid artery recognition system: a comparison of three automated paradigms for ultrasound images. Med. Phys. **39**(1), 378–391 (2012)
6. K.M. Meiburger, F. Molinari, R.A. Rocha, G. Zeng, S. Shafique, U.R. Acharya, L. Saba, M. Nagano, A. Campilho, E. Azevedo, A. Nicolaides, J. Suri, GIMT: Generalized IMT measurement in carotid ultrasound images with plaque: an automated method, in (*Under Submission*)
7. I.M. van der Meer, M.L. Bots, A. Hofman, A.I. del Sol, D.A. van der Kuip, J.C. Witteman, Predictive value of noninvasive measures of atherosclerosis for incident myocardial infarction: the rotterdam study. Circulation **109**(9), 1089–1094 (2004)
8. P. Poredos, Intima-media thickness: indicator of cardiovascular risk and measure of the extent of atherosclerosis. Vasc. Med. **9**(1), 46–54 (2004)
9. E. Tremoli, D. Baldassarre, R. Paoletti, R. Rauramaa, K. Nyssonen, U. DeFaire, A. Hamsten, S. Humphries, A. Smit, E. Mannarino, et al. Carotid intima media thickness as marker of atherosclerosis: resultis of the improve study. Atheroscler. Suppl. **9**(1), 213(2008)
10. D. Baldassarre, E. Tremoli, I.S. Group, et al., P775 Determinants of carotid intima media thickness (IMT) in a high risk european population: baseline results of the improve study. Atheroscler. Suppl. **10**(2), e951 (2009)
11. E. Tremoli, D. Baldassarre, 543 Associations between carotid artery intima media thickness, leukocytes and high sensitive c reactive protein in a high risk European population. Atheroscler. Suppl. **10**(2), e74 (2009)
12. M. Amato, D. Baldassarre, E. Tremoli, I.S. Group, et al., 112 Common carotid artery diameter as a marker of cardiovascular risk: preliminary results of the improve study. Atheroscler. Suppl. **10**(2), e232 (2009)
13. M.W. Lorenz, H. Bickel, M.L. Bots, M.M. Breteler, A.L. Catapano, M. Desvarieux, B. Hedblad, B. Iglseder, S.H. Johnsen, M. Juraska et al., Individual progression of carotid intima media thickness as a surrogate for vascular risk (PROG-IMT): rationale and design of a meta-analysis project. Am. Heart J. **159**(5), 730–736 (2010)
14. P. Pignoli, T. Longo, Evaluation of atherosclerosis with B-mode ultrasound imaging. J. Nucl. Med. Allied Sci. **32**(3), 166–173 (1988)
15. F. Molinari, G. Zeng, J.S. Suri, A state of the art review on intima-media thickness (IMT) measurement and wall segmentation techniques for carotid ultrasound. Comput. Methods Progr. Biomed. **100**, 201–221 (2010)
16. F. Molinari, C. Pattichis, G. Zeng, L. Saba, U. Acharya, R. Sanfilippo, A. Nicolaides, J. Suri, Completely automated multi-resolution edge snapper (CAMES): a new technique for an accurate carotid ultrasound IMT measurement: clinical validation and benchmarking on a multi-institutional database. IEEE Trans. Image Process **21**(3), 1211–1222 (2012)
17. F. Molinari, G. Zeng, J.S. Suri, An integrated approach to computer-based automated tracing and its validation for 200 common carotid arterial wall ultrasound images a new technique. J. Ultrasound Med. **29**(3), 399–418 (2010)
18. S. Delsanto, F. Molinari, P. Giustetto, W. Liboni, S. Badalamenti, J.S. Suri, Characterization of a completely user-independent algorithm for carotid artery segmentation in 2-D ultrasound images. IEEE Trans. Instrum. Meas. **56**(4), 1265–1274 (2007)
19. F. Molinari, W. Liboni, P. Giustetto, S. Badalamenti, J.S. Suri, Automatic computerbased tracings (ACT) in longitudinal 2-D ultrasound images using different scanners. J. Mech. Med. Biol. **9**(4), 481–505 (2009)

20. Y. Zhen, S. Jasjit, S. Yajie, R. Janer, Four image interpolation techniques for ultrasound breast phantom data acquired using Fischer's full field digital mammography and ultrasound system (FFDMUS): a comparative approach, in *IEEE International Conference on Image Processing, 2005. ICIP 2005*, vol. 2. pp. 1238–1241
21. F. Destrempes, J. Meunier, M.F. Giroux, G. Soulez, G. Cloutier, Segmentation in ultrasonic B-mode images of healthy carotid arteries using mixtures of Nakagami distributions and stochastic optimization. IEEE Trans. Med. Imaging **28**(2), 215–229 (2009)
22. C.P. Loizou, C.S. Pattichis, M. Pantziaris, T. Tyllis, A. Nicolaides, Snakes based segmentation of the common carotid artery intima media. Med. Biol. Eng. Comput. **45**(1), 35–49 (2007)
23. C.P. Loizou, C.S. Pattichis, C.I. Christodoulou, R.S.H. Istepanian, M. Pantziaris, A. Nicolaides, Comparative evaluation of despeckle filtering in ultrasound imaging of the carotid artery. IEEE Trans. Ultrason. Ferroelectr. Freq. Control **52**(10), 1653–1669 (2005)
24. C.P. Loizou, C.S. Pattichis, M. Pantziaris, T. Tyllis, A. Nicolaides, Quality evaluation of ultrasound imaging in the carotid artery based on normalization and speckle reduction filtering. Med. Biol. Eng. Comput. **44**(5), 414–426 (2006)
25. K.M. Meiburger, F. Molinari, U.R. Acharya, L. Saba, P.S. Rodrigues, W. Liboni, A. Nicolaides, J.S. Suri, Automated carotid artery intima layer regional segmentation. Phys. Med. Biol. **56**(13), 4073–4090 (2011)
26. F. Molinari, U.R. Acharya, G. Zeng, K.M. Meiburger, P.S. Rodrigues, L. Saba, J.S. Suri, CARES 2.0: completely automated robust edge snapper for CIMT measurement in 300 ultrasound images-a two stage paradigm. J. Med. Imaging Health Inf. **1**(2), 150–163 (2011)
27. F. Molinari, U.R. Acharya, G. Zeng, K.M. Meiburger, J.S. Suri, Completely automated robust edge snapper for carotid ultrasound IMT measurement on a multi-institutional database of 300 images. Med. Biol. Eng. Comput. **49**(8), 935–945 (2011)
28. F. Molinari, K.M. Meiburger, G. Zeng, A. Nicolaides, J.S. Suri, CAUDLES-EF: carotid automated ultrasound double line extraction system using edge flow. J. Digit. Imaging **24**(6), 1059–1077 (2011)
29. F. Molinari, K.M. Meiburger, L. Saba, U.R. Acharya, M. Ledda, A. Nicolaides, J.S. Suri, Constrained snake versus conventional snake for carotid ultrasound automated IMT measurements on multi-center data sets. Ultrasonics **52**(7), 949–961 (2012)
30. F. Molinari, K.M. Meiburger, L. Saba, G. Zeng, U.R. Acharya, M. Ledda, A. Nicolaides, J.S. Suri, Fully automated dual-snake formulation for carotid intima-media thickness measurement: a new approach. J. Ultrasound Med. **31**, 1123–1136 (2012)
31. R. Rocha, A. Campilho, J. Silva, E. Azevedo, R. Santos, Segmentation of the carotid intima-media region in B-Mode ultrasound images. Image Vis. Comput. **28**(4), 614–625 (2010)
32. R. Rocha, A. Campilho, J. Silva, E. Azevedo, R. Santos, Segmentation of ultrasound images of the carotid using RANSAC and cubic splines. Comput. Methods Progr. Biomed. **101**(1), 94–106 (2011)
33. G. Zack, W. Rogers, S. Latt, Automatic measurement of sister chromatid exchange frequency. J. Histochem. Cytochem. **25**(7), 741–753 (1977)
34. R. Rocha, *Image Segmentation and Reconstruction of 3D Surfaces from Carotid Ultrasound Images*, Thesis, Faculdade de Engenharia da Universidade do Porto, 2007
35. L. Rudin, S. Osher, Total variation based image restoration with free local constraints, in *IEEE International Conference on Image Processing*, vol. 1. (1994), pp. 31–35
36. L. Rudin, S. Osher, E. Fatemi, Nonlinear total variation based noise removal algorithms, in *Eleventh Annual International Conference of the Center for Nonlinear Studies on Experimental Mathematics: Computational Issues in Nonlinear Science*. Elsevier North-Holland, Inc., (1992), pp. 259–268
37. Y. Yu, S. Acton, Speckle reducing anisotropic diffusion. IEEE Trans. Image Process **11**(11), 1260–1270 (2004)
38. Y. Yu, S. Acton, Edge detection in ultrasound imagery using the instantaneous coefficient of variation. IEEE Trans. Image Process **13**(12), 1640–1655 (2004)
39. J. Canny, A computational approach to edge detection. IEEE Trans. Pattern Anal. Mach. Intell. **8**(6), 679–698 (1986)

40. M. Griffin, E. Kyriacou, C. Pattichis, D. Bond, S. Kakkos, M. Sabetai, G. Geroulakos, N. Georgiou, C. Doré, A. Nicolaides, Juxtaluminal hypoechoic area in ultrasonic images of carotid plaques and hemispheric symptoms. J. Vasc. Surg. **52**(1), 7 (2010)
41. L. Saba, R. Lippo, N. Tallapally, F. Molinari, R. Montisci, G. Mallarini, J. Suri, Evaluation of carotid wall thickness by using computed tomography and semiautomated ultrasonographic software. J. Vasc. Ultrasound **35**(3), 136–142 (2011)
42. K.M. Meiburger, F. Molinari, U.R. Acharya, L. Saba, P. Rodrigues, W. Liboni, A. Nicolaides, J. S. Suri, Automated carotid artery intima layer regional segmentation. Phys. Med. Biol. **56**(13), 4073 (2011)
43. J.S. Suri, R.M. Haralick, F.H. Sheehan, Greedy algorithm for error correction in automatically produced boundaries from low contrast ventriculograms. Pattern Anal. Appl. **3**(1), 39–60 (2000)
44. F. Molinari, G. Zeng, J.S. Suri, Intima-media thickness: setting a standard for completely automated method for ultrasound. IEEE Trans. Ultrasonics Ferroelectr. Freq. Control **57**(5), 1112–1124 (2010)
45. S. Golemati, J. Stoitsis, E.G. Sifakis, T. Balkizas, K.S. Nikita, Using the Hough transform to segment ultrasound images of longitudinal and transverse sections of the carotid artery. Ultrasound Med. Biol. **33**(12), 1918–1932 (2007)
46. D.C. Cheng, A. Schmidt-Trucksass, K.S. Cheng, H. Burkhardt, Using snakes to detect the intimal and adventitial layers of the common carotid artery wall in sonographic images. Comput. Methods Progr. Biomed. **67**(1), 27–37 (2002)
47. M. Gutierrez, P. Pilon, S. Lage, L. Kopel, R. Carvalho, S. Furuie, Automatic measurement of carotid diameter and wall thickness in ultrasound images. Comput. Cardiol. **29**, 359–362 (2002)
48. Q. Liang, I. Wendelhag, J. Wikstrand, T. Gustavsson, A multiscale dynamic programming procedure for boundary detection in ultrasonic artery images. IEEE Trans. Med. Imaging **19**(2), 127–142 (2000)
49. C.P. Loizou, C.S. Pattichis, A.N. Nicolaides, M. Pantziaris, Manual and automated media and intima thickness measurements of the common carotid artery. IEEE Trans. Ultrasonics Ferroelectr. Freq. Control **56**(5), 983–994 (2009)
50. F. Faita, V. Gemignani, E. Bianchini, C. Giannarelli, L. Ghiadoni, M. Demi, Real-time measurement system for evaluation of the carotid intima-media thickness with a robust edge operator. J. Ultrasound Med. **27**(9), 1353–1361 (2008)
51. R. Rocha, S.J, A. Campilho, Automatic segmentation of carotid B-mode images using fuzzy classification, in *Medical and Biological Engineering and Computing*, vol. 50 (2012), pp. 533–545

Chapter 3
Validation of the Carotid Intima-Media Thickness Variability (IMTV)

Abstract This Chapter (The contents of this chapter build upon the paper: K.M. Meiburger, F. Molinari, J. Wong, L. Aguilar, D. Gallo, D.A. Steinman, U. Morbiducci, **"Validation of the carotid intima-media thickness variability (IMTV): Can manual segmentations be trusted as Ground Truth?"**, In: Ultrasound in Medicine and Biology, http://dx.doi.org/10.1016/j.ultrasmedbio.2016.02.004) continues the study on morphological vascular studies for quantitative imaging techniques with clinical B-mode ultrasound images and specifically focuses on the validation of the intima-media thickness variability parameter. Recent studies have shown that the irregularity of the IMT along the carotid artery wall has a stronger correlation with atherosclerosis than the IMT itself, so in this chapter, the Intima-Media Thickness Variability (IMTV), a parameter defined to assess the IMT irregularities along the wall, is studied and validated. In particular, whether or not manual segmentations of the lumen-intima and media-adventitia can be trusted as ground truth in the calculation of the IMTV parameter is analyzed. A total of 60 simulated ultrasound images with a priori IMT and IMTV values were used. The images were simulated using the Fast And Mechanistic Ultrasound Simulation (FAMUS) software and presented 5 different morphologies, 4 nominal IMT values and 3 different levels of variability along the carotid artery wall (no variability, small variability, and large variability). Three experts manually traced the lumen-intima (LI) and media-adventitia (MA) profiles and two automated algorithms were used to obtain the LI and MA profiles. One expert also re-traced the LI and MA profiles to test intra-reader variability. The average IMTV measurements of the ground truth profiles used to simulate the longitudinal B-mode images were equal to 0.002 ± 0.002 mm, 0.149 ± 0.035 mm, and 0.286 ± 0.068 mm for the cases of no variability, small variability, and large variability. The IMTV measurements of one of the automated algorithms showed statistically similar values ($p > 0.05$, Wilcoxon signed rank) when considering small and large variability, but non-significant values when considering no variability ($p < 0.05$, Wilcoxon signed rank). The second automated algorithm showed statistically similar values in the small variability case. Two Readers' manual tracings, however, produced IMTV measurements with a statistically significant difference considering all three variability levels; the third Reader, on the other hand, showed a statistically significant difference in both the no variability and large variability case. Moreover, the error range between the Reader and automatic IMTV values was approximately

K.M. Meiburger, *Quantitative Ultrasound and Photoacoustic Imaging for the Assessment of Vascular Parameters*, PoliTO Springer Series,
DOI 10.1007/978-3-319-48998-8_3

0.15 mm, which is on the same order of small IMTV values, showing how manual and automatic IMTV readings should be not used interchangeably in clinical practice. Thanks to the results found in this study, it can be concluded that expert manual tracings should not be considered reliable in the IMTV measurement and therefore should not be trusted as Ground Truth. On the other hand, the first automated algorithm was found to be more reliable, showing how automated techniques could therefore foster the analysis of the carotid artery intima-media thickness irregularity.

3.1 Introduction

There is wide consensus in considering the intima-media thickness (IMT) of large arteries [1, 2] as an indicator of the onset of vascular disease. In particular, at the common carotid artery (CCA), IMT is considered as an indicator of atherosclerosis [3] and a validated marker of increased cardiovascular risk [4, 5], which was also brought up in Chaps. 1 and 2.

As already mentioned in Chap. 2, various large-scale and multi-center projects on the topic of artery wall thickness have aimed to combine individual data from large IMT prospective studies to investigate whether individual IMT progression can be used as a surrogate for vascular risk [6, 7], and their findings show how the progression of carotid IMT may have predictive capacity.

In recent years, it has been also observed that the variation of the IMT along the carotid artery wall has a stronger correlation with atherosclerosis than the value of the IMT itself [8]. This demonstrates how this parameter could also have a higher capacity of predicting future vascular events. In fact, IMT variability (IMTV) is an estimation of the wall irregularity [8], which is a risk condition since it could be an early indicator of the onset of an atherosclerotic plaque. Therefore, diagnostic tools for the assessment of IMT variations along the vessel length could have a relevant clinical impact, by enriching the information given by an IMT-based analysis only. Several studies confirm the need for IMT variability analysis. In particular, Ishizu et al. [9] associated the irregularity of IMT with the presence of coronary artery disease by ultrasound image analysis and in a more recent study it was observed that both IMT and arterial wall irregularity were associated to an increased cardiovascular risk [10].

Recently, the effectiveness of the carotid IMT alone when used to predict the cardiovascular outcome of subjects [8] was also profoundly questioned. In medical practice, IMT is generally measured by a reader who manually detects and marks the lumen-intima (LI) and media-adventitia (MA) interfaces. The geometrical (i.e. Euclidean) distance between these boundaries is then considered as the IMT. This manual measurement, however, has been reported to be grossly affected by inter-reader variability [11], due partially to image artifacts which can make the detection of LI/MA interfaces difficult. Moreover, the boundaries delineated manually by experts are discrete and noisy, typically made up of only a few points (or samples) along the artery wall [12], which challenges the accurate calculation of variations in IMT regularity. In a follow-up study, Costanzo et al. [8] identified high intra- and inter-reader variability in measuring IMT from CCA ultrasound images as a main cause of the poor predictive value of IMT.

These observations, together with the high inter-observer variability reported in detail by Polak et al. [11], support the development of an arsenal of automated tools that could aid and improve CCA analysis from ultrasound images. A fully automated analysis of carotid wall features (i.e., evaluation of IMT and its variation along an artery segment) saves a substantial amount of time to clinicians and avoids the problem of inter-reader variability [13]. It has also been demonstrated that edge-detected IMT measurements at the CCA far wall have almost the same if not even a stronger association with coronary heart disease events than manually-traced IMT measurements [14].

As far as could be found in present literature, there are still not many comprehensive studies that have clarified the issue of whether or not manual expert tracings can be appropriately used to calculate IMT and, more important, its variability. This chapter reports the study and results which can be found in [15]. The aim is to close this gap by using simulated realistic ultrasound images with a priori IMT and IMTV values, generated by using a recently proposed simulator based upon a point source/receiver approach [16]. On the simulated dataset the carotid IMT variability is measured both automatically and manually. The ultimate goals of the study are (1) to contribute to further investigate the role of the IMTV in the progression of atherosclerosis plaques and (2) to translate its use to the clinical practice.

3.2 Materials and Methods

3.2.1 Evaluation of IMT and IMT Variability (IMTV)

Before confronting the issue of the reliability of manual and automated IMTV measurements, the actual definition of intima-media thickness variability should be introduced. Studies have already been done regarding this issue when considering solely the IMT measurement [17], but not the IMTV measurement, up until the study reported in [15]. The Polyline distance was considered in this study. For conceptual purposes, the lumen-intima (LI) border is considered as boundary A and the media-adventitia (MA) border as boundary B. A Polyline is a line identified by two successive points on boundary B or A. On the basis of this definition, the perpendicular distance from a boundary point A (B) to the Polyline (i.e. the segment connecting two successive points) on the opposite boundary B (A) can be calculated [18]. In this way, the perpendicular distances for all the points from boundary A onto boundary B and vice-versa, is computed. The Polyline distance is defined as the average of the computed distances from A to B and B to A. Figure 3.1 shows an example of Polyline distance computation. This distance metric has been used extensively by researchers in previous studies [19, 20].

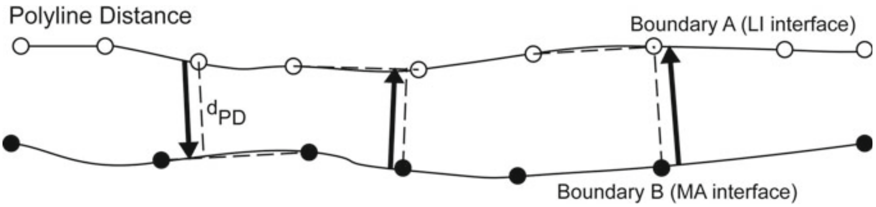

Fig. 3.1 The distance (d_PD) is computed as the perpendicular distance of one point on a boundary with respect to the closest segment of the other boundary. LI = lumen-intima; MA = media-adventitia; PDM = polyline distance metric

As can be seen, the Polyline distance by definition relies on the calculation of several distances between points on one boundary and segments on the other. These distances are fundamental in the calculation of the IMT variability, which can be thought of as the combination of their standard deviations. In fact, if σ_{LI} (σ_{MA}) is defined as the sum of the deviations from the mean distance of the distances from the LI (MA) border to the MA (LI) border, then the IMTV can therefore be calculated as:

$$IMTV = \sqrt{\frac{{\sigma_{\mathrm{LI}}}^2 + \sigma_{\mathrm{MA}}^2}{N_{\mathrm{LI}} + N_{\mathrm{MA}}}} \tag{3.1}$$

where N_{LI} and N_{MA} are the numbers of points on the LI and MA borders, respectively. Roughly speaking, Eq. 3.1 is a measure of the variability of the distance between the LI and MA profiles. This variability is therefore assumed to be representative of the irregularity of the distal wall interfaces.

3.2.2 *Simulation of Ultrasound Test Images*

To validate the reliability of manual segmentations of the LI and MA borders, ultrasound images with LI and MA profiles known a priori were simulated. The images therefore had a priori known IMT and IMTV values. For simplicity, the IMT and IMTV values obtained with these ground truth profiles are called from here on out $\mathrm{IMT}_{\mathrm{GT}}$ and $\mathrm{IMTV}_{\mathrm{GT}}$. The Fast And Mechanistic Ultrasound Simulation (FAMUS) software was used [16] to simulate the ultrasound images. This simulator relies on a point source/receive approach and combines the flexibility and realism of mechanistic approaches with the speed of other approximate approaches. Specific details of the simulator can be found in [16]. The dimensions of the simulated phantoms were 40 × 1 × 25 mm in the x, y and z (lateral, elevation and axial) directions using 20, 000 scatterers (20 scatterers/mm^3) uniformly placed and with a standard Gaussian amplitude distribution. The simulated array transducer had a central frequency of 3.5 MHz with 64 active elements, and the B-mode image was reconstructed using 128 lines. The realistic clinical B-mode ultrasound images were simulated as follows: within the lumen the amplitude of the scatterers was set to zero; within the intima-media complex the Gaussian amplitude distribution was multiplied by a factor of 2; within the adventitia wall layer the Gaussian amplitude was multiplied by a factor of 30. To obtain these values, a subset of 20 real clinical B-mode ultrasound images were used to calculate the contrast between (i) the intima-media complex and the lumen and (ii) the adventitia layer and the lumen. The so obtained mean values were 5.5 and 15.2, respectively. With the aforementioned amplitude values for the simulated images, the obtained mean contrast values were 4.7 for the intima-media complex and 14.2 for the adventitial wall layer.

On the basis of recent observations [21], five images of the CCA with representative geometric attributes (straight, slanted downward, slanted upward, curved downward and curved upward) were simulated. Four different nominal IMT values were simulated (0.5, 0.65, 0.8 and 0.95 mm) for each analyzed CCA geometry, each one with known intima- media thickness irregularity. The simulated IMT variability data belonged to three different levels (i.e., no variability, low variability and large variability), which are paradigmatic of what is observed in clinical practice. In particular, the IMTV values recently reported for the CCA [22] are used. In more detail, the IMTV value was prescribed as follows: Considering no variability in the IMT, the mean $\mathrm{IMTV}_{\mathrm{GT}}$ was nominally zero; considering low variability in the IMT, the mean $\mathrm{IMTV}_{\mathrm{GT}}$ was set to be close to an average value (0.141 mm), as reported in [22]; considering the presence of large variability in the IMT, the mean $\mathrm{IMTV}_{\mathrm{GT}}$ was set to be close to the 90th percentile (0.280 mm) of the IMTV values as reported in [22].

Overall, a total of 60 simulated B-mode images were generated and analyzed. Examples of simulated ultrasound images with different carotid geometric attributes (curved, slanted and straight) and irregularities of the IMT are provided in Fig. 3.2. The simulated images are publicly available for download (see the "Acknowledgments" of this chapter for details).

3.2.3 Manual and Automated Lumen-Intima and Media-Adventitia Tracing

After image randomization, three expert readers (K.M.M, F.M., C.C., coming from both a technical background with 6 [K.M.M.] and 15 [F.M.] years of experience and a medical background [C.C.] with 10 years of experience) manually traced the LI and MA borders on the simulated images. An example of manual tracings, compared with the corresponding $\mathrm{GT}_{\mathrm{LI}}$ and $\mathrm{GT}_{\mathrm{MA}}$ profiles, is provided in Fig. 3.3. Reader 1 also segmented all of the image database at a second time point, to assess intra-reader variability. To manually trace the profiles, the ultrasound image was displayed on the entire computer screen, and the user was asked to insert an arbitrary number of points along the LI and MA interfaces. Once completed, the user was given the option to

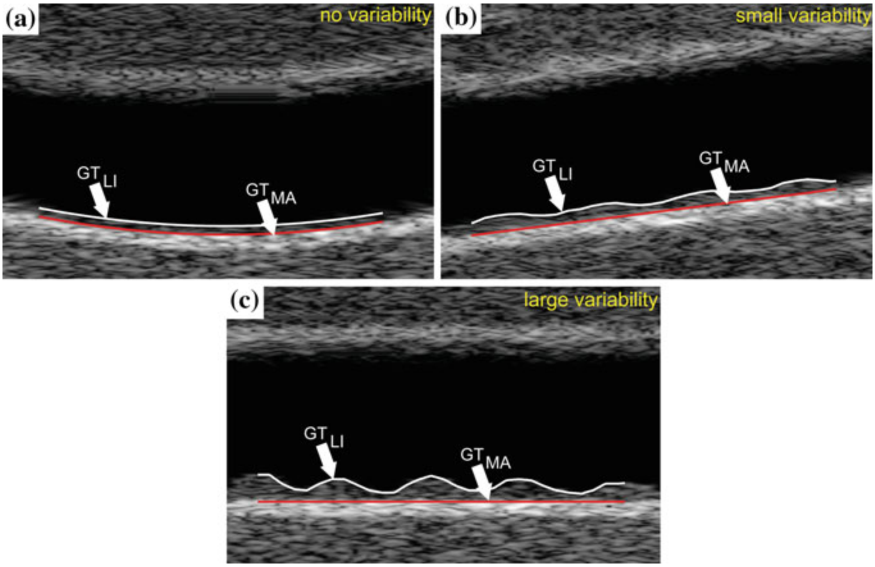

Fig. 3.2 Examples of three simulated ultrasound images with different carotid morphologies (*curved*, *slanted* and *straight*) and irregularities of the intima-media *thickness*. The panels **a**, **b**, and **c** show cases of no variability, small variability, and large variability, respectively. GT_{LI} and GT_{MA} profiles are in *white* and *red*, respectively. GT = ground truth; LI = lumen-intima; MA = media-adventitia

either save the profiles if satisfied with the tracings or to redo the segmentation. The manual segmentations were then interpolated using a linear interpolation so as to have one point for every image column.

Parallelly, two completely user-independent algorithms were used for the automated segmentation of the lumen-intima and media-adventitia borders. The first algorithm is based on a two-step approach: (i) a multiresolution for adventitia border detection (CCA recognition) [23, 24]; (ii) LI/MA border estimation based on dynamic programming and a random sample consensus algorithm [25, 26]. Extensive details on the fully automated IMT measurement can be found in previous studies, where an accuracy equal to approximately 85 % was found to characterize the performance of the algorithm [23–25, 27]. This first algorithm will be referred to as “Auto” from here on out. The second algorithm, referred to as “Auto_{DS}”, is based on the same multiresolution border detection approach for CCA recognition, whereas the LI/MA border estimation is instead based on a dual snake model, which in previous studies yielded a figure of merit equal to approximately 97 % [28].

In Fig. 3.4 are some examples of segmentations obtained by application of the automated algorithms.

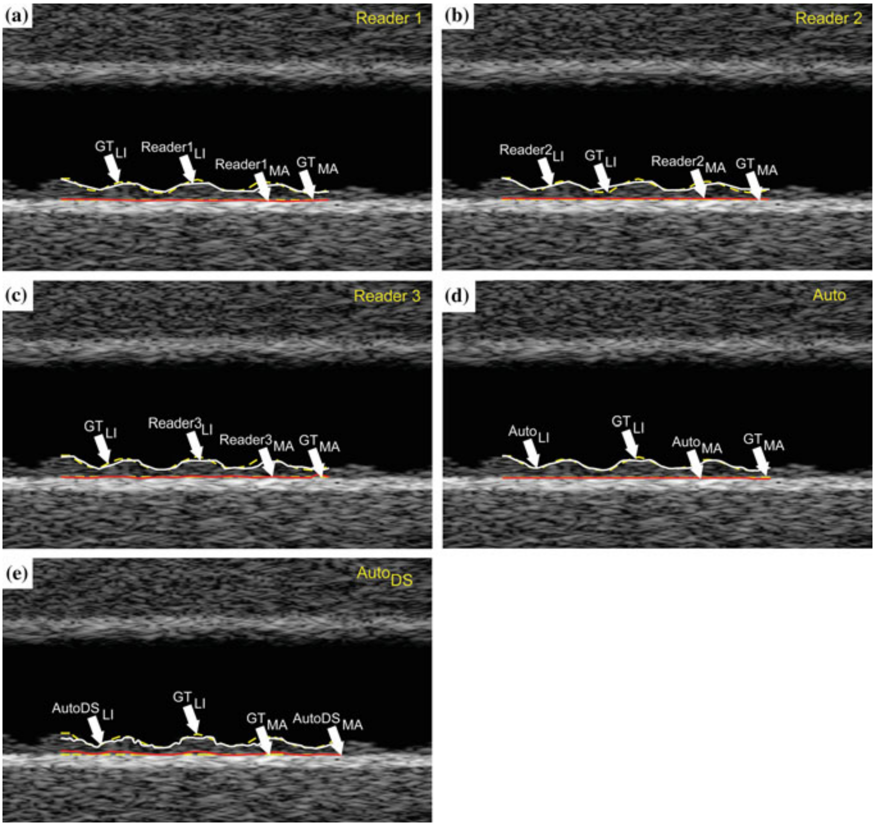

Fig. 3.3 Examples of manual and automated segmentations. The GT_{LI} and GT_{MA} profiles are represented by *dashed yellow lines*. The manual or automatic LI and MA profiles are in *white* and *red*, respectively. Panels **a**, **b**, and **c** show the GT profiles along with the manual segmentations of readers 1, 2, and 3, respectively. Panels **d** and **e** show the GT profiles with the segmentation results of the automatic algorithms, Auto and $Auto_{DS}$, respectively. GT = ground truth; LI = lumen-intima; MA = media-adventitia

3.2.4 Statistical Analysis

The reliability of both the manual and automated procedures for IMTV evaluation was tested with respect to ground truth by calculating the error ($IMTV_{GT}$ - IMTV). Correlation analysis and error analysis (in terms of error distribution and mean square error [MSE]) with respect to $IMTV_{GT}$ values were also performed. Statistically, the Wilcoxon signed rank test was applied to test if the median of the differences from the ground truth was equal to zero. The significance level was set at $p < 0.05$.

The agreement between manual and automated IMTV measurements was evaluated by applying a Bland-Altman analysis, which allowed the assessment of seeing if the two methods are interchangeable when applied to clinical practice.

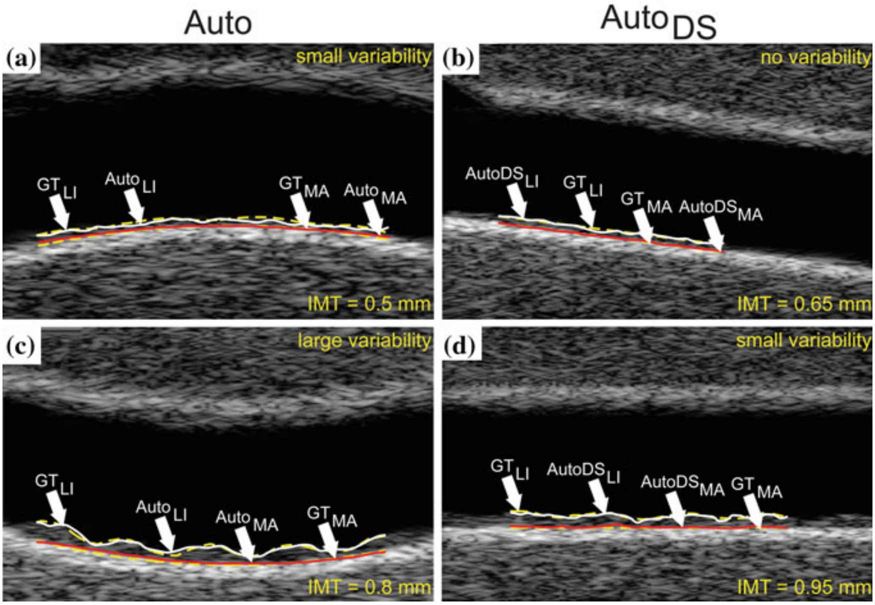

Fig. 3.4 Segmentation examples of the automatic algorithm compared with the true profiles used to simulate the ultrasound images with different nominal IMTs. The GT_{LI} and GT_{MA} profiles are represented by *dashed yellow lines*. The automatic LI and MA profiles are in *white* and *red*, respectively. The nominal IMTs are 0.5 (**a**), 0.65 (**b**), 0.8 (**c**) and 0.95 (**d**) mm. IMT = intima-media thickness; GT = ground truth; LI = lumen-intima; MA = media-adventitia

3.3 Results

Examples of the manual and automated results and their comparison with the ground truth are found in Figs. 3.3 and 3.4. The manual and automatic LI profiles are shown in solid white lines, and the MA profiles in solid red lines. The ground truth (GT) profiles are represented by dashed yellow lines. In particular, Fig. 3.4 displays automated segmentation examples, compared with the GT as prescribed in simulated ultrasound images with different nominal IMTs. The left column (A and C) illustrates segmentation results from the first automatic algorithm (Auto), and the right column (B and D) illustrates results from the second automatic algorithm ($Auto_{DS}$). Note that the automated algorithm produced LI/MA boundaries almost overlapping with the GT boundaries and that, in the presence of high variability (Fig. 3.4b), the variations in the profile of the LI boundary were tracked.

Figure 3.5 presents an example of an image with no IMTV variability. In the zoomed windows (Fig. 3.5b, d), the large white arrows identify sections of the lumen-intima interface that feature visible irregularities in the image because of the simulation effect that both the reader and the automated algorithm captured. However, it can be observed how the LI profile traced by the algorithm was more accurate

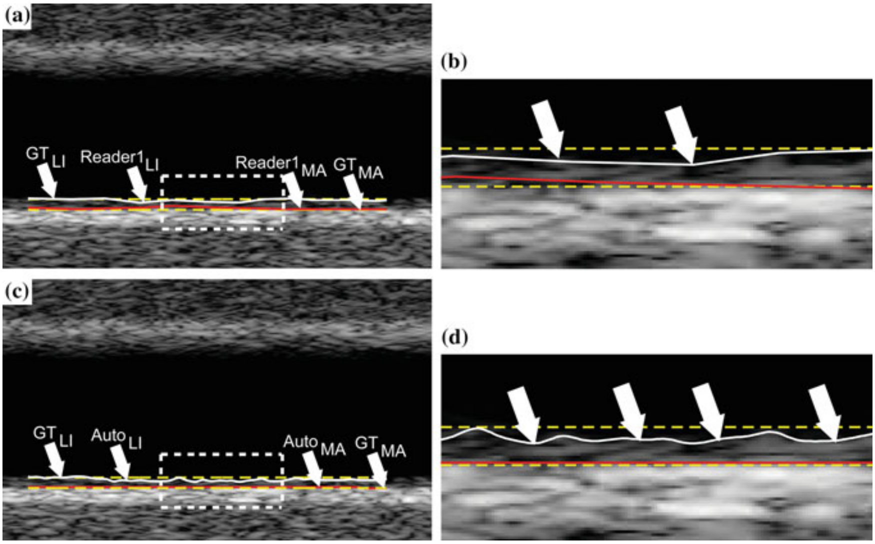

Fig. 3.5 Examples of simulated image with no variability compared with the reader's manual tracings (**a, b**) and the automated algorithm (**c, d**). **a, c** Entire section of carotid artery wall that was segmented. **b, d** Zoomed in sections of artery wall identified by the *white dashed* rectangle in (**a**) and (**c**). The large *white arrows* identify sections of the lumen-intima interface that present visible irregularities in the image caused by the simulation effect. LI = lumen-intima; MA = media-adventitia

in tracing the wall irregularities than the manual profile, and that, overall, the MA profile as computed by the algorithm is closer to the actual GT boundary than the manually traced one. This result obtained on images with no IMTV variability has an impact on IMTV estimation by the automated algorithm and by readers, which is further discussed in the following.

The overall IMT and IMTV values obtained by analyzing the simulated ultrasound image data set are summarized in Tables 3.1 and 3.2, respectively. The values in Tables 3.1 and 3.2 were calculated analyzing the same section of the carotid artery wall (i.e., cutting the profiles so as to always contain the same image column support) and ensuring that each profile has one point per image column (i.e., manual tracings were interpolated). Table 3.1 compares the IMT measurements by the three readers and by the automated algorithms with the GT values. The first row reports the IMT values and IMT measurement error for the set of 60 images, whereas the other rows are relative to the three cases of no, small and large IMTV. This was done to verify that the IMT and IMTV measurements were independent and that the manual and automated tracings were accurate. The overall IMT measurement errors are in line with the performance of previously described automated algorithms [23, 28–30], with a worst case error of 0.120 ± 0.114 mm out of a GT value of 0.901 ± 0.200 mm.

When IMTV measurements (Table 3.2) over the whole data set of images are considered (i.e., not separating images into the three variability levels), it can be

Table 3.1 Manual and automated IMT results with respect to $\mathrm{IMT_{GT}}$ on an image set (total of 60 images)

Variability type	Measure	Ground truth ($\mathrm{IMT_{GT}}$)	Reader 1	Reader 2	Reader 3	Auto	$\mathrm{Auto_{DS}}$
All (60 images)	IMT (mm)	0.815 ± 0.200	0.764 ± 0.192	0.776 ± 0.211	0.780 ± 0.204	0.773 ± 0.234	0.723 ± 0.108
	IMT error (mm)	–	0.052 ± 0.059	0.039 ± 0.072	0.036 ± 0.072	0.042 ± 0.154	0.092 ± 0.110
No variability (20 images)	IMT (mm)	0.720 ± 0.171	0.654 ± 0.128	0.643 ± 0.157	0.662 ± 0.135	0.617 ± 0.094	0.670 ± 0.099
	IMT error (mm)	–	0.066 ± 0.070	0.077 ± 0.064	0.058 ± 0.060	0.103 ± 0.117	0.049 ± 0.097
Small variability (20 images)	IMT (mm)	0.826 ± 0.193	0.748 ± 0.174	0.772 ± 0.167	0.775 ± 0.179	0.707 ± 0.143	0.719 ± 0.095
	IMT error (mm)	–	0.078 ± 0.047	0.054 ± 0.056	0.051 ± 0.050	0.118 ± 0.115	0.107 ± 0.108
Large variability (20 images)	IMT (mm)	0.901 ± 0.200	0.889 ± 0.1924	0.914 ± 0.218	0.914 ± 0.218	0.995 ± 0.242	0.780 ± 0.104
	IMT error (mm)	–	0.012 ± 0.034	−0.013 ± 0.064	−0.001 ± 0.088	−0.094 ± 0.132	0.120 ± 0.114

IMT = intima-media thickness; GT = ground truth

Table 3.2 Manual and automated IMTV results with respect to IMTV$_{GT}$ on image set (total of 60 images). IMTV = intima-media thickness variability; GT = ground truth

Variability type	Measure	Ground truth (IMTV$_{GT}$)	Reader 1	Reader 2	Reader 3	Auto	Auto$_{DS}$
All (60 images)	IMTV (mm)	0.141 ± 0.122	0.129 ± 0.066	0.113 ± 0.063[a]	0.168 ± 0.067	0.180 ± 0.077[a]	0.171 ± 0.056[a]
	(IMTV error (mm)	–	0.013 ± 0.072	0.029 ± 0.076	−0.026 ± 0.077	−0.038 ± 0.064	−0.030 ± 0.077
	Absolute IMTV error (mm)	–	0.063 ± 0.036	0.072 ± 0.037	0.064 ± 0.050	0.056 ± 0.049	0.068 ± 0.047
	IMTV MSE (mm^2)	–	0.005 ± 0.005	0.006 ± 0.006	0.007 ± 0.008	0.006 ± 0.008	0.007 ± 0.007
No variability (20 images)	IMTV (mm)	0.002 ± 0.002	0.077 ± 0.027[a]	0.065 ± 0.020[a]	0.116 ± 0.028[a]	0.120 ± 0.027[a]	0.120 ± 0.023[a]
	IMTV error (mm)	–	−0.075 ± 0.026	−0.064 ± 0.020	−0.114 ± 0.027	−0.119 ± 0.027	−0.118 ± 0.023
	Absolute IMTV error (mm)	–	0.075 ± 0.026	0.064 ± 0.020	0.114 ± 0.027	0.119 ± 0.027	0.118 ± 0.023
	IMTV MSE (mm^2)	–	0.006 ± 0.004	0.004 ± 0.003	0.014 ± 0.007	0.015 ± 0.006	0.014 ± 0.006
Small variability (20 images)	IMTV (mm)	0.144 ± 0.035	0.117 ± 0.031[a]	0.094 ± 0.039[a]	0.154 ± 0.044	0.153 ± 0.039	0.158 ± 0.027
	IMTV error (mm)	–	0.027 ± 0.025	0.050 ± 0.030	−0.010 ± 0.054	−0.009 ± 0.023	−0.014 ± 0.041
	Absolute IMTV error (mm)	–	0.029 ± 0.023	0.052 ± 0.025	0.032 ± 0.044	0.020 ± 0.013	0.038 ± 0.020
	IMTV MSE (mm^2)	–	0.001 ± 0.002	0.003 ± 0.003	0.003 ± 0.007	0.001 ± 0.001	0.002 ± 0.002
No variability (20 images)	IMTV (mm)	0.279 ± 0.066	0.192 ± 0.069[a]	0.179 ± 0.056[a]	0.233 ± 0.061[a]	0.266 ± 0.064	0.235 ± 0.032[a]
	IMTV error (mm)	–	0.086 ± 0.030	0.100 ± 0.043	0.045 ± 0.033	0.013 ± 0.034	0.043 ± 0.048
	Absolute IMTV error (mm)	–	0.086 ± 0.030	0.100 ± 0.043	0.046 ± 0.033	0.030 ± 0.019	0.047 ± 0.044
	IMTV MSE (mm^2)	–	0.008 ± 0.005	0.012 ± 0.008	0.003 ± 0.004	0.001 ± 0.001	0.004 ± 0.006

IMTV = intima-media thickness variability; MSE = mean square error; GT = ground truth. [a]IMTV values that are significantly different ($p < 0.05$, Wilcoxon's signed rank test) compared with IMTV$_{GT}$

observed that the IMTV errors (IMTV_{GT} - IMTV) were found to be 0.013 ± 0.072, 0.029 ± 0.076 and -0.026 ± 0.077 mm for readers 1, 2 and 3, respectively. The automated algorithms (Auto and Auto_{DS}) had IMTV errors of -0.038 ± 0.064 and -0.030 ± 0.077 mm, respectively (Table 3.2). A statistically significant difference was observed for reader 2 and both of the automatic algorithms, whereas there were no statistically significant differences for readers 1 and 3.

A more focused analysis was able to highlight a sensitivity of the results to the level of variability characterizing the IMT. Table 3.2 indicates that when the analysis is performed on the separate subsets of images with no variability, small variability and large variability, the following observations are possible:

1. In the no variability subset, a statistically significant difference was always found between the ground truth and both manual and automated IMTV values, where both the manual and the automated methods always overestimate IMTV.
2. In the small variability subset, no statistically significant difference from the ground truth was observed only for both automated IMTV values and reader 3, whereas the null hypothesis that the difference distribution (IMTV_{GT} - IMTV) has median of zero could be rejected for the manual IMTV measures by readers 1 and 2.
3. In the small variability subset, on average, the automated methods and reader 3 overestimated IMTV (negative error values in Table 3.2), whereas on average readers 1 and 2 underestimated.
4. In the large variability subset, no statistically significant difference from the ground truth was observed only in the first automatic algorithm (Auto), whereas the null hypothesis that the difference distribution (IMTV_{GT} - IMTV) has a median of zero could be rejected for all three readers and Auto_{DS}.
5. Large IMTV values are in general underestimated, independent of the method (positive error values in Table 3.2).
6. In general, the automated methods produce lower absolute IMTV error values relative to the ground truth than the manual method, in the small (0.038 ± 0.020 mm versus 0.052 ± 0.025 mm) and large (0.047 ± 0.044 mm versus 0.100 ± 0.043 mm) variability subsets.
7. The MSE values are lower for the first automated method (Auto) than for the manual method in the large variability subset, whereas they are comparable (and almost negligible) in the small variability subset.
8. The second automated method (Auto_{DS}) is characterized by MSE values slightly higher than those of reader 1, but lower than those of readers 2 and 3, in the small variability subset, whereas in the large variability subset, MSE values from Auto_{DS} are lower than those of readers 1 and 2, but higher than those of reader 3.

The results in Table 3.2 are reinforced by the correlation plots in Fig. 3.6, where it can be observed that considering small and large variability data, there is a more marked linear relationship between the automated IMTV data of the first automated algorithm ($R = 0.94$) and the corresponding IMTV_{GT} values than the manual data ($R = 0.89$, $R = 0.86$, $R = 0.79$). The second automated algorithm exhibits a linear relationship that is intermediate ($R = 0.83$).

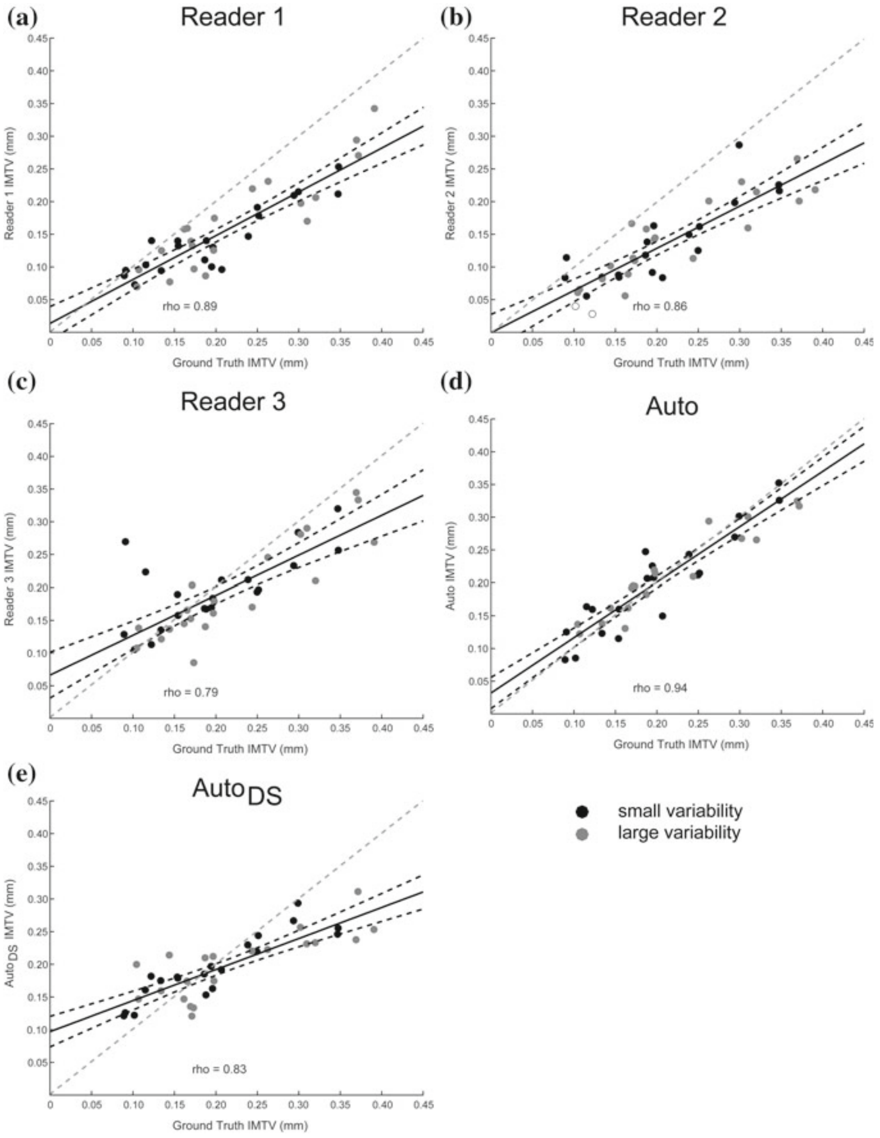

Fig. 3.6 Correlation plots considering small and large variability. The regression *line* is represented by the *solid black line*, and the 95 % confidence interval of the regression *line* is represented by the *dotted black lines*. The *bisector line*, which represents a perfect correlation and no IMTV error, is the *dotted gray line*. Panels **a**, **b**, and **c** show the correlation plots of ground truth compared to readers 1, 2, and 3, respectively. Panels **d** and **e** show the plots when comparing the results obtained by the automated algorithms, Auto and Auto$_{\mathrm{DS}}$, respectively. IMTV = intima-media thickness variability

Table 3.3 IMTV results on 10 images with no variability

Tracings	IMTV (mm)
Ground truth	0.000 ± 0.000
Reader 1	0.093 ± 0.027^{a}
Auto	0.142 ± 0.033^{a}

IMTV = intima-media thickness variability. [a]IMTV values that are significantly different ($p < 0.05$, Wilcoxon's signed rank test) compared with the ground truth IMTV ($IMTV_{GT}$)

Because both the manual and automated methods overestimated the IMTV in the absence of IMT variability (Table 3.2), a more in-depth analysis was carried out. In detail, 10 more ultrasound images of the CCA with a straight morphology and no IMT variability were simulated. Reader 1 manually segmented the images, and the automated algorithm was again employed to generate the LI and MA borders. In Fig. 3.5 an example of a simulated image for this analysis with the manual and automated segmentations can be seen. Even though the ultrasound image was simulated with profiles that are perfectly straight, there is a certain amount of irregularity in the lumen-intima and media-adventitia profiles. This is because the distribution of scatterers (uniform in space, random in amplitude) gives rise to ultrasound speckle patterns that do not necessarily conform precisely to the prescribed vessel geometry. It is important to point out, however, that this mimics the phenomenon of speckle in clinical ultrasound images, similarly caused by the presence of inhomogeneities within tissue. This simulated speckle effect yields the realistic non-perfectly straight profiles that are evident in both the manual segmentation by readers and the automated segmentation. Table 3.3 summarizes the IMTV values obtained in this side study. Notably, the automated algorithm, which segments the carotid artery along every image column, is much more sensitive to this effect than the manual tracings.

Figure 3.7 illustrates the comparison of the automated IMTV measurements with those by the readers. From the Bland-Altman analysis, it can be noted that all readers tended to underestimate the IMTV with respect to the automated algorithm (negative bias). Moreover, (i) no marked proportional error was observed between manually and automatically assessed IMTVs, and (ii) no clear dependence of the difference between the two methods was evident. By comparison with data summarized in Table 3.1, the 95 % limits of agreement in Fig. 3.7 clearly indicate that the limits of agreement are sufficiently large to conclude that manual and automated methods should not be used interchangeably in clinical practice. In fact, the range of agreement of differences between manual and automated IMTV values is approximately 0.150 mm (Fig. 3.7), which could easily lead to situations in which readers classify as null or small IMTV what the an automated technique may classify as small or large, respectively (see $IMTV_{GT}$ values in Table 3.2).

Concerning inter-reader variability, a statistically significant difference was found in seven of nine cases (reader 1 vs. reader 2, reader 1 vs. reader 3, reader 2 vs. reader 3 for no, small and large variability). The only two cases that did not show a statistically significant difference were the no variability subset and large variability subset when

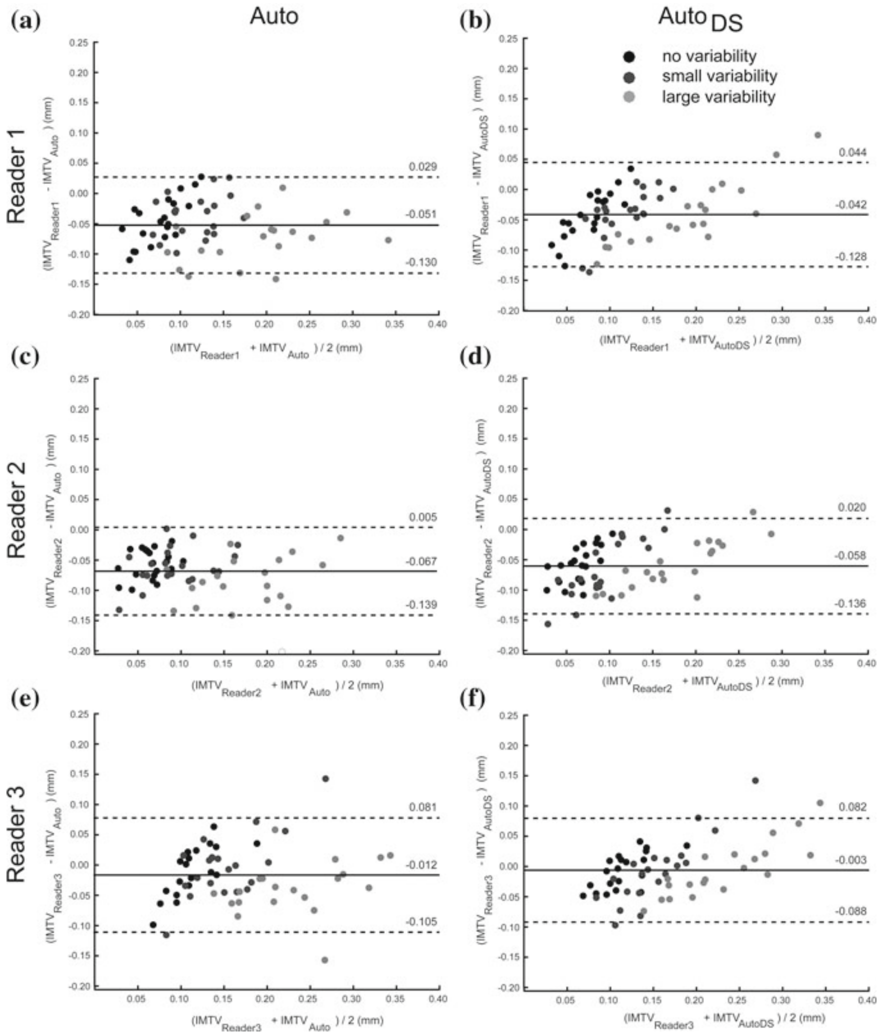

Fig. 3.7 Bland-Altman plots. The bias is represented by the straight *solid black line*; the *straight dotted black lines* represent the bias ± two times the standard deviation (Bland-Altman limits of agreement). In the first (**a, b**), second (**c, d**) and third (**e, f**) rows, measurements of the first, second and third readers, respectively, are compared with the automated (first column, Auto; second column, Auto_{DS}) IMTV measurements. IMTV = intima-media thickness variability

comparing reader 1 with reader 2. Regarding intra-reader variability, a statistically significant difference was observed over all the subsets in IMTV measurements of reader 1 (Table 3.4). These results confirm the critical issue of inter- and intra-reader variability.

Table 3.4 IMTV intra-reader variability

Variability	IMTV (mm)	
	Reader 1	Reader 1b
All	0.129 ± 0.066[a]	0.153 ± 0.075[a]
No	0.077 ± 0.027[a]	0.096 ± 0.018[a]
Small	0.117 ± 0.031[a]	0.135 ± 0.045[a]
Large	0.192 ± 0.069[a]	0.230 ± 0.073[a]

IMTV = intima-media thickness variability. [a]IMTV values that significantly differed ($p < 0.05$, Wilcoxon's signed rank test)

3.4 Discussion

A set of simulated ultrasound images was analyzed with the aim of evaluating the reliability of manual segmentations in the evaluation of IMT variability. Three expert readers manually traced the complete image data set using the same *ad hoc* interface, and one reader segmented the image data set twice so as to analyze intra-reader variability. Two previously developed, fully automated algorithms were also used to trace the LI/MA interfaces. The ultrasound images were simulated considering five different morphologies and three different levels of irregularity of the intima-media thickness along the distal carotid artery wall.

Here the point source/receiver-based FAMUS software [16] was used to simulate B-mode longitudinal images of the CCA. Because of its mechanistic basis, FAMUS-simulated B-mode images can be easily calibrated to clinical scans through contrast calculations, ensuring reliability when subjected to automated segmenting. Additionally, FAMUS has been proven to match the flexibility and realism of other mechanistic approaches based on the impulse response method, but demonstrating a computational savings of nearly two orders of magnitude [16].

A relationship between the IMT measurement errors and the IMTV errors was not observed. Overall, the worst performance of both the readers and the algorithms in the measurement of IMT was found for images with small variability, whereas, as mentioned earlier, the worst for the IMTV estimation was the no variability case.

Determining if expert tracings can be appropriately used to measure IMT variability is an important yet delicate issue. As the results in Table 3.2 indicate, there is a substantial difference when considering different IMT variability levels. In fact, IMTV values from reader 2 and the automated algorithms showed a statistically significant difference in the distributions of median errors from the ground truth when the whole image data set was considered. On the contrary, the distributions of the reader IMTV median errors from the ground truth revealed a statistically significant difference in the three subsets of images simulated with different levels of variability in the IMT, except for reader 3 for the small variability case. This discrepancy can be explained by the fact that, as can be observed in Table 3.2, in the case of no variability the average IMTV error is negative, meaning that the readers' measurements overestimate the IMTV_{GT}. On the other hand, the readers' measurements tend to underestimate the IMTV (i.e., the IMTV error is positive) in both the small and large variability image subsets. This variability level-dependent underestimation/overestimation in readers' analyses leads to an overall average estimation error almost null when the whole image data set is considered, giving the false idea that the manual segmentations present IMTV measurements that are close to the $\mathrm{IMTV}_{\mathrm{GT}}$ values.

On the other hand, the automated IMTV evaluation performance of the first algorithm is characterized by distributions of median errors from the ground truth with no statistically significant difference for both the small and large variability simulated image subsets, confirming its greater robustness with respect to manual evaluation. The second automated algorithm ($\mathrm{Auto}_{\mathrm{DS}}$) showed a statistically significant difference when considering the large variability subset of images; however, the IMTV error values and MSE values were lower than those of both readers 1 and 2 and comparable to those of reader 3, and it still proved to be more robust than some of the manual evaluations. Automated algorithms come in various shapes and sizes, and the findings from this study also illustrate the importance of using an automated algorithm that is also specifically designed for tracking a variable IMT along the artery wall. The second automated algorithm is based on a dual snake model, and although the parameters may be fine-tuned, it had more difficulty in correctly capturing the large variations in the IMT when compared with the algorithm based on dynamic programming and a random sample consensus method.

An important issue is how the reader measurements systematically underestimate both the $\mathrm{IMTV}_{\mathrm{GT}}$ values (Fig. 3.6) and the automated measurements (Fig. 3.7). An underestimation of the irregularity of the IMT along the artery wall may be a critical issue clinically, because it could lead to misclassification of high cardiovascular risk subjects. The results of the Bland-Altman analysis (Fig. 3.7) indicate that the manual and automated methods cannot be used interchangeably in clinical practice. This could have an important implication, in particular when an improperly used manual IMTV measurement could erroneously misclassify a high cardiovascular risk subject as a lower risk subject.

When no variability is present in the IMT, the automated IMTV evaluation shows a statistically significant difference in the distribution of median errors from the ground truth. The results of the analysis carried out only on simulated images of straight CCAs with no variability (Fig. 3.5 and Table 3.3) explain why both the readers and the automated algorithm present IMTV measurements that statistically differ from the IMTV ground truth values when no variability is present in ultrasound images. This architectural effect is minimized in the presence of small and large IMT variability in the simulated images, where $\mathrm{IMTV}_{\mathrm{GT}}$ values are not close to zero. In the two latter cases, the architectural variations of the LI boundary can be properly captured by an automated algorithm, but not by an expert reader.

On the basis of these findings, manual tracings produce IMTV measurements that almost always statistically differ from the $\mathrm{IMTV}_{\mathrm{GT}}$ measurements, whereas the IMT measurements did not statistically significantly differ from the ground truth. The IMTV values as evaluated by readers 1–3 were found to be substantially different. Manual IMTV always showed a statistically significant difference except for when comparing reader 1 and reader 2 evaluations in subsets of no and large variability. Moreover, it was observed that human variability, assessed on reader 1 evaluations, affects manual IMTV measurements. Polak et al. [11] reported that manual IMT reader measurements are affected by inter-reader variability and here it is shown that IMTV evaluation is even more sensitive to this inter-reader variability. It can therefore be concluded that using manual tracings as ground truth for evaluating IMTV is not accurate and highly variable. This proves to be a difficulty when trying to validate the IMTV results of automated algorithms, as it cannot correctly be concluded that the reader IMTV measurements may be identified as ground truth, making direct comparisons impossible. However, automated algorithms were found to provide statistically similar IMTV measurements, even if the actual IMT values show a greater difference from the ground truth values when compared with the manual readings. In fact, the automated IMTV measurements produced the smallest measurement error when compared with the ground truth tracings. This is a positive result for automated algorithms, because it not only indicates their importance in the automated measurement of the intima-media thickness, but also indicates how their usage could be of fundamental importance for the accurate measurement of intima-media thickness variability and its association with clinical data.

Even though the automated algorithm overestimated the IMTV value in cases of no variability (i.e., when IMTV should actually be zero), this can be considered a minor limitation. In reality, an increase in IMTV is caused by the initial stages of the atherosclerotic process, when lipids slowly start to build up in the arterial wall. In such conditions, the IMTV slowly increases, but the IMT would still be low. Hence, an estimated high IMTV associated with a low IMT can be reliably considered as still a low-risk condition.

Moreover, it is important to mention that recent studies have investigated the compression and decompression of the intima-media complex during the cardiac cycle [31]. In particular, it was observed that (i) the IMT undergoes a total variation of roughly 10 % during a heartbeat, and (ii) the temporal variability of the IMT differs substantially between healthy and diseased subjects. For these reasons, it is crucial to perform the IMTV measurements as presented here in the same cardiac phase (e.g., diastole), to maintain consistency among subjects.

To further support the obtained results, the same analysis on simulated images was applied to a small database of 20 in vivo images of the common carotid artery. Based on a local manual measurement of the IMT (the reader manually placed two markers at the thickest section of the wall protruding into the lumen), the images were divided into high risk and low risk. The images were then segmented (i) automatically by applying the first algorithm (Auto) and (ii) manually (by all three readers). The results of the analysis of clinical images, summarized in Table 3.5, indicate that a statistically significant difference between the low-risk and high-risk patients was observed by all

Table 3.5 IMTV results on 20 clinical images

Tracings	IMTV (mm)
Reader 1	0.125 ± 0.086
Reader 2	0.096 ± 0.080[a]
Reader 3	0.135 ± 0.078
Auto	0.123 ± 0.079

[a] IMTV value that significantly differed ($p < 0.05$, Wilcoxon's signed rank test) compared with $\text{IMTV}_{\text{Auto}}$ value

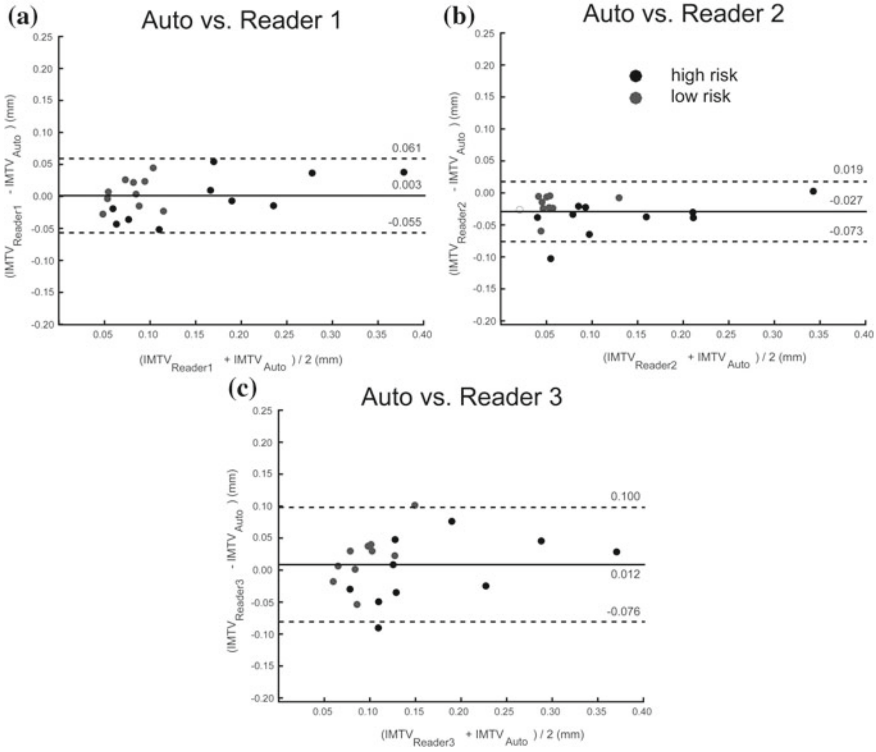

Fig. 3.8 Bland-Altman plots on clinical image database (20 images). The bias is represented by the *straight solid black line*; the *straight dotted black lines* represent the bias ± two times the standard deviation (Bland-Altman limits of agreement). **a**–**c** Measurements of the first, second and third readers, respectively, are compared with the automated IMTV measurements, respectively. IMTV = intima-media thickness variability

of the readers and by the automated algorithm. However, from the receiver operating characteristic analysis, it emerged that the area under the curve was 0.79, 0.85 and 0.84 for readers 1, 2 and 3, respectively, against an area under the curve of 0.94 for the automatic algorithm. This analysis performed on in vivo images confirms that the proposed IMTV automatic evaluation is capable of discriminating between the high- and low-risk patients using clinical images. Concerning inter-reader variability, there were no statistically significant differences in values between readers 1 and 3, whereas reader 2's IMTV evaluations were statistically significantly different in both cases (versus reader 1 and versus reader 2). From the Bland-Altman plots in Fig. 3.8, it can be observed that the range of agreement of differences between manual and automated IMTV extends from approximately 0.092 mm (reader 2) to 0.176 mm (reader 3); reader 2 shows a narrow range of agreement but a mean difference (bias) at least twice as large as those of the other readers. Results in Fig. 3.8 reinforce how inter-reader variability is critical and could easily lead to situations in which one reader classifies as null or small IMTV what another reader may classify as small or large, respectively.

3.5 Conclusions

An in-depth analysis of the evaluation of intima-media thickness variability was performed on realistic simulated ultrasound images of the CCA used as ground truth. The reliability of expert readers' manual tracings in the IMTV calculation was assessed and paralleled by an automated extraction of the IMTV. The IMT and IMTV values were measured by manual LI and MA delineations and by automatic computer-based delineations. From a clinical point of view, it can be concluded that the irregularity of the intima-media thickness along the carotid artery wall is an increasingly important factor to be analyzed; yet manual tracings should not be considered equivalent to ground truth when calculating the IMTV parameter. Contrarily, the profiles generated by an automated algorithm are more consistent and robust, indicating that automated algorithms are an essential tool for clinical analysis of the irregularity of carotid artery wall thickness.

Acknowledgments The 60 images that were simulated for this study are publicly available. The data set can be obtained by sending a request to Prof. Filippo Molinari and by checking his ResearchGate profile.

References

1. P. Touboul et al. Mannheim carotid intima-media thicknessconsensus (2004–2006). An update on behalf of the advisory board of the 3rd and 4th watching the risk symposium, 13th and 15th European stroke conferences, Mannheim, Germany, 2004, and Brussels, Belgium, 2006, in *Cerebrovascular Diseases*, vol. 23. (2007), pp. 75–80
2. P.J. Touboul, M.G. Hennerici, S. Meairs, H. Adams, P. Amarenco, M. Desvarieux, S. Ebrahim, M. Fatar, R. Hernandez Hernandez, S. Kownator, P. Prati, T. Rundek, A. Taylor, N. Bornstein, L. Csiba, E. Vicaut, K.S. Woo, F. Zannad, Mannheim intima-media thickness consensus. Cerebrovasc. Dis. **18**(4), 346–349 (2004)
3. B. von Sarnowski, J. Ludemann, H. Volzke, M. Dorr, C. Kessler, U. Schminke, Common carotid intima-media thickness and framingham risk score predict incident carotid atherosclerotic

plaque formation: longitudinal results from the study of health in Pomerania. Stroke **41**(10), 2375–7 (2010)

4. T. Naqvi, Ultrasound vascular screening for cardiovascular risk assessment. Why, when and how? Minerva. Cardioangiol. **54** 53–67 (2006)
5. O. Elkiran, E. Yilmaz, M. Koc, A. Kamanli, B. Ustundag, N. Ilhan, The association between intima media thickness, central obesity and diastolic blood pressure in obese and owerweight children: a cross-sectional school-based study. Int. J. Cardiol
6. E. Tremoli, D. Baldassarre, R. Paoletti, R. Rauramaa, K. Nyssonen, U. DeFaire, A. Hamsten, S. Humphries, A. Smit, E. Mannarino, et al. Carotid intima media thickness as marker of atherosclerosis: result is of the improve study, in Atheroscler. Suppl. **9**(1), 213 (2008)
7. M.W. Lorenz, H. Bickel, M.L. Bots, M.M. Breteler, A.L. Catapano, M. Desvarieux, B. Hedblad, B. Iglseder, S.H. Johnsen, M. Juraska et al., Individual progression of carotid intima media thickness as a surrogate for vascular risk (PROG-IMT): Rationale and design of a meta-analysis project. Am. Heart J. **159**(5), 730–736 (2010)
8. P. Costanzo, J.G. Cleland, E. Vassallo, P. Perrone-Filardi, Questioning the predictive role of carotid intima-media thickness. Future Cardiol. **7**(5), 651–656
9. T. Ishizu, T. Ishimitsu, H. Kamiya, Y. Seo, N. Moriyama, K. Obara, S. Watanabe, I. Yamaguchi, The correlation of irregularities in carotid arterial intima-media thickness with coronary artery disease. Heart Vessel. **17**(1), 1–6 (2002)
10. N. Labropoulos, J. Leon Jr, L.P. Brewster, L. Pryor, J. Tiongson, S.S. Kang, M.A. Mansour, P. Kalman, Are your arteries older than your age? Eur. J. Vasc. Endovasc. Surg. **30**(6), 588–596 (2005)
11. J. Polak, L. Funk, D. O'Leary, Inter-reader differences in common carotid artery intimamedia thickness: implications for cardiovascular risk assessment and vascular age determination. J. Ultrasound Med. **30**, 915–920 (2011)
12. L. Saba, R. Montisci, F. Molinari, N. Tallapally, G. Zeng, G. Mallarini, J. Suri, Comparison between manual and automated analysis for the quantification of carotid wall by using sonography. A validation study with CT, in Eur. J. Radiol. **81**, 911–918 (2012)
13. J.H. Stein, C.E. Korcarz, M.E. Mays, P.S. Douglas, M. Palta, H. Zhang, T. Lecaire, D. Paine, D. Gustafson, L. Fan, A semiautomated ultrasound border detection program that facilitates clinical measurement of ultrasound carotid intima-media thickness. J. Am. Soc. Echocardiogr. **18**(3), 244–251 (2005)
14. J.F. Polak, D.H. O'Leary, Edge-detected common carotid artery intima-media thickness and incident coronary heart disease in the multi-ethnic study of atherosclerosis. J. Am. Heart Assoc. **4**(6), e001492 (2015)
15. K.M. Meiburger, F. Molinari, J. Wong, L. Aguilar, D. Gallo, D.A. Steinman, U. Morbiducci, Validation of the carotid intima-media thickness variability (IMTV): can manual segmentations be trusted as Ground Truth? **42**(7), 1598–1611 (2016)
16. L. Aguilar, R.S. Cobbold, D. Steinman, Fast and mechanistic ultrasound simulation using a point source/receiver approach. IEEE Trans. Ultrasonics Ferroelectr. Freq. Control **60**(11), 2335–2346 (2013)
17. L. Saba, F. Molinari, K.M. Meiburger, M. Piga, G. Zeng, R.U. Acharya, A. Nicolaides, J. Suri, What is the correct distance measurement metric when measuring carotid ultrasound intima media thickness automatically? Int. Angiol. **31**, 483–489 (2012)
18. J.S. Suri, R.M. Haralick, F.H. Sheehan, Greedy algorithm for error correction in automatically produced boundaries from low contrast ventriculograms. Pattern Anal. Appl. **3**(1), 39–60 (2000)
19. F. Molinari, G. Zeng, J.S. Suri, Intima-media thickness: setting a standard for completely automated method for ultrasound. IEEE Trans. Ultrasonics Ferroelectr. Freq. Control **57**(5), 1112–1124 (2010)
20. F. Molinari, U.R. Acharya, G. Zeng, K.M. Meiburger, J.S. Suri, Completely automated robust edge snapper for carotid ultrasound IMT measurement on a multi-institutional database of 300 images. Med. Biol. Eng. Comput. **49**(8), 935–945 (2011)
21. D. Gallo, D.A. Steinman, U. Morbiducci, An insight into the mechanistic role of the common carotid artery on the hemodynamics at the carotid bifurcation. Ann. Biomed. Eng. **43**(1), 68–81 (2015)

22. N. Ikeda, T. Araki, K. Sugi, M. Nakamura, M. Deidda, F. Molinari, K.M. Meiburger, U.R. Acharya, L. Saba, P.P. Bassareo, M. Di Martino, Y. Nagashima, G. Mercuro, M. Nakano, A. Nicolaides, J.S. Suri, Ankle-brachial index and its link to automated carotid ultrasound measurement of intima-media thickness variability in 500 Japanese coronary artery disease patients. Curr. Atheroscl. Rep. **16**(393) (2014)
23. F. Molinari, C. Pattichis, G. Zeng, L. Saba, U. Acharya, R. Sanfilippo, A. Nicolaides, J. Suri, Completely automated multi-resolution edge snapper (CAMES): a new technique for an accurate carotid ultrasound IMT measurement: clinical validation and benchmarking on a multi-institutional database. IEEE Trans. Image Process (2011). (Sep 23, (Epub ahead of print))
24. F. Molinari, G. Krishnamurthi, R.U. Acharya, S.V. Sree, G. Zeng, L. Saba, A. Nicolaides, J. Suri, Hypothesis validation for far wall brightness in carotid artery ultrasound for feature-based IMT measurement using combination of level set segmentation & registration. IEEE Trans. Instrum. Meas. **61**(9), 1054–1063 (2012)
25. R. Rocha, A. Campilho, J. Silva, E. Azevedo, R. Santos, Segmentation of the carotid intima-media region in B-Mode ultrasound images. Image Vis. Comput. **28**(4), 614–625 (2010)
26. R. Rocha, A. Campilho, J. Silva, E. Azevedo, R. Santos, Segmentation of ultrasound images of the carotid using RANSAC and cubic splines. Comput. Methods Progr. Biomed. **101**(1), 94–106 (2011)
27. R. Rocha, J. Silva, A. Campilho, Automatic segmentation of carotid B-mode images using fuzzy classification, in *Medical and Biological Engineering and Computing*, vol. 50 (2012), pp. 533–545
28. F. Molinari, K.M. Meiburger, L. Saba, U.R. Acharya, G. Ledda, G. Zeng, S.Y.S. Ho, A.T. Ahuja, S.C. Ho, A. Nicolaides, J.S. Suri, Ultrasound IMT measurement on a multiethnic and multi-institutional database: our review and experience using four fully automated and one semi-automated methods. Comput. Methods Progr. Biomed. **108**, 946–960 (2012)
29. S. Delsanto, F. Molinari, P. Giustetto, W. Liboni, S. Badalamenti, J.S. Suri, Characterization of a completely user-independent algorithm for carotid artery segmentation in 2-D ultrasound images. IEEE Trans. Instrum. Meas. **56**(4), 1265–1274 (2007)
30. F. Molinari, C.S. Pattichis, G. Zeng, L. Saba, U.R. Acharya, R. Sanfilippo, A. Nicolaides, J.S. Suri, Completely automated multiresolution edge snapper: a new technique for an accurate carotid ultrasound IMT measurement: clinical validation and benchmarking on a multi-institutional database. IEEE Trans. Image Process. **21**(3), 1211–1222 (2012)
31. G. Zahnd, M. Orkisz, A. Sérusclat, P. Moulin, D. Vray, Simultaneous extraction of carotid artery intima-media interfaces in ultrasound images: assessment of wall thickness temporal variation during the cardiac cycle. Int. J. Comput. Assisted Radiol. Surg. **9**(4), 645–658 (2014)

Chapter 4
Quantitative Assessment of Cancer Vascular Architecture by Skeletonization of 3D CEUS Images: Role of Liposomes and Microbubbles

Abstract This Chapter (The contents of this chapter build upon the paper: F. Molinari, K. M. Meiburger, P. Giustetto, S. Rizzitelli, C. Boffa, M. Castano, and E. Terreno, "**Quantitative Assessment of Cancer Vascular Architecture by Skeletonization of High Resolution 3D Contrast-Enhanced Ultrasound Images: Role of Liposomes and Microbubbles**", In: Technology in Cancer Research and Treatment, 13(6):541–550, 2014) opens the second section of this work, which is based on emphasizing quantitative imaging techniques for the assessment of architectural parameters of vasculature that can be extracted from 3D volumes. Using contrast-enhanced ultrasound (CEUS) imaging, it was demonstrated how the characterization and description of the vascular network of a cancer lesion in mouse models can be effectively determined using both traditional microbubbles and liposomes. Eight mice were administered both microbubbles and liposomes and 3D CEUS volumes were acquired. Vascular architectural descriptors were calculated after a skeletonization technique was applied. The accurate characterization and description of the vascular network of a cancer lesion is of critical importance in clinical practice and cancer research in order to improve diagnostic accuracy or to assess the effectiveness of a treatment. The aim of this study was to show the effectiveness of liposomes as an ultrasound contrast agent to describe the 3D vascular architecture of a tumor. Eight C57BL/6 mice grafted with syngeneic B16-F10 murine melanoma cells were injected with a bolus of 1, 2-Distearoyl-sn-glycero-3-phosphocoline (DSPC)-based non-targeted liposomes and with a bolus of microbubbles. 3D contrast-enhanced images of the tumor lesions were acquired pre-contrast, after the injection of microbubbles, and after the injection of liposomes. The 3D representation of the vascular architecture in these three conditions was obtained with a previously developed reconstruction and characterization image processing technique,. Six descriptive parameters of these networks were also computed: the number of vascular trees (NT), the vascular density (VD), the number of branches, the 2D curvature measure, the number of vascular flexes of the vessels, and the 3D curvature. Results showed that all the vascular descriptors obtained by liposome-based images were statistically equal to those obtained by using microbubbles, except the VD which was found to be lower for liposome images. All the six descriptors computed in pre-contrast conditions had values that were statistically lower than those computed in presence of contrast, both for liposomes and microbubbles. Liposomes

K.M. Meiburger, *Quantitative Ultrasound and Photoacoustic Imaging for the Assessment of Vascular Parameters*, PoliTO Springer Series,
DOI 10.1007/978-3-319-48998-8_4

have already been used in cancer therapy for the selective ultrasound-mediated delivery of drugs. This work demonstrated their effectiveness also as vascular diagnostic contrast agents, therefore proving that liposomes can be used as efficient “theranostic ”(i.e. therapeutic + diagnostic) ultrasound probes.

4.1 Introduction

Sonography is a non-invasive imaging modality that allows the real-time visualization of cancer lesions in almost any organ of the human body, except lungs and the gastric tract (where the presence of air could limit the propagation of the ultrasound waves). Due to their excellent penetration capabilities, sonography has been used to visualize thyroid [1, 2], pancreas [3], liver [4], prostate [5], ovarian [6, 7], breast [8], and brain [9] cancers. Sonographic devices show a gray image in which the pixel intensity (brightness) is proportional to the logarithmic amplitude of the ultrasound echo generated in that portion of tissue when used in traditional B-mode modality. In cancer diagnosis, B-mode imaging allows the detection of the presence of a lesion. A sample image of a mouse syngeneic cancer model (C57BL/6 mouse with subcutaneous grafting of B16-F10 murine syngeneic melanoma cancer cells) is shown in Fig. 4.1a. When used in Doppler modality, sonographic devices also allow the observation of blood flow velocity, since the gray B-Mode image is overlaid by a color map showing either the direction and the value of the blood flow (Color Doppler mode) or just the value of the blood flow (Power Doppler mode). Color and Power Doppler images are, however, limited in resolution and cannot detect blood flows in microvasculature [10] (Fig. 4.1b).

Previous studies have shown that the characterization of cancer lesion vascular patterns are not possible with Doppler imaging alone, because of the lack of spatial resolution [11, 12]. Contrast-enhanced ultrasound (CEUS) imaging can be used to effectively assess the vascularization of tumors in vivo [13, 14]. CEUS imaging relies on second harmonic non-linear imaging (Fig. 4.1c). In this image, the signal is spontaneously generated by the non-linear behavior of both tissues and blood [15]. However, second harmonic imaging mainly exploits the non-linear properties of contrast agents, typically consisting of gas-filled microbubbles. Such microbubbles have an average diameter of about 5 mm and do not extravasate, but they have limited duration in the blood flow [16]. A sample of CEUS imaging is shown in Fig. 4.1d. 3D CEUS imaging allows an accurate reconstruction of cancer vascular patterns [17, 18]. Huang et al. showed that it is possible to reconstruct the spatial vascular pattern of breast cancer lesions by using 3D ultrasound imaging [19, 20]. Their approach consisted of two steps: the Power Doppler images were segmented first of all in order to detect the voxels in which blood flow was present, and then the set of voxels was post-processed by thinning algorithms in order to reconstruct the internal vascular architecture. In 2010, Molinari et al. proposed a quantitative approach for the characterization of thyroid nodules that was based on 3D CEUS imaging [18]. The 3D representation of the tumor vascularization can also be characterized by computing

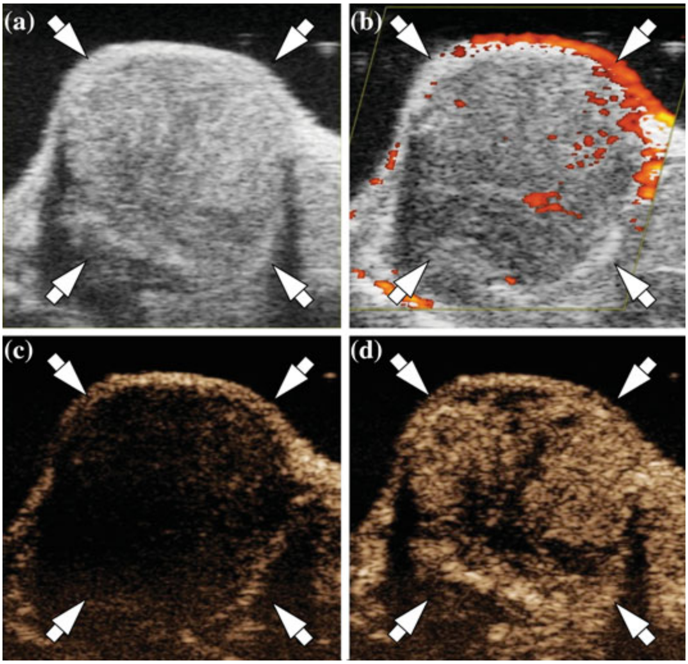

Fig. 4.1 Ultrasound images of a mouse tumor (C57BL/6 mouse with subcutaneous grafting of syngeneic melanoma induced by B16-F10 cancer cells). **a** High-resolution B-mode, **b** Power Doppler, **c** Second harmonic non-linear spontaneous signal, and **d** CEUS image after injection of microbubbles. The *white* arrows indicate the cancer lesion borders. CEUS = Contrast Enhanced UltraSound. Image taken with permission from [22]

numerical features of the vascular pattern, including parameters such as the number of vascular trees (NT), the number of vascular branches, and the tortuosity of the vessels [18]. Acharya et al. then showed that such numerical CEUS features could be used for the differential diagnosis of malignant lesions with respect to benign ones [1, 21].

Liposomes are nano-sized vesicles that are widely used in medicine as drug carriers, mostly in cancer therapy [23, 24]. Researchers have recently been facing the challenge of developing innovative strategies to provide an imaging support to therapies, including the design of probes for the in vivo visualization of drug delivery and release [25, 26]. This field is called “theranosis ”, which comes from merging the words “therapy ”and “diagnosis ”, and it indicates the use of the same agent for diagnosis and therapy [27]. Liposomes play a relevant role in this emerging research field, mainly thanks to the fact that they are very versatile and can therefore be loaded with drugs and diagnostic agents that present different physico-chemical characteristics. Therefore, liposomes present the characteristics of a probe that can potentially be used to both characterize and treat a cancerous lesion.

The aim of this study was to quantitatively compare tumor vascular patterns as assessed by 3D CEUS when using traditional microbubbles and liposomes. The study was conducted on animal models using dedicated ultrasound equipment; however, the processing technique used is general and easily adaptable to human studies.

4.2 Methods

4.2.1 Liposomes Preparation

DSPC[1] liposomes were prepared using the thin film hydration method. The total amount of lipidic material was 50 mg/mL. The liposomes were formulated as follows: DSPC/ DSPE-PEG2000[2] (95/5 molar ratio). Chemicals were purchased from Avanti Polar Inc. (Alabaster, AL, USA). The thin lipid film was hydrated with a 300 mm solution of the clinically approved MRI agent Gadoteridol (marketed by Bracco Imaging as ProHance™) and the so-obtained suspension was extruded several times on polycarbonate filters. The mean hydrodynamic liposomes diameter was 160 ± 10 nm (determined by dynamic light scattering) and the final concentration of Gadoteridol in the liposomes suspension was 30 mm. Another related study showed that liposomes with an internal core of an MRI contrast agent were visible by ultrasound imaging and that their release could be controlled by non-focused ultrasounds, so these liposome were used in the present study [23].

4.2.2 Experimental Protocol

Eight C57BL/6 male mice (10 weeks old, weight 23 ± 4 g) purchased from Charles River Laboratories (Calco, Lecco, Italy) were tested. B16-F10 murine melanoma cells, cultured in RPMI 1640 medium supplemented with 10 % (v/v) heat-inactivated fetal calf serum, 100 UI/mL penicillin, and 100 mg/mL streptomycin, were inoculated 1×10^6 in 0.2 mL PBS subcutaneously to obtain a syngeneic melanoma in the rear thigh of the mice. All the experiments were performed around 1 week after the injection, when the tumor's maximum diameter reached about 8 mm.

The mice were sedated by gaseous anesthesia according to the protocols for preclinical studies [28]. Ultrasound examinations were performed with a VEVO2100 system (Fujifilm VisualSonics, Toronto, Canada) equipped with a 24 MHz linear probe. Traditional high-resolution ultrasound (HRUS) images were acquired, along with 3D CEUS images of the tumor. A basal 3D HRUS and CEUS image without any contrast of the lesion was first acquired. Then a 50 μL bolus of non-targeted Vevo MicroMarker (Bracco, Geneve) optimized for use on the Visualsonics HR Micro-Ultrasound System VEVO2100 was injected. 40 μL of saline solution was then injected right after the contrast agent bolus. Then the 3D HRUS and CEUS images were acquired. After waiting for the complete destruction of the microbubbles (about 30 min), a 200 μL bolus of the above described liposomes was then injected, followed by 40 μL of saline solution. After the liposomes injection, again the 3D HRUS and CEUS images were acquired. The Gain and Time Gain Compensation (TGC) settings of the ultrasound system were kept the same for all exams.

Experiments were performed according to the national regulations and were approved by the local animal experiments ethical committee.

4.2.3 Pre-processing and Skeletonization Strategy

The pre-processing strategy of the images was the same for all three different 3D CEUS volumes. The pre-processing steps are fully described in a previous work [18], and is summarized here in Fig. 4.2. The first column of Fig. 4.2 reports the processing steps applied to the pre-contrast CEUS image (i.e. before the injection of any contrast), the middle column is relative to the CEUS image acquired after the injection of microbubbles, and the far right column is relative to the injection of liposomes. Only the central slice of the 3D volumes is represented. The cancer lesion and the slice are the same in all three columns. The rows of Fig. 4.2 report the sequence of the pre-processing steps. The first row shows the raw CEUS image; the second row portrays the image after intensity normalization; and the third row shows the image after low-pass filtering (Gaussian filtering with a $3 \times 3 \times 3$ kernel and $\sigma = 1$). After filtering, the images were morphologically opened in order to emphasize the intensity signal given by the contrast agent (fourth row of Fig. 4.2). A structuring element of 1 pixel radius was used, because it resembled the shape of a bubble. Each slice was then segmented by using Otsu's thresholding [29]. The bottom row of Fig. 4.2 reports the segmentation mask, where the white region indicates the presence of contrast agent.

Once the slices were processed and segmented, a skeletonization process was applied to reduce the representation of the vascular network. The skeletonization procedure aims at reducing the image into a minimal representation that still preserves morphology [30]. This skeleton-based approach has already been used in previous ultrasound studies [12, 18], in which there was the need to reduce the representation of the blood vessels without losing the architectural features of the vascular pattern. The skeletonization procedure consisted of two cascaded steps:

1. First of all, a geometrical skeleton based on the distance transform (DT) was adopted [31]. The DT of a point belonging to an object is defined as its minimal distance from the closest border of the object itself. Therefore, points located in the middle of a vessel have high DT values, whereas points located near the vessel borders have lower DT values. A DT skeleton can then be obtained by simply imposing a threshold on the DT of an image, thus preserving the innermost points of the objects. The lower the threshold, the thicker the object representation will be. In previous works, it was shown that a suitable value for CEUS DT skeletons is

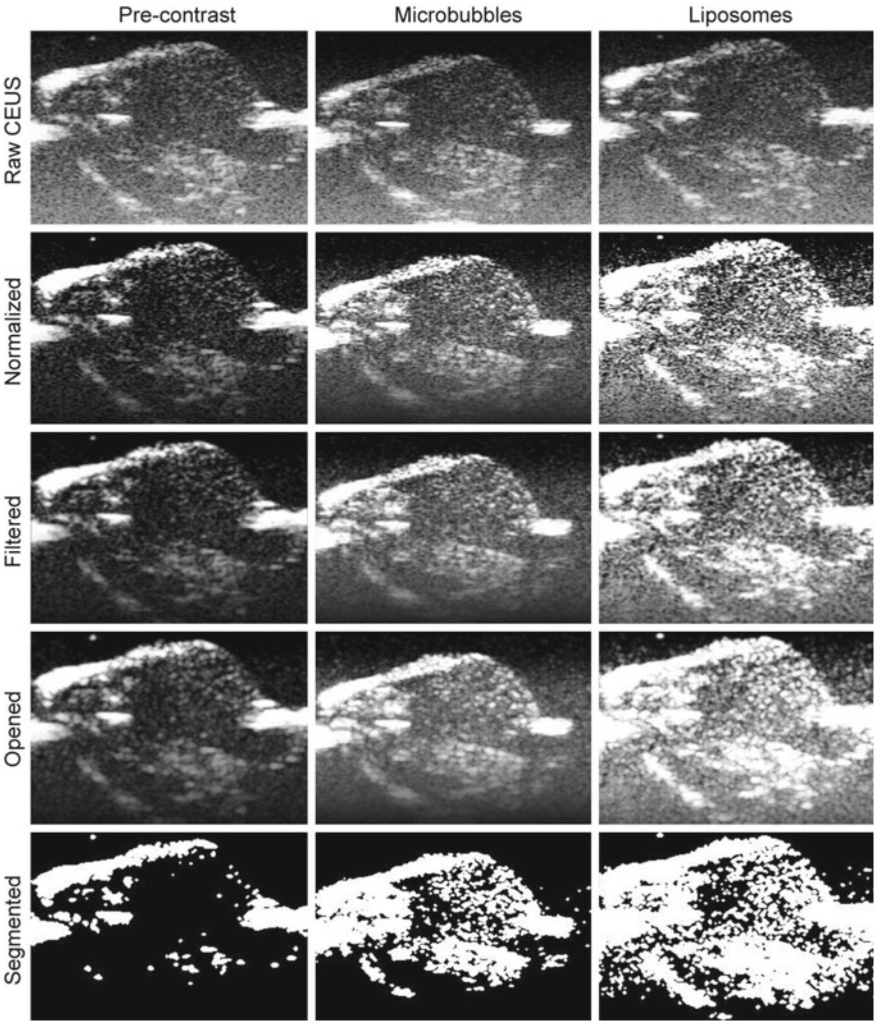

Fig. 4.2 Pre-processing architecture. The first column is relative to a central slice of the tumor before injection of any contrast, the second to the injection of microbubbles, and the third to the injection of liposomes. The rows report the pre-processing steps (from *top* to *bottom*): the raw image, the intensity normalized image, the filtered image, the morphologically opened image, and the result of the segmentation based on Otsu's thresholding. CEUS = Contrast Enhanced UltraSound. Image taken with permission from [22]

0.55 [18]. Figure 4.3 sketches the skeletonization process. In particular, Fig. 4.3b shows the DT skeleton obtained by the segmented CEUS image of Fig. 4.3a.

2. The DT skeleton was then again thinned with the use of a topological skeleton. The skeleton proposed by Ma and Sonka [30] was used. Topological skeletons are based on a series of $3 \times 3 \times 3$ masks. These masks describe all the possi-

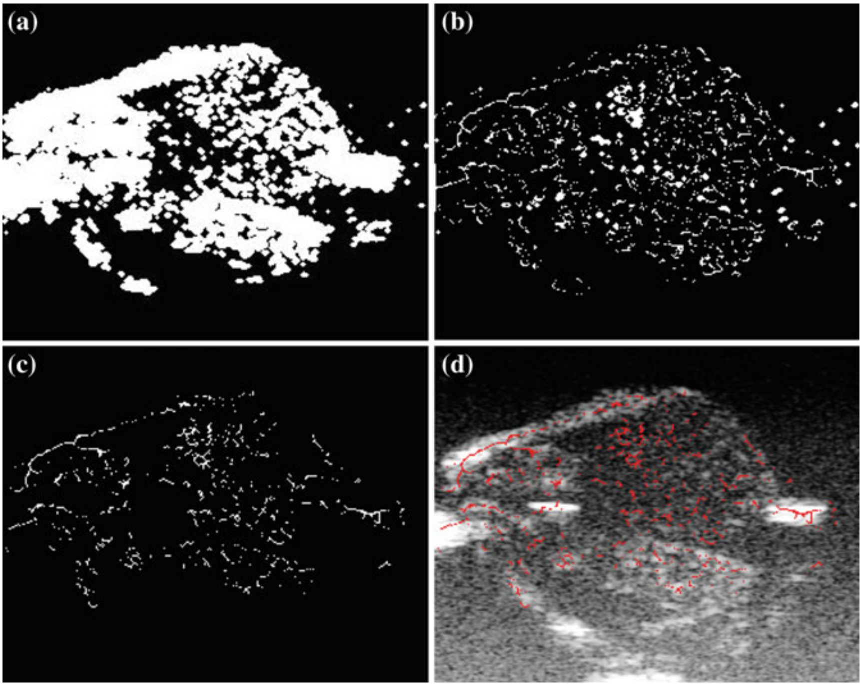

Fig. 4.3 Skeletonization process. This sample is relative to the injection of microbubbles. **a** Preprocessed image (same as Fig. 4.2, *middle* column, *bottom* row), **b** Application of the Distance Transform geometric skeleton, **c** Application of the topological skeleton, and **d** Final skeleton (in *red*) overlaid on the original CEUS image. CEUS = Contrast Enhanced UltraSound. Image taken with permission from [22]

ble conditions to consider a pixel as a "border "pixel. Hence, if the 3 × 3 × 3 neighborhood of a pixel matches one of the masks, that pixel is located on the border of an object and can thus be deleted. Full details about the Ma and Sonka algorithm [30] can also be found in the study by Palágyi and Kuba [32], in which 38 masks were used. Figure 4.3c reports the topological skeleton obtained from the DT skeleton of Fig. 4.3b. Figure 4.3d shows the final skeleton in red overlaid on top of the original CEUS image.

4.2.4 Vascular Pattern Characterization

The obtained 3D skeletons can be thought of as volumetric binary images containing a network of vessels. Therefore, such networks can be analyzed in order to numerically describe the represented vascular pattern. Each 3D skeleton was hence analyzed by the Breadth First Search (BFS) algorithm [33]. Since cancer lesions can have different

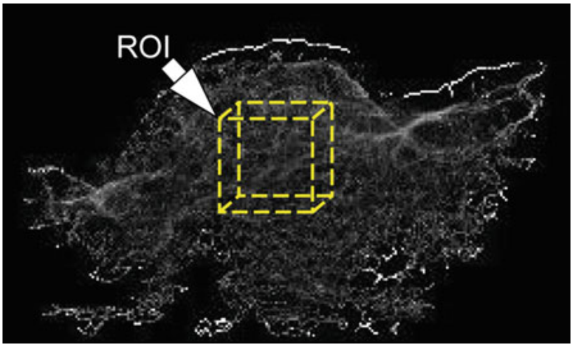

Fig. 4.4 Manual positioning of the Region-of-Interest (ROI) in the *center* of the 3D skeleton. The ROI size was 50 × 50 × 20 pixels. Image taken with permission from [22]

sizes, a Region-of-Interest (ROI) of 50 × 50 × 20 pixels was analyzed, in order to standardize the quantification of the vascular pattern. This size was chosen because it was compatible with the dimensions of all the cancer lesions of the dataset. Figure 4.4 shows the positioning of the ROI with respect to the 3-D skeleton. The positioning of the ROI was done manually.

Starting from an initial voxel, the BFS algorithm navigates the entire skeleton by following the vessels. The BFS marks each voxel as visited and continues until all voxels of the skeleton have been visited at least once. The BFS algorithm is able to search all of the vessels in the skeleton and then compute quantitative parameters. The six parameters that were considered indicative of the vascular pattern were:

1. Number of vascular trees (NT): Defined as the number of trees in which the BFS decomposes the skeleton image.
2. Vascular density (VD): Defined as the number of skeleton voxels compared to the volume of the selected ROI.
3. Number of branching nodes (NB): Defined as the number of branches of the structure.
4. 2D distance metric (DM): A measure of the bi-dimensional tortuosity of a vessel. Considering a curved line representing the vessel, the DM is defined as the ratio between the actual length of the curve and the Euclidean distance between the first and last point of the curve. The DM value of a straight line would be equal to 1, but it would assume higher values as the curvature increases.
5. Inflection count metric (ICM): Defined as the number of flexes of a curve. This is another measurement of vessel tortuosity.
6. 3D sum of angles metric (SOAM): Defined as the sum of all the angles that a curve has in space.

The mathematical description of these parameters can be found in previously published papers [18, 19]. To summarize, the vascular complexity was characterized by three morphological parameters (NT, VD, and NB) and by three curvature/tortuosity parameters (DM, ICM, and SOAM).

4.3 Results

The advantages of the proposed two-step skeletonization architecture are:

1. Prevention of vessel disconnections, because the DT skeleton cannot create disconnections unless a wrong (i.e. too high) threshold is selected;
2. Reduction of the computational cost, because the computationally expensive topological skeleton is applied to an already reduced set of voxels.

Figure 4.5 reports the obtained skeletons from the three sets of CEUS images for a cancer lesion of the dataset. The first column of Fig. 4.5 shows the tumor before injection of any contrast, the second displays the injection of microbubbles, and the third portrays the injection of liposomes. The first row Fig. 4.5 instead portrays the original CEUS images (central slice of the tumor); the second row reports the corresponding skeletonized images; the bottom row instead shows the 3D reconstructed skeletons. It can be observed that the 3D skeletons obtained after injections of microbubbles or liposomes are very rich and represent the intra-lesion vasculature very nicely. Conversely, the skeleton obtained from the raw CEUS images without any contrast is limited to the periphery of the lesion, and there is no representation of the internal vessels.

Table 4.1 reports the average values of the vascular descriptors. The values were measured on the 3D CEUS volumes after skeletonization.

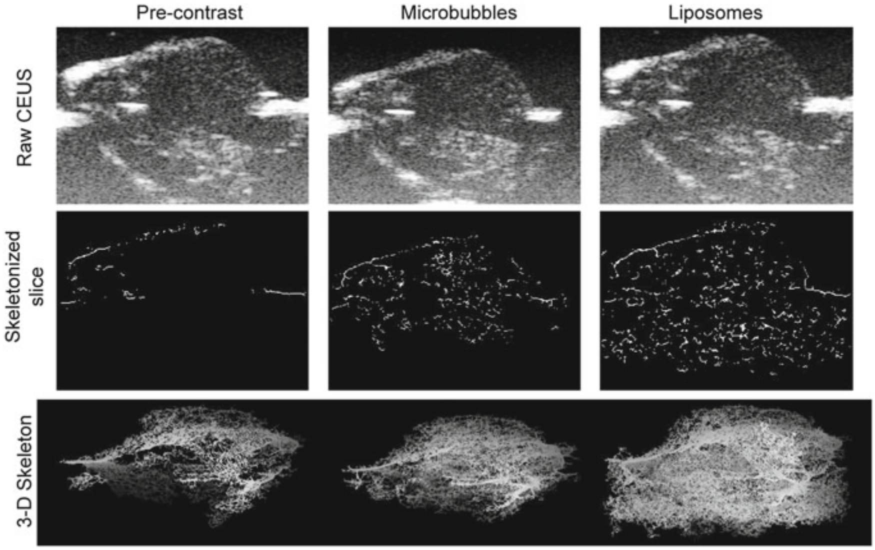

Fig. 4.5 Representation of the final 3D skeletons. The first column is relative to the tumor before injection of any contrast, the second to the injection of microbubbles, and the third of liposomes. The *first row* reports the original CEUS image (central slice of the tumor); the *second row* reports the corresponding skeletonized image; the *bottom* row reports the 3D reconstructed skeleton. CEUS = Contrast Enhanced UltraSound. Image taken with permission from [22]

Table 4.1 Average values of the six descriptors of the vascular patterns as measured from the 3D CEUS skeletons. The asterisk * indicates the descriptors that were not statistically different between microbubbles and liposomes (paired Student's t-test; $p > 0.05$). CEUS = Contrast Enhanced UltraSound

	NT*	VD	NB*	DM*	ICM*	SOAM*
Pre-contrast	14.3 ± 6.2	0.01 ± 0.01	188 ± 146	8.39 ± 4.26	3.76 ± 2.73	4.49 ± 3.08
Microbubbles	39.5 ± 17.5	0.07 ± 0.01	1096 ± 357	23.70 ± 3.57	7.86 ± 3.57	12.17 ± 6.41
Liposomes	38.1 ± 17.2	0.05 ± 0.03	695 ± 450	23.11 ± 12.08	9.88 ± 5.45	11.08 ± 6.00

(NT : Number of vascular Trees; VD : Vascular Density; NB : Number of Branching nodes; DM : 2D Distance Metric; ICM : Inflection Count Metric; SOAM : 3D Sum Of Angles Metric)

The first comparison is between the vascular descriptors obtained by using liposomes and microbubbles (second and third rows). The asterisks in Table 4.1 denote the descriptors that were not statistically different between the 3D microbubbles and 3D liposomes CEUS skeletons (paired Student's t-test; $p > 0.05$). Five out of six descriptors were not statistically different, whereas one (VD) was higher for microbubbles than for liposomes ($p = 0.01$). The average NT detected in the ROIs from 3D CEUS skeletons obtained after the injection of microbubbles was equal to 39.5 ± 17.5 (38.1 ± 17.2 after liposomes injection), whereas the average NB was 1096 ± 357 (695 ± 450 after liposomes injection). The three curvature/tortuosity descriptors were equal to 23.70 ± 3.57 (DM), 7.86 ± 3.57 (ICM), and 12.17 ± 6.41 (SOAM) for microbubbles-based skeletons. For liposomes-based skeletons the three descriptors had the following respective values: 23.11 ± 12.08 (DM), 9.88 ± 5.45 (ICM), and 11.08 ± 6.00 (SOAM). The values reported by both the second and third rows are very close, thus demonstrating the effectiveness of liposomes as a potential alternative to microbubbles for the quantification and characterization of cancer vascularization with 3D ultrasound images.

The second comparison is among the vascular descriptors measured by the pre-contrast skeletons and the respective descriptors measured after microbubbles or liposomes injection. The values of the six descriptors measured in pre-contrast conditions were: 14.3 ± 6.2 (NT), 0.01 ± 0.01 (VD), 188 ± 146 (NB), 8.39 ± 4.26 (DM), 3.76 ± 2.73 (ICM), 4.49 ± 3.08 (SOAM). All the descriptor values were statistically lower in the pre-contrast condition than in the contrast condition (paired Student's t-test; always $p > 0.05$), independently on the type of contrast (i.e. microbubbles or liposomes).

4.4 Discussion

The reconstruction and numerical characterization of a tumor lesion vasculature could be very useful in practical applications, in basic research, and in pharmacological and oncological applications. Previous studies have demonstrated how the characterization of the internal vascularization of breast lesions could be useful in clinical practice to aid the differential diagnosis between benign and malignant lesions. Huang et al. showed that the descriptors of the vascular architecture of a lesion could be used to assess malignancy in breast lesions [19]. They used 3D volumes obtained by Power Doppler imaging; therefore, their data were mainly relative to macro-vessels because of the low resolution. They showed that malignant lesions had higher vascular descriptors values. This is due to the fact that tumor angiogenesis creates new vessels with a high number of branches, and that the neo-formed vessels are usually coiled. More recently, the same team showed that malignant lesions can be efficiently detected by comparing the vascular descriptors of the suspected lesion with the descriptors measured on a portion of healthy tissue taken as reference [20]. Molinari et al. applied a similar technique to show the difference between the intranodal vascularization of benign and malignant thyroid lesions [18], and they demonstrated that the numerical values of the vascular descriptors measured by the skeletons are higher for malignant lesions than for benign lesions. Molinari et al. used CEUS imaging [18], thus showing the effectiveness of this approach to describe the microvascularization of a tumor. Therefore, this combined approach of 3D reconstruction and description of the vascular architecture finds its application in the field of cancer research and treatment.

In this work, conducted on animal models, it was shown that the injection of a bolus of liposomes produces CEUS 3D volumes that are suitable for the reconstruction and characterization of the microvascularization of a lesion. It was demonstrated that the 3D skeletons of the intra-lesion vascular network obtained after liposomes injection are statistically similar to those obtained after injecting traditional sonographic contrast agents consisting of gaseous microbubbles. The skeleton of the vascular network of eight mice by injecting microbubbles and liposomes separately was reconstructed, and then it was shown that the numerical values of the vascular descriptors were on average not statistically different. Specifically, the number of branches, and the curvature and tortuosity indexes were not statistically different when measured after microbubbles or liposomes injection (Table 4.1).

It was found that one out of six parameters (VD) was statistically lower for liposome-based skeletons than for microbubbles skeletons. This result was most likely due to the type of liposomes that were used. The DSPC liposomes used in this work likely generated a non-optimal ultrasound signal. Numerically, the average VD measured from 3D liposome-based CEUS images was not very different from that measured from microbubbles-based images, but the standard deviation was three times higher (Table 4.1). Additionally, the ultrasound equipment used was specifically optimized for the Vevo MicroMarker microbubbles and produced images with higher echogenicity. Hence, it is likely that a suboptimal sonographic response of the liposomes, which produced images with lower echogenicity, gave forth a lower VD average value. An improved echogenicity of the liposomes could be obtained by changing the liposomal formulation in terms of membrane and core composition. Alternatively, echogenic liposomes (ELIP), i.e. liposomes loaded with a mixture of gas and water, could also be tested; however, these liposomes have a more difficult preparation process and often tend to present a large variability in their size [34]. The latter issue may significantly limit the performance of the probe due to the fact that large nanoparticles (diameter >200 nm) reduce the vascular extravasation [35], thereby decreasing considerably their usefulness in cancer therapy. Furthermore, ELIP are not approved for clinical use yet, as opposed to conventional liposomes.

Nevertheless, this study demonstrates that it is possible to accurately reconstruct and describe the vascular architecture of a cancer lesion by using liposomes and 3D non-linear ultrasound imaging. Some very recent studies adopted a CEUS based methodology to improve the assessment of cancer lesions. Specifically, Grouls et al. used non-targeted microbubbles and clinically translatable PEGylated targeted microbubbles for the vascular endothelial growth factor receptor type 2 [36]. They quantified the microbubbles kinetics in the lesion and showed that targeted microbubbles enabled the distinction between early stages of liver dysplasia and a normal liver. In this study, stealth non-targeted liposomes were used. Therefore, this technique is believed to have further potential for improvement if echogenic and targeted liposomes were used.

The technique presented here has some limitations that will be discussed here in the following. From a technical point of view, the procedure is not fully automated yet. The pre-processing and skeletonization steps are automated and user-independent, but manual placing of the analysis ROI (Fig. 4.4) is required. Different placements of the ROI could lead to different vascular parameters. In pilot experiments (not reported in this work), a very low intra-operator variability (lower than 0.1 % for all the six parameters) was observed. The team has already developed a fully automated version of this procedure that will remove this limitation. The new procedure will incorporate an automated segmentation of the tumor in the 3D HRUS images. The segmentation mask will be applied to the 3D CEUS volume, in order to automatically determine the entire lesion volume. Another limitation of this study is given by the kinetics of the liposomes in the tumor environment [37]. Since liposomes might extravasate, their non-linear signal could become inaccurate in certain conditions. In fact, smaller nanoparticles have a higher therapeutic effect, but they generate a lower ultrasound signal. Liposomes with an average size of 200 nm might be the best compromise. The liposomes kinetics in tumor environment is currently being studied by using ultrasounds, in order to further optimize the CEUS acquisition modality.

4.5 Conclusions

In this work, it was shown that liposome-based 3D CEUS images can be considered suitable to accurately reconstruct and numerically describe the vascular network of tumor lesions. The integrated technique was based on image processing, skeletonization, and characterization and can describe morphological and geometrical aspects of the vessel network. This study was conducted in a preclinical environment, but the approach could be easily translated to human applications in the near future. This theranostic technique could be useful for the characterization of tumor types, for the differential diagnosis of suspected lesions, and for the assessment of the effect of anti-cancer drugs (i.e. anti-angiogenetic drugs).

References

1. U. Acharya, O. Faust, S. Sree, F. Molinari, R. Garberoglio, J. Suri, Cost-effective and non-invasive automated benign & malignant thyroid lesion classification in 3D contrastenhanced ultrasound using combination of wavelets and textures: A class of thyroscan™ algorithms. Technol. Cancer Res. Treat. **10**(4), 371–380 (2011)
2. U. Acharya, O. Faust, S. Sree, F. Molinari, J. Suri, ThyroScreen system: High resolution ultrasound thyroid image characterization into benign and malignant classes using novel combination of texture and discrete wavelet transform. Comput. Methods Programs Biomed. **107**(2), 233–241 (2012)

3. N. Faccioli, S. Crippa, C. Bassi, M. D'Onofrio, Contrast-enhanced ultrasonography of the pancreas. Pancreatology **9**(5), 560–566 (2009)
4. T. Herbold, R. Wahba, C. Bangard, M. Demir, U. Drebber, D. Stippel, The laparoscopic approach for radiofrequency ablation of hepatocellular carcinoma - Indication, technique and results. Langenbeck's Arch. Surg. **398**(1), 47–53 (2013)
5. J. Wolff, M. Mason, Drivers for change in the management of prostate cancer - Guidelines and new treatment techniques. BJU Int. **109**(SUPPL. 6), 33–41 (2012)
6. U. R. Acharya, S. Vinitha Sree, M. Muthu Rama Krishnan, L. Saba, F. Molinari, S. Guerriero, J. Suri, Ovarian tumor characterization using 3D ultrasound. Technol. Cancer Res. Treat **11**(6), 543–552 (2012)
7. U. Acharya, S. Sree, L. Saba, F. Molinari, S. Guerriero, J. Suri, Ovarian tumor characterization and classification using ultrasound - A new online paradigm. J. Digit. Imaging **26**(3), 544–553 (2013)
8. T. Boehler, F. Zoehrer, M. Harz, H. Hahn, Breast image registration and deformation modeling. Crit. Rev. Biomed. Eng. **40**(3), 235–258 (2012)
9. U. Roelcke, Imaging brain tumors with PET, SPECT, and ultrasonography. Handb. Clin. Neurol. **104**, 135–142 (2012)
10. W. Uller, E. Jung, M. Hornung, C. Ross, W. Jung, H. Schlitt, C. Stroszczynski, A. Agha, Evaluation of the microvascularization of pathologic parathyroid glands in patients with primary hyperparathyroidism using conventional ultrasound and contrast-enhanced ultrasound. Clin. Hemorheol. Microcirc. **48**(1–3), 95–103 (2011)
11. M. Varras, Benefits and limitations of ultrasonographic evaluation of uterine adnexal lesions in early detection of ovarian cancer. Clin. Exp. Obstetri. Gynecol. **31**(2), 85–98 (2004)
12. J. Hoang, K. Wai, M. Lee, D. Johnson, S. Farrell, US features of thyroid malignancy: Pearls and pitfalls. Radiographics **27**(3), 847–860 (2007)
13. J.-M. Gorce, M. Arditi, M. Schneider, Influence of bubble size distribution on the echogenicity of ultrasound contrast agents: A study of sonovue(TM). Investig. Radiol. **35**(11), 661–671 (2000)
14. J. Bzyl, W. Lederle, A. Rix, C. Grouls, I. Tardy, S. Pochon, M. Siepmann, T. Penzkofer, M. Schneider, F. Kiessling, M. Palmowski, Molecular and functional ultrasound imaging in differently aggressive breast cancer xenografts using two novel ultrasound contrast agents (BR55 and BR38). Eur. Radiol. **21**(9), 1988–1995 (2011)
15. S. Carerj, A. Trono, C. Zito, E. Ficarra, F. Luzza, G. Oreto, F. Arrigo, Harmonic tissue imaging: From physical principles to clinical application [La seconda armonica tissutale: Dai principi fisici all'applicazione clinica]. Ital. Heart J. Suppl. **2**(10), 1078–1086 (2001)
16. M. Schneider, Characteristics of SonoVue(TM). Echocardiography **16**(7) II, 743–746 (1999)
17. R. Carraro, F. Molinari, M. Deandrea, R. Garberoglio, J. Suri, Characterization of thyroid nodules by 3-D contrast-enhanced ultrasound imaging, (2008), pp. 2229–2232
18. F. Molinari, A. Mantovani, M. Deandrea, P. Limone, R. Garberoglio, J. Suri, Characterization of Single Thyroid Nodules by Contrast-Enhanced 3-D Ultrasound. Ultrasound Med. Biol. **36**(10), 1616–1625 (2010)
19. S.-F. Huang, R.-F. Chang, W. Moon, Y.-H. Lee, D.-R. Chen, J. Suri, Analysis of tumor vascularity using three-dimensional power Doppler ultrasound images. IEEE Trans. Med. Imaging **27**(3), 320–330 (2008)
20. Y.-H. Huang, J.-H. Chen, Y.-C. Chang, C.-S. Huang, W. Moon, W.-J. Kuo, K.-J. Lai, R.-F. Chang, Diagnosis of solid breast tumors using vessel analysis in three-dimensional power Doppler ultrasound images. J. Digit. Imaging **26**(4), 731–739 (2013)
21. U. Acharya, S. Sree, G. Swapna, S. Gupta, F. Molinari, R. Garberoglio, A. Witkowska, J. Suri, Effect of complex wavelet transform filter on thyroid tumor classification in three dimensional ultrasound. Proc. Inst. Mech. Eng. Part H J. Eng. Med. **227**(3), 284–292 (2013)
22. F. Molinari, K.M. Meiburger, P. Giustetto, S. Rizzitelli, C. Boffa, M. Castano, E. Terreno, Quantitative Assessment of Cancer Vascular Architecture by Skeletonization of Highresolution 3-D Contrast-enhanced Ultrasound Images: Role of Liposomes and Microbubbles. Technol. Cancer Res. Treat. **13**(6), 541–550 (2014)

23. P. Giustetto, D. Castelli, C. Boffa, S. Rizzitelli, D. Durando, J. Cutrin, S. Aime, E. Terreno, Release of a paramagnetic magnetic resonance imaging agent from liposomes triggered by low intensity non-focused ultrasound. J. Med. Imaging Health Inform. **3**(3), 356–366 (2013)
24. J. Wang, M. Sui, W. Fan, Nanoparticles for tumor targeted therapies and their pharmacokinetics. Curr. Drug Metab. **11**(2), 129–141 (2010)
25. N. Ahmed, H. Fessi, A. Elaissari, Theranostic applications of nanoparticles in cancer. Drug Discov. Today **17**(17–18), 928–934 (2012)
26. E. Terreno, F. Uggeri, S. Aime, Image guided therapy: The advent of theranostic agents. J. Control. Release **161**(2), 328–337 (2012)
27. P. Prabhu, V. Patravale, The upcoming field of theranostic nanomedicine: An overview. J. Biomed. Nanotechnol. **8**(6), 859–882 (2012)
28. S. Gargiulo, A. Greco, M. Gramanzini, S. Esposito, A. Affuso, A. Brunetti, G. Vesce, Mice anesthesia, analgesia, and care, Part II: anesthetic considerations in preclinical imaging studies. ILAR journal / National Research Council, Institute of Laboratory Animal Resources **53**(1), E70–81 (2012)
29. N. Otsu. ‘Threshold selection method from gray-level histograms. IEEE Trans. Syst. Man. Cybern. SMC-**9**(1), 62–66 (1979)
30. C. Ma, M. Sonka, A fully parallel 3D thinning algorithm and its applications. Comput. Vis. Image Underst. **64**(3), 420–433 (1996)
31. C. Arcelli, G. Sanniti Di Baja, L. Serino, Distance-driven skeletonization in voxel images. IEEE Trans. Pattern Anal. Mach. Intell. **33**(4), 709–720 (2011)
32. K. Palágyi, A. Kuba, A 3D 6-subiteration thinning algorithm for extracting medial lines. Pattern Recognit. Lett. **19**(7), 613–627 (1998)
33. J. Silvela, J. Portillo, Breadth-first search and its application to image processing problems. IEEE Trans. Image Process. **10**(8), 1194–1199 (2001)
34. J. Kopechek, K. Haworth, J. Raymond, T. Douglas Mast, S. Perrin Jr., M. Klegerman, S. Huang, T. Porter, D. McPherson, and C. Holland. Acoustic characterization of echogenic liposomes: Frequency-dependent attenuation and backscatter. In: J. Acoust. Soc. Am. **130**(5), 3472–3481 (2011)
35. O. Ishida, K. Maruyama, K. Sasaki, M. Iwatsuru, Size-dependent extravasation and interstitial localization of polyethyleneglycol liposomes in solid tumor-bearing mice. Int. J. Pharm. **190**(1), 49–56 (1999)
36. C. Grouls, M. Hatting, A. Rix, S. Pochon, W. Lederle, I. Tardy, C. Kuhl, C. Trautwein, F. Kiessling, M. Palmowski, Liver dysplasia: US molecular imaging with targeted contrast agent enables early assessment. Radiology **267**(2), 487–495 (2013)
37. D. Delli Castelli, W. Dastrù, E. Terreno, E. Cittadino, F. Mainini, E. Torres, M. Spadaro, S. Aime, In vivo MRI multicontrast kinetic analysis of the uptake and intracellular trafficking of paramagnetically labeled liposomes. J. Control. Release **144**(3), 271–279 (2010)

Chapter 5
Skeletonization Based Blood Vessel Quantification Algorithm for In Vivo Photoacoustic 3D Images

Abstract This chapter (the contents of this chapter build upon the paper: K.M. Meiburger, S.Y. Nam, E. Chung, L.J. Suggs, S.Y. Emelianov, and F. Molinari, **"Skeletonization algorithm-based blood vessel quantification using in vivo 3D photoacoustic imaging"**, In: Physics in Medicine and Biology, 61(22), 2016) closes the second section of this work, which is based on emphasizing quantitative imaging techniques for the assessment of architectural parameters of vasculature that can be extracted from 3D volumes. A skeletonization technique for the quantitative assessment of vascular architecture in burn wounds was developed and validated using completely non-invasive photoacoustic imaging, thus not requiring any contrast agent administration. It was shown how this technique can provide quantitative information about the vascular network from photoacoustic 3D images that can distinguish healthy from diseased tissue. Blood vessels are the only system to provide nutrients and oxygen to every part of the body. Many diseases have significant effects on blood vessel formation, so the vascular network can be a cue to assess malicious tumor and ischemic tissues. Various imaging techniques can visualize blood vessel structure, but their applications are often constrained by expensive costs, contrast agents, ionizing radiations, or a combination of the above. Photoacoustic imaging combines the high-contrast and spectroscopic-based specificity of optical imaging with the high spatial resolution of ultrasound imaging, and image contrast depends on optical absorption. This enables the detection of light absorbing chromophores such as hemoglobin with a greater penetration depth compared to purely optical techniques. A skeletonization algorithm for vessel architectural analysis using non-invasive photoacoustic 3D images acquired without the administration of any exogenous contrast agents is presented in this chapter. 3D photoacoustic images were acquired on rats ($n = 4$) in two different time points: before and after a burn surgery. A skeletonization technique based on the application of a vesselness filter and medial axis extraction is proposed to extract the vessel structure from the image data and six vascular parameters (number of vascular trees (NT), vascular density (VD), number of branches (NB), 2D distance metric (DM), inflection count metric (ICM), and sum of angles metric (SOAM)) were calculated from the skeleton. The parameters were compared (1) in locations with and without the burn wound on the same day and (2) in the same anatomic location before (control) and after the burn surgery. Four out of the six descriptors were statistically different (VD, NB, DM, ICM, $p < 0.05$) when

K.M. Meiburger, *Quantitative Ultrasound and Photoacoustic Imaging for the Assessment of Vascular Parameters*, PoliTO Springer Series,
DOI 10.1007/978-3-319-48998-8_5

comparing two anatomic locations on the same day and when considering the same anatomic location at two separate times (i.e., before and after burn surgery). The study demonstrates how it is possible to obtain quantitative characterization of the vascular network from 3D photoacoustic images without any exogenous contrast agent which can assess microenvironmental changes related to disease progression.

5.1 Introduction

Blood vessels reach into every part of the human body for nutrient and oxygen supply as well as molecular cell signaling [1, 2]. Blood vessel branching, maturation, and quiescence are determined by ambient microenvironments and angiogenic signals. Thus, abnormalities present in the blood vessel structure can reveal underlying disease very early on in its progression [3] and it has been shown that vessel abnormalities normalize with the administration of a successful therapy [4]. It is therefore of critical importance to be able to evaluate vessel network morphologies in a non-invasive and quantitative manner.

Various non-invasive imaging modalities, such as computed tomographic angiography, magnetic resonance angiography, Doppler ultrasound imaging, and recently acoustic angiography have been used to visualize blood vessel structure, as also mentioned in Chap. 4. However, computed tomographic angiography has an issue of ionizing radiation despite of its advantages including superb spatial resolution [5]. Also, magnetic resonance angiography has limitation in accuracy mainly due to rapid extravasation of the magnetic contrast agents [6]. Doppler ultrasound imaging is relatively cost-effective, but it suffers from operator-dependent results and the limited types and duration of the contrast agents [5]. Recently, acoustic angiography has shown positive results of non-invasive vascular imaging but this technique requires exogenous contrast agents and custom-made probes [7, 8]. Optical Coherence Tomography Angiography (OCT-A) is another imaging technique which allows high-resolution imaging of microvascular structures [9]. Studies have shown how this imaging technique can be used for vessel quantification [10–13], however this technique has the main drawback of a limited field of view, where an image produced with one acquisition is typically only a few millimeters wide.

Photoacoustic imaging is a technique that has seen rapid growth in the last decade and it has emerged as an alternative imaging technique to noninvasively visualize microvasculature [14]. The photoacoustic wave can be generated by thermoelastic expansion after the absorption of a short laser pulse. Because the contrast mechanism of photoacoustic imaging is based on optical absorption, blood vessels can be imaged using strong photon-absorbing endogenous chromophores, in particular hemoglobin, without any additional support from exogenous contrast agents [15]. Also, physiological parameters such as oxygen saturation and hemoglobin concentration can be quantitatively assessed using photoacoustic imaging [16, 17]. Photoacoustic imaging has been extensively used to monitor various tissues, such as breast [18], skin

[19], brain [20], and eyes [21, 22], in which microvascular changes are critical and needed to be quantitatively and longitudinally assessed.

However, even though enormous amounts of data from blood vessel structures have been collected using photoacoustic imaging, an extremely limited number of studies are devoted to vessel architectural analysis. Yang et. al presented a multiparametric quantitative microvasculare imaging technique, but their method was relative to Optical Resolution PhotoAcoustic Microscopy (OR-PAM) images, which produce very high resolution images but are limited to 1.2 mm depth in biological tissues [23, 24]. Among various methods to assess complex vasculature, skeletonization algorithms, used with 3D contrast enhanced ultrasound images, have shown to be able to characterize and quantify thyroid nodular vascularization in clinical patients [25] and tumor vascularization in in vivo preclinical studies [26]. A skeletonization algorithm for vessel architectural analysis of 3D photoacoustic data without the administration of any contrast agent is presented here, which is based on [27] and it is demonstrated how it obtains quantitative information about the vascular network in tissue mimicking phantoms and in vivo subcutaneous tissue.

5.2 Materials and Methods

5.2.1 Tissue Mimicking Vessel Phantom for Combined Ultrasound and Photoacoustic Imaging

A tissue mimicking vessel phantom was prepared to evaluate the skeletonization algorithm for photoacoustic imaging compared to that for ultrasound imaging used in previous studies [25, 26]. Specifically, 8 % polyvinyl alcohol (PVA) solution was mixed with silica particles (1 wt% and 15 µm diameter) and fine graphite particles (1 wt% and 30 µm diameter) to mimic acoustic and optical properties. Then, the mixed solution was poured into plastic tubes with an inner diameter of 1 mm and molded by three cycles of freezing and thawing. The crosslinked PVA phantom was cut and dried for a day to form a vessel-like structure. The PVA phantom was placed on the bottom layer of the background phantom (8 % porcine skin gel) and the same gelatin solution was used to fill the top layer of the phantom. Figure 5.1 displays the top view of the ultrasound (a) and photoacoustic (b) 3D images that were acquired with the tissue mimicking vessel phantom.

5.2.2 Burn Injury Model

The burn injury model was used to validate the developed skeletonization algorithm for quantification of blood vessel changes. The dorsal surface of Lewis rats (male, 8–15 weeks) were burned using a temperature controlled brass plate with a diameter of

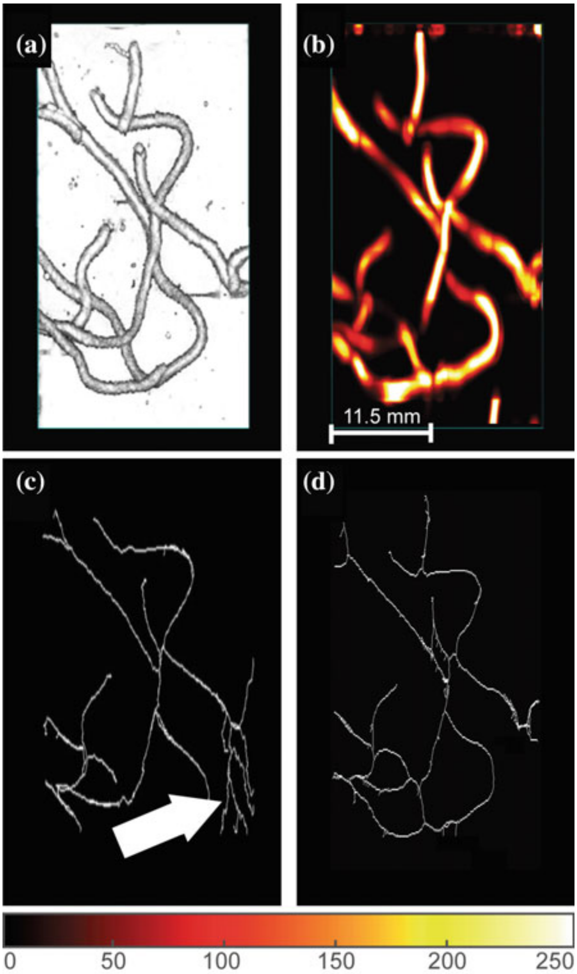

Fig. 5.1 Phantom data. **a** Top view of the ultrasound volume of the phantom; **b** Top view of the photoacoustic volume of the phantom; **c** Top view of the ultrasound skeleton; **d** Top view of the photoacoustic skeleton. Image taken with permission from [27]

1.8 cm after anesthesia of the rats with inhalation of 2 % isoflurane. ECG, respiration, and body temperature of the rat were monitored using the animal monitoring board during anesthesia. The heating temperature was $87\infty C$ and the heating duration was 10 s. For 2 days after burn injury, analgesic drug (Buprenorphine, 0.05 g/kg) was injected to the rats every 12 h. Also, weight and behavior of the rats with burn injury were monitored until the end of the experiment. The rats were housed and cared according to the regulation and guidance of the Animal Resource Center in The University of Texas at Austin and the Institutional Animal Care and Use Committee (IACUC) protocol $(AUP-2010-00111)$.

5.2.3 Ultrasound and Photoacoustic Imaging

An ultrasound imaging system (Vevo 2100, VisualSonics, Inc.) and a tunable laser system (Vevo LAZR, VisualSonics, Inc.) was used to acquire ultrasound and photoacoustic signals. The pulsed laser with a pulse duration of 7 ns and a wavelength of 880 nm was delivered through an optical fiber bundle integrated with an ultrasound linear 128 element array transducer (MS-550S, VisualSonics, Inc.) operating at a center frequency of 40 MHz. Both ultrasound and photoacoustic signals from a two-dimensional imaging plane were captured using the combined imaging probe and three-dimensional data with a size of 13.88 mm $\diamond$ 29.5 mm $\diamond$ 7.8 mm were acquired by incremental mechanical movement of the probe in the elevational direction (i.e., orthogonal to the imaging plane). In the case of in vivo imaging, motion artifacts were compensated by acquiring the signals while respiratory motion was minimized. The dorsal area containing both healthy and injured tissue was imaged at different time points before and after the burn surgery. A total of 4 animals were used for the burn surgery and the imaging experiment. The burn surgery was done on day 0, whereas the animals were imaged on day -2 (i.e., two days before the burn surgery, reported as Day-2) and then again on day 14 (i.e., fourteen days after the burn surgery, reported as Day14). Furthermore, the imaging was done so that the burn wound area was contained in half of the acquired volume, providing a burn area and a control area for each volume. So the in-vivo dataset contained 8 total volumes, consisting of 16 areas to be analyzed: 8 control area volumes and 8 burn area volumes (4 before the surgery and 4 after).

5.2.4 Image Processing

The developed image processing algorithm is divided into 3 main steps before the skeletonization procedure is applied: (1) image preprocessing, (2) morphological dilation, (3) and thresholding and segmentation. Figure 5.2 shows the steps of the algorithm before skeletonization, which will be explained in more detail below. The center slices of the analyzed volumes are reported by columns. The first column portrays the maximum intensity projection top view of the photoacoustic image.

Preprocessing

First of all, a 3D median filter was applied to the volume, because this filter produces a good noise reduction in photoacoustic images. Moreover, since the data of interest in the image volumes are blood vessels, a Frangi-vesselness filter was then applied to further remove noise and photoacoustic signal that was not deriving from blood vessels [28]. The Frangi filter is characterized by its scale (or sigma) which determines the dimensions of the vessels that are recognized in the 3D image. By combining multiscale measurements, both large and small vessels can be displayed. To consider both microvasculature and larger vessels, a sigma size ranging from 2 to 10 with a

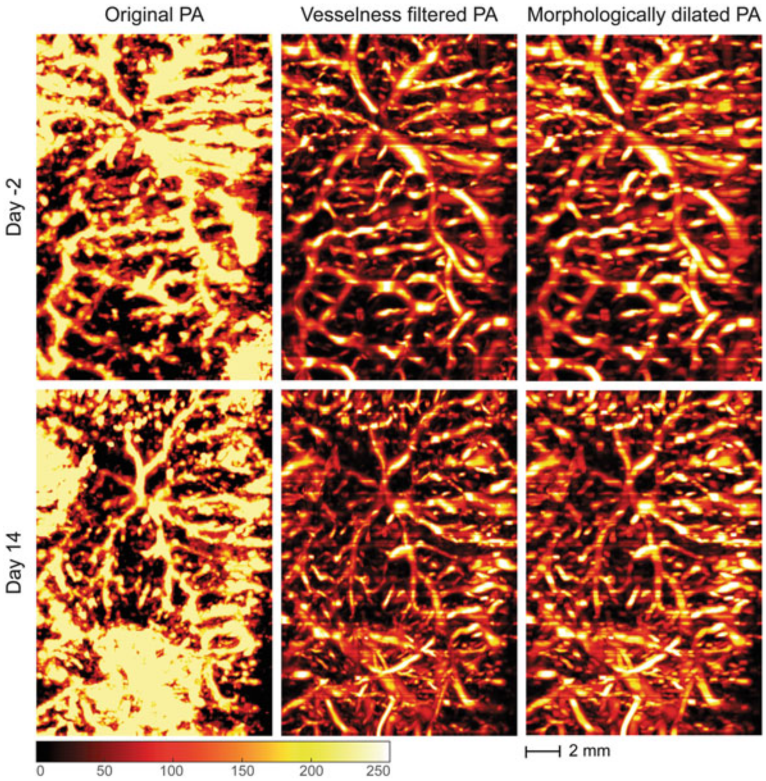

Fig. 5.2 Preprocessing steps. Each row represents one of the two dataset areas considered: The *first row* (Panels **a**, **b**, **c**) shows the entire imaged area on Day-2, whereas the *second row* shows the entire imaged area on Day14 (Panels **d**, **e**, **f**). The *top half* of the imaged area represents the "control" area, whereas the *bottom half* of the imaged area is the "burn" area. The *first column* (Panels **a**, **d**) shows the original PA image; the *second column* (Panels **b**, **e**) display the PA image filtered with the vesselness filter; the *last column* (Panels **c**, **f**) shows the morphologically dilated image volume. PA = Photoacoustic. Image taken with permission from [27]

step size of 2 was adopted. A step size of 2 was chosen to reduce computational time since using a step size of 1 did not show noticeable difference in pilot studies (not presented here).

The filtered image can be seen in the second column of Fig. 5.2.

Morphological Dilation

After the initial preprocessing stage, the slices of the volume were morphologically dilated using a disk-shaped structural element with radius 3. This particular morphological operation was added in the image processing pipeline to further emphasize the intensity of the photoacoustic signal given by blood and to smoothen out the data. The morphologically dilated slice can be seen in the third column of Fig. 5.2.

Thresholding and Segmentation

In order to obtain a final binary volume to be skeletonized, the preprocessed and morphologically dilated slices of the volume were segmented. Since each slice clearly represents either the lack of a photoacoustic signal (structures not containing haemoglobin, i.e., non-vessel structures) or the presence of a photoacoustic signal (structure containing a high amount of haemoglobin, i.e., blood vessels), a percentage (40 %) of Otsu's threshold was used to separate the statistical distribution of the two classes [29]. A percentage of Otsu's threshold was used instead of the nominal value because the actual threshold minimizes the intraclass variance of the black and white pixels, which systematically overestimates an accurate threshold when considering photoacoustic images in which the lack of signal is equal to zero.

The final segmented top view can be seen in the first column of Fig. 5.3.

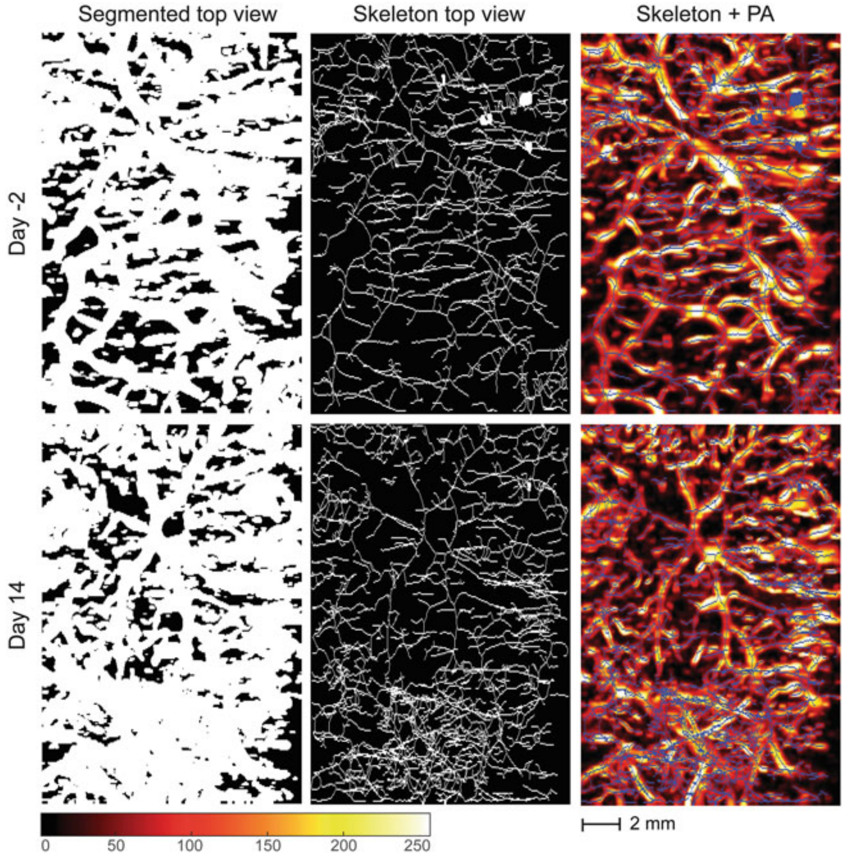

Fig. 5.3 Skeletonization Process. The *first column* (Panels **a**, **d**) shows the top view of the segmented volume; the *second column* (Panels **b**, **e**) shows the skeleton obtained by extracting the medial axis, and the *third column* (Panels **c**, **f**) shows the final skeleton overlaid in *blue* on the photoacoustic top view image. PA = Photoacoustic. Image taken with permission from [27]

5.2.5 Skeletonization

After all the slices were segmented, a skeletonization process was applied to reduce the representation of the vascular network. This procedure is specifically designed to reduce the segmented binary volume into a minimal representation of the network while still preserving morphology. Since the morphology of interest in this case are blood vessels, a medial axis extraction skeletonization algorithm was employed [30, 31].

The final skeleton obtained after the application of the topological skeleton can be seen in the second column of Fig. 5.3. The final skeleton overlaid in blue on the photoacoustic maximum intensity projection top view is displayed in the third column of Fig. 5.3.

5.2.6 Vascular Pattern Characterization

Once the 3D skeletons, which are basically volumetric binary images containing a network of vessels, were obtained, we then analyzed the characteristics of the network in order to provide a quantitative measure of the subcutaneous vascularization. Each 3D skeleton was therefore analyzed with the Breadth First Search (BFS) algorithm [32]. To standardize the quantification of the vascular pattern, we chose a fixed size of a Region Of Interest (ROI) equal to 7.5 mm × 3.75 mm × 10 mm. This size was used because it was compatible with the dimensions of the burn area size used in our dataset. The ROI positioning was done manually. The BFS technique was implemented in MATLAB as a customized software and automatically searches all the skeleton nodes inside the selected ROI starting from a given node. The procedure iterates on all the nodes and then stops when all the nodes have been visited, mapping the skeleton as a series of vascular trees. Once the entire ROI skeleton is mapped, quantitative parameters are automatically found in order to numerically describe the vascular pattern.

The six vascular patterns considered are as follows, and are the same that were assessed in Chap. 4:

1. Number of vascular Trees (NT): defined as the number of trees in which the BFS algorithm decomposes the skeleton volume.
2. Vascular Density (VD): defined as the number of skeleton voxels compared to the volume of the selected ROI.
3. Number of Branching nodes (NB): defined as the number of branches of the structure.
4. 2D Distance Metric (DM): Defined as the ratio between the actual path length of the curve and the linear distance between the first and last point of the curve, where each curve represents a vessel. This is a measure of the bidimensional tortuosity of the vessel, since the DM value of a straight line would be equal to 1, whereas it would present higher values as the curvature increases.

5. Inflection Count Metric (ICM): Defined as the number of flexes of a curve multiplied by the 2D distance metric. This is another measurement of vessel tortuosity, which takes into consideration the difference between a gentle curve and a much more tortuous vessel that makes abrupt changes in direction.
6. 3D Sum Of Angles Metric (SOAM): Defined as the sum of all the angles that a curve has in space. This tortuosity measurement is necessary since neither the DM or ICM parameter are able to handle tight coils well.

The mathematical description of the tortuosity parameters can be found in previously published studies [33, 34] and in Sect. 1.4.2. Summarizing, the vascular complexity was characterized by three morphological parameters (NT, VD, NB) and by three curvature/tortuosity parameters (DM, ICM, SOAM).

5.3 Results

5.3.1 Phantom

Figure 5.1c–d shows the obtained skeletons for the phantom. The left column shows the skeleton obtained with the same contrast-enhanced ultrasound imaging skeletonization technique that has been used in previous studies [25, 26] and was presented in Chap. 4, whereas the right column is relative to the skeleton obtained using the photoacoustic skeletonization technique that is presented here. The top row shows the top view of the ultrasound (a) and Photoacoustic (b) phantoms and the bottom row displays the corresponding skeletonized top images.

Table 5.1 reports the values of the vascular descriptors for the phantom. The values were measured on the 3D ultrasound and photoacoustic volumes after skeletonization.

As can be seen by Fig. 5.1, the results obtained with the phantom show how the photoacoustic skeletonization technique (Fig. 5.1d) presents a similar skeletonized structure compared with a similar technique used in ultrasound imaging in previous studies (Fig. 5.1c) [25, 26].

Further considerations on the numerical results portrayed in Table 5.1 are made in the Discussion section.

Table 5.1 Values of the six descriptors of the vascular patterns as measured from the 3D ultrasound and photoacoustic skeletons

	NT	VD	NB	DM	ICM	SOAM
US Phantom	1	0.0033	13	2.111	108.740	1.095
PA Phantom	1	0.0043	17	1.656	99.219	1.248

NT Number of vascular trees; *VD* Vascular density; *NB* Number of branching nodes; *DM* 2D distance metric; *ICM* Inflection count metric; *SOAM* 3D sum of angles metric

5.3.2 *In Vivo Study*

Figure 5.4 reports the obtained skeletons from the four sets of photoacoustic images for one animal of the dataset. The first and second column of Fig. 5.4 are relative to the control and burn area before the surgery (Day-2), respectively, whereas the third and fourth column are relative to the control and burn area after the surgery (Day 14). The first row of Fig. 5.4 portrays the central slice of the combined ultrasound and photoacoustic images; the yellow rectangle shows the specific region of interest that was analyzed for vascular parameter calculation. The second row reports the top view of the photoacoustic images within the considered ROI; the third row depicts the corresponding skeletonized top view images; the bottom row instead shows the top view photoacoustic images with the skeleton overlaid in blue. It is possible to observe that the skeleton of the burn area after the surgery is very rich and represents

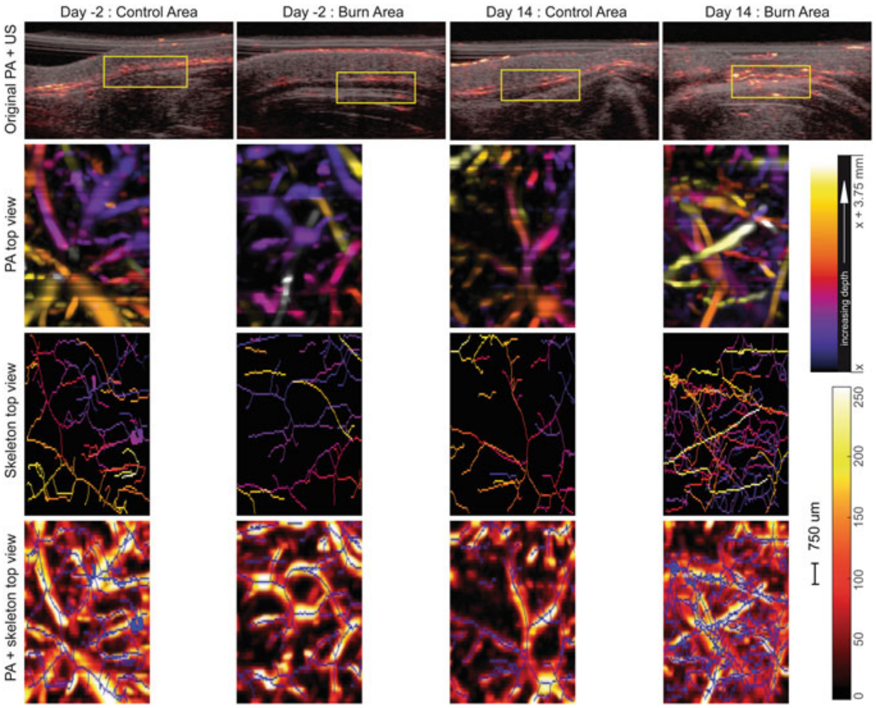

Fig. 5.4 Representation of the final 3D skeletons. The *first column* is relative to the control area on *Day*-2, the second to the burn area on *Day*-2, the third to the control area on *Day* 14, and the fourth to the burn area on *Day* 14. The *first row* represents the original US and PA images (central slice of considered area); the *second row* shows the top view of the PA volume in the considered Region Of Interest; the *third row* depicts the corresponding skeletonized top view image; the *bottom row* shows the skeleton overlaid in the photoacoustic top-view image. US = Ultrasound, PA = Photoacoustic. Image taken with permission from [27]

a dense intra-lesion vasculature. Conversely, the skeletons obtained from the control areas and the burn area before the surgery are limited and show a noticeably less visual representation of skeletonized blood vessels.

Table 5.2 reports the average values ± the standard deviation of the vascular descriptors. The values were measured on the 3D photoacoustic volumes after skeletonization. The box plots of the six parameters are also portrayed in Fig. 5.5, which clearly emphasizes the vascular parameter changes on the burn area before and after the injury.

The first comparison is between the vascular descriptors obtained when comparing the burn area and control area on the same day after the burn surgery, $Day14$ (first and second rows of Table 5.2). The asterisks in Table 5.2 show the descriptors that were statistically different between the two photoacoustic skeletons (paired Student's t-test; $p < 0.05$). Four out of the six descriptors were statistically different (VD, NB, DM, ICM).

Secondly, the comparison between the vascular descriptors obtained on the burn area on $Day14$ and the burn area on Day-2 (first and third rows) also show statistically significant differences. The crosses in Table 5.2 show the descriptors that were statistically different between the two photoacoustic skeletons (paired Student's t-test; $p < 0.05$). In this case, again four out of the seven descriptors were statistically different (VD, NB, DM, ICM).

As can be seen, the values reported by the first row when compared to the second and third rows are quite different, thus demonstrating the effectiveness of the skeletonization algorithm to obtain quantitative information about the vascular network that can distinguish healthy from diseased tissue. The quantitative results can be also be visually appreciated by the box plots in Fig. 5.5, which clearly portray the difference of the vascular parameters, when comparing both the burn area before and after the injury and the burn area compared to the control area at the same time point.

Table 5.2 Average values of the descriptors of the vascular patterns as measured from the 3D photoacoustic skeletons

Study	NT	VD^{a,b}	NB^{a,b}	DM^{a,b}	ICM^{b}	SOAM
$Day14$ **Burn area**	8 ± 3	0.002 ± 0.0004	55 ± 14	2.187 ± 0.239	65.437 ± 10.403	1.048 ± 0.062
$Day14$ **Control area**	4 ± 2	0.001 ± 0.0004	22 ± 6	1.494 ± 0.159	35.099 ± 3.399	1.072 ± 0.057
Day-2 **Burn area**	5 ± 2	0.001 ± 0.0004	25 ± 4	1.665 ± 0.099	46.481 ± 11.707	1.000 ± 0.059
Day-2 **Control area**	5 ± 2	0.001 ± 0.0004	28 ± 11	1.656 ± 0.093	38.845 ± 4.840	1.019 ± 0.062

[a] The descriptors that were statistically different between $Day14$ burn area and $Day14$ control area (paired Student's t-test; $p < 0.05$)

[b] The descriptors that were statistically different between $Day14$ burn area and Day-2 burn area (paired Student's t-test; $p < 0.05$)

NT Number of vascular trees; *VD* Vascular density; *NB* Number of branching nodes; *DM* 2D distance metric; *ICM* Inflection count metric; *SOAM* 3D sum of angles metric

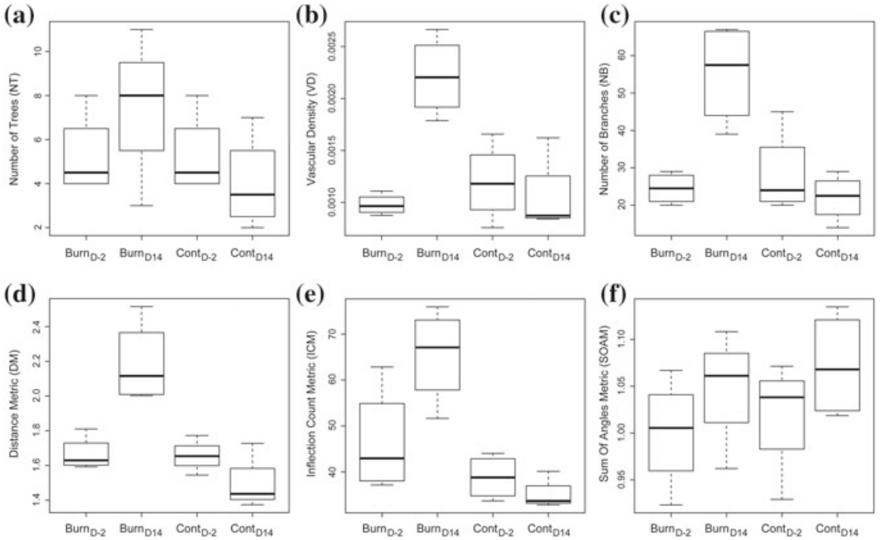

Fig. 5.5 Box plots of the six vascular parameters in the burn area on Day-2 (Burn_{D-2}), burn area on Day14 (Burn_{D14}), control area on Day-2 (Cont_{D-2}) and control area on Day14 (Cont_{D14}). **a** Number of vascular trees; **b** Vascular density; **c** Number of branches; **d** Distance metric; **e** Inflection count metric; **f** Sum of angles metric. Image taken with permission from [27]

On the other hand, when comparing the control areas on $Day14$ and on Day-2, none of the six descriptors showed a significant difference ($p \geq 0.05$). Similarly, the burn area on Day-2 and the control area on Day-2 did not show a statistically significant difference for any of the vascular descriptors ($p \geq 0.05$).

5.4 Discussion

The ability to evaluate vessel network morphologies in a non-invasive and quantitative manner can provide crucial information that can reveal disease early in its progression, among other things [27].

A skeletonization process using a completely non-invasive photoacoustic (PA) imaging technique is presented here to obtain a quantitative analysis of vessel structure extracted from three-dimensional PA images. Phantoms were specifically made to mimic basic vessel complexity, and the results obtained with the proposed method and with a method used in previous studies were also compared.

The phantom vascular parameter results are similar between the two techniques and visually present a similar skeletonized structure, showing how the proposed technique can correctly identify a vascular structure from 3D photoacoustic images. As can be seen in Fig. 5.1, the interface between the top and bottom layer of the phantom produced some artifacts in the ultrasound image, and therefore in the resulting ultrasound skeleton (see white arrow). These artifacts are most likely what produced the discrepancies between the ultrasound and photoacoustic skeletons in the calculation of the quantitative vascular parameters.

Considering the burn injury in-vivo model, again no contrast agents were necessary to obtain the vascular parameters, and it was found that the vascular parameters calculated after a burn surgery showed a significant increase compared to the same area analyzed before the burn surgery (VD, NB, DM, ICM parameters). It was moreover shown that the parameters obtained analyzing the burn area were significantly different from those analyzed in a control area on the same animal (i.e., not where the burn surgery was done) and on the same day (VD, NB, DM, ICM parameters). The results from this study indicated that the skeletonization technique can be successfully used to provide a quantitative basis for distinguishing healthy from diseased tissue volumes, without the use of any contrast agent.

The number of vascular trees (NT) and the sum of angles metric (SOAM) were not significantly different when comparing both the burn area on different days and the burn area with the control area. In both cases, the burn area dataset on $Day14$ showed higher average results, but not a statistically significant difference. It is clear, even visually (see Fig. 5.4), that the vascular density is much higher in the burn area on $Day14$, however this does not necessarily imply that the number of vascular trees must increase, but that at least the tortuosity complexity of the vessels should increase, with the creation of new vessels. In fact, the 2D distance metric and the inflection count metric are always statistically higher when comparing the burn area on two separate days (before and after surgery) and when comparing the burn area and control area on Day14. The sum of angles metric is specifically useful when the vasculature involves many tight coils [33], and can therefore provide important information especially when considering tumor lesion vasculature which has shown to often present vessels that form high frequency coils of low amplitude [8, 33]. It can therefore be assumed that the angiogenesis process in the animal study did not contain as many tight coiled vessels, but rather broader and more meandering neo-vessels.

Photoacoustic imaging has grown exponentially in the last decades and enormous amounts of data from blood vessel structures have been collected using this imaging method. However, as far as what was found in literature, the study reported in [27] and again described in this chapter, is the first time a skeletonization technique for quantitative vascular network analysis has been proposed for 3D volumetric photoacoustic imaging. In this study, photoacoustic data acquired with the VisualSonics Vevo LAZR system was used, which utilizes a linear probe for ultrasound detection; however the skeletonization technique in itself does not depend on the detection system and could easily be adapted to other photoacoustic volumetric data, including photoacoustic tomography with spherical and/or cylindrical detection systems [35, 36], photoacoustic microscopy [37–40], and systems which use other types of signal detection, such as Fabry–Perot scanners [41].

5.5 Conclusions

It can be concluded that the comparison of vascular network quantification without the use of any contrast agent is feasible with photoacoustic volumetric datasets, and future studies using this quantitative architectural analysis of vessel structure on data obtained from tumor lesions will be done to further test and validate this technique.

References

1. P. Carmeliet, Angiogenesis in life, disease and medicine. Nature **438**(7070), 932–936 (2005)
2. P. Carmeliet, R.K. Jain, Molecular mechanisms and clinical applications of angiogenesis. Nature **473**(7347), 298–307 (2011)
3. E. Bullitt, N.U. Lin, M.G. Ewend, D. Zeng, E. P. Winer, L.A. Carey, J.K. Smith, Tumor therapeutic response and vessel tortuosity: preliminary report in metastatic breast cancer, in *Medical Image Computing and Computer-Assisted Intervention-MICCAI 2006* (Springer, New York, 2006), pp. 561–568
4. C.Y. Li, S. Shan, Q. Huang, R.D. Braun, J. Lanzen, K. Hu, P. Lin, M.W. Dewhirst, Initial stages of tumor cell-induced angiogenesis: evaluation via skin window chambers in rodent models. J. Natl Cancer Inst. **92**(2), 143–147 (2000)
5. J.T. Perry, J.D. Statler, Advances in vascular imaging. Surg. Clin. North Am. **87**(5), 975–993 (2007)
6. D.M. McDonald, P.L. Choyke, Imaging of angiogenesis: from microscope to clinic. Nat. Med. **9**(6), 713–725 (2003)
7. R.C. Gessner, C.B. Frederick, F.S. Foster, P.A. Dayton, Acoustic angiography: a new imaging modality for assessing microvasculature architecture. J. Biomed. Imaging **2013**, 14 (2013)
8. R.C. Gessner, S.R. Aylward, P.A. Dayton, Mapping microvasculature with acoustic angiography yields quantifiable differences between healthy and tumor-bearing tissue volumes in a rodent model. Radiology **264**(3), 733–740 (2012)
9. T.E. de Carlo et al., A review of optical coherence tomography angiography (OCTA). Int. J. Retina Vitreous **1**(1), 5 (2015)
10. Y.M. Liew, R.A. McLaughlin, P. Gong, F.M. Wood, D.D. Sampson, In vivo assessment of human burn scars through automated quantification of vascularity using optical coherence tomography. J. Biomed. Opt. **18**(6), 061213 (2012)
11. L. Kuehlewein, S.R. Sadda, D. Sarraf, OCT angiography and sequential quantitative analysis of type 2 neovascularization after ranibizumab therapy. Eye **29**(7), 932–935 (2015)
12. J. Lee, H. Radhakrishnan, W. Wu, A. Daneshmand, M. Climov, C. Ayata, D.A. Boas, Quantitative imaging of cerebral blood flow velocity and intracellular motility using dynamic light scattering-optical coherence tomography. J. Cereb. Blood Flow Metab. **33**(6), 819–25 (2013)
13. R. Reif, J. Qin, L. An, Z. Zhi, S. Dziennis, R. Wang, Quantifying optical microangiography images obtained from a spectral domain optical coherence tomography system. Int. J. Biomed. Imaging **2012**, Article ID 509783, p. 11 (2012)
14. S.Y. Emelianov, P.-C. Li, M. O'Donnell, Photoacoustics for molecular imaging and therapy. Phys. Today **62**(8), 34 (2009)
15. J. Wang, M. Sui, W. Fan, Nanoparticles for tumor targeted therapies and their pharmacokinetics. Curr. Drug Metab. **11**(2), 129–141 (2010)
16. S.Y. Nam, L.M. Ricles, L.J. Suggs, S.Y. Emelianov, In vivo ultrasound and photoacoustic monitoring of mesenchymal stem cells labeled with gold nanotracers. PLoS One **7**(5), e37267 (2012)
17. S. Hu, K. Maslov, L.V. Wang, In vivo functional chronic imaging of a small animal model using optical-resolution photoacoustic microscopy. Med. Phys. **36**(6), 2320–2323 (2009)

18. R.A. Kruger, R.B. Lam, D.R. Reinecke, S.P. Del Rio, R.P. Doyle, Photoacoustic angiography of the breast. Med. Phys. **37**(11), 6096–6100 (2010)
19. H.F. Zhang, K. Maslov, G. Stoica, L.V. Wang, Functional photoacoustic microscopy for high-resolution and noninvasive in vivo imaging. Nat. Biotechnol. **24**(7), 848–851 (2006)
20. G. Ku, X. Wang, X. Xie, G. Stoica, L.V. Wang, Imaging of tumor angiogenesis in rat brains in vivo by photoacoustic tomography. Appl. Opt. **44**(5), 770–775 (2005)
21. S. Jiao, M. Jiang, J. Hu, A. Fawzi, Q. Zhou, K.K. Shung, C.A. Puliafito, H.F. Zhang, Photoacoustic ophthalmoscopy for in vivo retinal imaging. Opt. Express **18**(4), 3967–3972 (2010)
22. W. Song, Q. Wei, T. Liu, D. Kuai, J.M. Burke, S. Jiao, H.F. Zhang, Integrating photoacoustic ophthalmoscopy with scanning laser ophthalmoscopy, optical coherence tomography, and fluorescein angiography for a multimodal retinal imaging platform. J. Biomed. Opt. **17**(6), 0612061–0612067 (2012)
23. Z. Yang, J. Chen, J. Yao, R. Lin, J. Meng, C. Liu, J. Yang, X. Li, L. Wang, L. Song, Multi-parametric quantitative microvascular imaging with optical-resolution photoacoustic microscopy in vivo. Opt. Express **22**(2), 1500–1511 (2014)
24. Y.S. Zhang, J. Yao, C. Zhang, L. Li, L.V. Wang, Y. Xia, Optical-resolution photoacoustic microscopy for volumetric and spectral analysis of histological and immunochemical samples. Angew. Chem. Int. Ed. **53**(31), 8099–8103 (2014)
25. F. Molinari, A. Mantovani, M. Deandrea, P. Limone, R. Garberoglio, J. Suri, Characterization of single thyroid nodules by contrast-enhanced 3-d ultrasound. Ultrasound Med. Biol. **36**(10), 1616–1625 (2010)
26. F. Molinari, K.M. Meiburger, P. Giustetto, S. Rizzitelli, C. Boffa, M. Castano, E. Terreno, Quantitative assessment of cancer vascular architecture by skeletonization of highresolution 3-d contrast-enhanced ultrasound images: role of liposomes and microbubbles. Technol. Cancer Res. Treat. **13**(6), 541–550 (2014)
27. K.M. Meiburger, S.Y. Nam, E. Chung, L.J. Suggs, S.Y. Emelianov, F. Molinari, Skeletonization algorithm-based blood vessel quantification using in vivo 3D photoacoustic imaging. Phys. Med. Biol. **61**(22) (2016)
28. A.F. Frangi, W.J. Niessen, K.L. Vincken, M.A. Viergever, Multiscale vessel enhancement filtering, in *Medical Image Computing and Computer-Assisted Interventation "MICCAI" '98* (Springer, New York, 1998), pp. 130–137
29. N. Otsu, Threshold selection method from gray-level histograms. IEEE Trans. Syst. Man Cybern. SMC **9**(1), 62–66 (1979)
30. M. Kerschnitzki, P. Kollmannsberger, M. Burghammer, G.N. Duda, R. Weinkamer, W. Wagermaier, P. Fratzl, Architecture of the osteocyte network correlates with bone material quality. J. Bone Min. Res. **28**(8), 1837–1845 (2013)
31. T.-C. Lee, R.L. Kashyap, C.-N. Chu, Building skeleton models via 3-D medial surface axis thinning algorithms. CVGIP: Graph. Models Image Process. **56**(6), 462–478 (1994)
32. J. Silvela, J. Portillo, Breadth-first search and its application to image processing problems. IEEE Trans. Image Process. **10**(8), 1194–1199 (2001)
33. E. Bullitt, G. Gerig, S.M. Pizer, W. Lin, S.R. Aylward, Measuring tortuosity of the intracerebral vasculature from MRA images. IEEE Trans. Med. Imaging **22**(9), 1163–1171 (2003)
34. E. Bullitt, K.E. Muller, I. Jung, W. Lin, S. Aylward, Analyzing attributes of vessel populations. Med. Image Anal. **9**(1), 39–49 (2005)
35. F. Kiessling, D. Razansky, F. Alves, Anatomical and microstructural imaging of angiogenesis. Eur. J. Nucl. Med. Mol. Imaging **37**(1), 4–19 (2010)
36. A. Taruttis, E. Herzog, D. Razansky, V. Ntziachristos, Real-time imaging of cardiovascular dynamics and circulating gold nanorods with multispectral optoacoustic tomography. Opt. Express **18**(19), 19592–19602 (2010)
37. H. Zhang, K. Maslov, G. Stoica, L. Wang, Functional photoacoustic microscopy for highresolution and noninvasive in vivo imaging. Nat. Biotechnol. **24**(7), 848–851 (2006)
38. J. Staley, P. Grogan, A. Samadi, H. Cui, M. Cohen, X. Yanga, Growth of melanoma brain tumors monitored by photoacoustic microscopy. J. Biomed. Opt. **15**(4) (2010)

39. J.-T. Oh, M.-L. Li, H. Zhang, K. Maslov, G. Stoica, L. Wang, Three-dimensional imaging of skin melanoma in vivo by dual-wavelength photoacoustic microscopy. J. Biomed. Opt. **11**(3) (2006)
40. M.-L. Li, J. Wang, J. Schwartz, K. Gill-Sharp, G. Stoica, L. Wang, In-vivo photoacoustic microscopy of nanoshell extravasation from solid tumor vasculature. J. Biomed. Opt. **14**(1) (2009)
41. E.Z. Zhang, P.C. Beard, A miniature all-optical photoacoustic imaging probe. SPIE BiOS. International Society for Optics and Photonics (2011), pp. 78991F-78991F

Conclusions and Final Remarks

As stated in the Introduction, healthcare is continuously seeking improved quantitative medical imaging techniques with which to better diagnose, treat, and monitor the health of patients. The work presented in this final work aims at the development of quantitative imaging techniques for the improvement of the diagnosis, treatment, and monitoring of two of the main causes of death in the world: cardiovascular diseases and cancer.

Firstly, automated segmentation techniques for the intima-media complex were presented in general. It was then demonstrated how the correct carotid localization in the B-mode longitudinal ultrasound images is of fundamental importance and how this task can be accomplished with a fully automated algorithm.

A new completely automated algorithm for the segmentation of the common carotid artery far wall was developed and validated, and it was shown that the technique is able to correctly segment atherosclerotic plaques in B-mode longitudinal ultrasound images. The performances of the algorithm were validated against expert human tracings and benchmarked with a semi-automated technique, and the results were very promising. Since it is a completely automated method, it does not require any human interaction and could therefore be used to process large databases, removing subjectivity from the process and providing a clinical tool that could be easily used in daily practice. This technique could also provide the first steps to an automatic plaque classification and characterization system.

The automated IMT measurement was validated in numerous situations and was found to be a useful parameter for the prediction and association of clinical parameters of patients with coronary artery disease.

Secondly, a vascular parameter regarding the morphology and variation of the common carotid artery wall thickness, the intima-media thickness variability (IMTV), was studied in depth. Since recent studies have shown that the IMT variation along the carotid artery wall has a stronger correlation with atherosclerosis than the nominal intima-media thickness value itself, a good understanding of this vascular parameter, its dependencies, and how it should be calculated, is of fundamental importance. The results from this validation study demonstrated that the

K.M. Meiburger, *Quantitative Ultrasound and Photoacoustic Imaging for the Assessment of Vascular Parameters*, PoliTO Springer Series,
DOI 10.1007/978-3-319-48998-8

IMTV measurement is most reliably calculated with the Hausdorff distance metric, and underlined the importance of automatic algorithms since it was found that manual segmentations of the far wall should not be considered as being reliable for the IMTV measurement.

Thirdly, a quantitative imaging technique for the assessment of architectural parameters of the vascular network that can be extracted from 3D volumes obtained with contrast-enhanced ultrasound imaging was used to demonstrate how the characterization and description of the vascular network of a cancer lesion in mouse models can be effectively determined using both traditional microbubbles and liposomes. Eight mice were administered both microbubbles and liposomes and 3D CEUS volumes were acquired. Vascular architectural descriptors were calculated after a skeletonization technique was applied, and it was found that liposome-based 3D CEUS images are suitable to accurately reconstruct and numerically describe the vascular network of tumor lesions. The study was conducted in a preclinical environment, but the approach could be easily translated to human applications in the near future. This theranostic technique could be useful for the characterization of tumor types, for the differential diagnosis of suspected lesions, and for the assessment of the effect of anti-cancer drugs (i.e. anti-angiogenetic drugs).

Finally, the development and validation of a skeletonization technique for the quantitative assessment of vascular architecture in burn wounds using completely non-invasive photoacoustic imaging was presented. 3D photoacoustic images were acquired in 2 different time frames on rats ($n = 4$): before and after a burn surgery. The skeletonization technique extracted the vessel structure from the image data and six vascular parameters were calculated from the skeleton. This study demonstrated that the comparison of vascular network quantification without the use of any contrast agent is feasible with photoacoustic volumetric datasets, and that it can distinguish healthy from diseased tissue. Future studies using this quantitative architectural analysis of vessel structure on data obtained from tumor lesions will be done to further test and validate this technique.

In conclusion, it can be affirmed that the aim of this work, the development and presentation of quantitative techniques for ultrasound and photoacoustic imaging for the assessment of architectural and vascular parameters, was achieved.